Schwarz Domain Decomposition Algorithms for the Closest Point Method on Closed Manifolds

by

Alireza Yazdani

B.Sc., Sharif University of Technology, 2018

Thesis Submitted in Partial Fulfillment of the
Requirements for the Degree of
Master of Science

in the
Department of Mathematics
Faculty of Science

SIMON FRASER UNIVERSITY
Fall 2021

Declaration of Committee

Name:	**Alireza Yazdani**
Degree:	**Master of Science**
Thesis title:	**Schwarz Domain Decomposition Algorithms for the Closest Point Method on Closed Manifolds**
Committee:	**Chair:** Ralf Wittenberg Associate Professor, Mathematics **Steven Ruuth** Supervisor Professor, Mathematics **Ronald Haynes** Committee Member Professor, Mathematics Memorial University of Newfoundland **JF Williams** Examiner Associate Professor, Mathematics

Abstract

The discretization of surface intrinsic PDEs has challenges that one might not face in flat spaces. The closest point method (CPM) is an embedding method that represents surfaces using a function that maps points in the flat space to their closest points on the surface. This mapping brings intrinsic data onto the embedding space, allowing us to numerically approximate PDEs by standard methods in a tubular neighbourhood of the surface. Here, we solve the surface intrinsic positive Helmholtz equation by the CPM paired with finite differences which usually yields a large, sparse, and non-symmetric linear system. Domain decomposition methods, especially Schwarz methods, are robust algorithms to solve these linear systems. In this work, we investigate the convergence of four Schwarz-CPM methods for 1-manifolds in $\mathbb{R}^d$. The analysis is followed by numerical experiments for verification.

Keywords: Surface intrinsic partial differential equations; closest point method; domain decomposition methods; parallel and alternating Schwarz; classical and optimized Schwarz methods.

Dedication

This thesis work is dedicated to my wife, Fatemeh, who has been a constant source of support and encouragement during the challenges of graduate school and life. I am truly thankful for having you in my life.

Acknowledgements

I am extremely thankful to Professor Steven Ruuth and Professor Ronald Haynes, Department of Mathematics at Memorial University, for their noble guidance, valuable suggestions, support with full encouragement, and enthusiasm. This thesis would not have been possible without their help.

I am grateful for my family whose constant love and support keep me motivated and confident. I hope the sacrifices you have endured for me to pursue this dream will be repaid to you with many opportunities for joy and success in your future.

Table of Contents

List of Figures

Chapter 1

Introduction

Surface differential equations arise in a wide variety of natural phenomenon such as biological systems, fluid dynamics, and image processing. For instance, the development of a human brain is investigated by solving a Gray-Scott reaction-diffusion equation on a sphere with a finite element approach in [36]. Coat markings of animals and pigmentation patterns on butterfly wings are modelled using differential equations (mostly reaction-diffusion equations) posed on surfaces. In an interesting work, the evolution of the stripes in the fish Pomacanthus is analyzed in [34]. In fluid dynamics, thin films can be modelled on surfaces. For example, in [30], a theoretical model is developed for surfactant and liquid delivery to lungs. Also, solidification on surfaces is another important field of study where surface differential equations arise. For example, ice accumulation on the surface of aircrafts has been a bottleneck in the design process [46].

Herein, we consider the surface intrinsic positive Helmholtz equation

$$(c - \Delta_{\mathcal{S}})u = f, \tag{1.1}$$

where $\Delta_{\mathcal{S}}$ denotes the Laplace–Beltrami operator associated with the surface $\mathcal{S} \subset \mathbb{R}^d$, and $c > 0$ is a constant. We provide various fields of study that the surface intrinsic positive Helmholtz equation becomes of interest. The Laplace–Beltrami operator appears in the flattening of human brain surface [3]. A flattened representation of the brain is important for visualizing magnetic imaging data that translates neural activity within the brain folds. In order to diagnose neurodegenerative diseases – particularly Alzheimer's disease – in early stages using MRI images, cortical thickness of the human brain is estimated using the Laplace–Beltrami operator applied on the brain [56]. In another application, Equation (1.1) with $f = 0$ is solved on graphs to perform dimensionality reduction [5]. Dimensionality reduction plays an important role in data representation and can be exploited for clustering a dataset. Suppose that for an $n \times n$ gray scale image of an object under a fixed lighting that each pixel represents the brightness with a value from zero to one. Such images belong to the space of $[0, 1]^{n^2}$, however, all images of a specific object form a manifold in the embedding space of $[0,1]^{n2}$. Learning the manifold of interest, the dataset can be represented in the lower dimensional space of the manifold. Further, the learned manifold can be used later to categorize data. Hence, the process is also called manifold learning. Having a set of data, a graph is constructed in the embedding space. The eigenmaps of the Laplace–Beltrami operator are evaluated on the graph to represent the data in a lower dimensional space. In [13], the authors introduce a novel method to classify a given data point by perturbing the manifold where a specific category of the data live. Another interesting application of the surface intrinsic positive Helmholtz equation is in shape analysis. The eigenfunctions of the Laplace–Beltrami operator on 3D surfaces are visionary as they provide insights into the morphology and structure of the surface [49]. Note that the eigenproblem of the Laplace–Beltrami operator is equivalent to Equation (1.1) with $f = 0$. In [49], the eigenfunctions of the Laplace–Beltrami operator are utilized for shape segmentation. Moreover, the eigenfunctions of the operator have been used for shape comparison [51]. In another work, corresponding points in an object with several poses are found by the eigenfunctions [17]. The same approach is used for determining the corresponding points in a symmetric 3D triangulated object [17]. As the gradient and divergence operators are defined over the Riemannian structure of the manifold, the spectrum of the Laplace–Beltrami operator − which depends on the gradient and divergence operators − is isometry invariant. In addition, scaling an object by a factor of a can be compensated by normalizing the eigenvalues by $1/a^2$. These properties of the Laplace–Beltrami operator along with some other properties stated in [50] make the Laplace–Beltrami operator a valuable asset in statistical shape analysis. See [10] for an application of the Laplace–Beltrami operator for reconstructing colored surfaces obtained from 3D scans. There are also some other possible applications of the eigenfunctions of the Laplace–Beltrami listed in [37]: signal processing on surfaces, registration and pose transfer, and parameterization. The Laplace–Beltrami operator also appears in the modelling of thermal behaviour of thin membranes coated on nanoparticles [2]. Lastly, discretization of this equation arises from the time-stepping of reaction-diffusion equations on surfaces [42]. As a consequence, considerable recent work has taken place to develop efficient, high-speed solvers for this and other related PDEs on surfaces.

There are several methods to solve surface intrinsic differential equations. If a surface parameterization (a mapping from the surface to a parameter space) is known, then the equation can be solved in the parameter domain [14]. For a one-dimensional manifolds embedded in a higher dimensional space, obtaining the parameterization is a fairly easy task. The given curve can be parameterized along the arc length. The parameterization method follows by discretizing the differential equations along the curve length. The parameterization of higher dimensional manifolds is more difficult and cannot be performed analytically for general manifolds. Expensive computational and numerical approaches are required for the parameterization of general manifolds. An ideal parameterization preserves the metric structure of the manifold, such as area and angles of shapes for a two-dimensional manifold.

However, such a parameterization does not exist in general, and a single metric structure is traded off against the others. In [54], an angle preserving model for the parameterization of a 2D manifold is proposed that minimizes the angular distortion without any constraints on the area distortion. For preserving both area and angles of the manifold of interest, a functional energy is defined in [14] whose minimizer is a parameterization of the surface. Here, there is a parameter involved that can be tuned to switch between angle preserving and area preserving parameterizations. Another angle preserving approach is introduced in [38] that results in conformal parameterization of the manifold. There have also been some works on optimizing the parameterization that maintain the overall structure of parameterizations while reducing memory requirements [53]. An excellent discussion on the parameterization of surfaces can be found in [21]. After finding an appropriate parameterization of the manifold, we discretize the surface intrinsic differential operators in the parameter space. Note that the discretization needs special treatment if the parameterization is not conformal. This is the drawback of the parameterization approach for solving surface intrinsic differential equations, as a conformal parameterization of manifolds cannot be easily obtained. Indeed, the process of finding a conformal parameterization is computationally expensive and is closely related to finding the eigenfunctions of the Laplace–Beltrami operator [38]. It has to be pointed out that the error analysis of such approaches strongly depends on the parameterization, and switching between different parameterizations leads to a completely different accuracy. Further, the new coordinates achieved by a parameterization may end up in establishing artificial singularities such as the poles of spherical coordinates

Another approach that has been widely used in the literature for solving the surface intrinsic differential equations is the finite element method. For a one-dimensional curve, the finite element method is equivalent to the parameterization approach described above. Hence, we restrict the discussion to higher dimensional manifolds. In order to utilize the finite element method for solving a surface differential equation, one first needs a triangulation of the surface. If a triangulation of the manifold is not available, one must be created. There are many techniques for constructing a triangulation of a manifold such as [31], but this is beyond the scope of this thesis. Supposing a triangulated surface is in hand, a finite element discretization of the surface intrinsic differential operator can be created. It is shown in [18] that there exists a unique discrete solution in the space of piecewise linear functions to an elliptic surface intrinsic differential equation such as Equation (1.1) on a compact surface. The finite element approach has been used in various fields of study for solving surface differential equations; e.g., pattern formation on evolving biological surfaces [4], the Cahn–Hilliard equation on surfaces [20], and diffusion smoothing on brain surface [11]. Some finite element discretizations of the Laplace–Beltrami operator can be found in [15, 47]. Although the approach has been widely used, the accuracy of the method strongly depends on the quality of the triangulation and intrinsic properties of the geometry, and it is not well understood for general surfaces [18].

Alternatively, we can solve the differential equation in a neighbourhood of the surface using standard PDE methods in the underlying embedding space. The advantage of discretizing the equivalent partial differential equation in the embedding space over the other approaches is its accurate error, stability, and robustness measures – which are unknown for the finite element and parameterization methods described above. Note that the implementation is also quite simple. We, herein, list some methods of this kind. In [8], the level set of the embedded manifold of co-dimension one is used to transform the surface differential equation into an equivalent PDE in the embedding space. If an implicit representation of the manifold is in hand, the level set representation of the manifold is obtained by solving the classical Hamilton–Jacobi equation $||\nabla\psi|| = 1$ where $\psi : \mathbb{R}^d \to \mathbb{R}$ denotes the level set of the manifold. The surface is the zero level set, i.e., $\mathcal{S} = \{x \in \mathbb{R}^d | \psi(x) = 0\}$. Otherwise, if a triangulated surface is given, one can employ a variety of approaches [58, 35] to find the implicit representation of the surface. Surface properties can be simply computed using the level set representation ψ, if needed. PDE approximations are also simplified, since we are now able to use standard finite difference schemes in the embedding space. Further, the method is capable of solving a PDE on a surface that simultaneously evolves [1]. The method introduced in [8] has a number of drawbacks, especially in the case of diffusion equations on surfaces. Since we solve a PDE (consistent with the surface differential equation) in one higher dimension, it is usually solved in a small band around the manifold to reduce the cost of solving in a higher dimension. Subsequently, suitable boundary conditions are required for the PDE in the underlying embedding space. However, the analytic solution does not depend on the boundary conditions. Dirichlet and Neumann boundary conditions lead to a jump in the solution and the gradient of solution, respectively, and this results in large errors [29]. Hence, how to choose appropriate boundary conditions is unclear. Another limitation involved in the method is that there is no capability of the method for open manifolds or manifolds of co-dimension higher than one.

The *closest point method* (CPM) is an embedding method suitable for the discretization of PDEs on surfaces that addresses the drawbacks of the other approaches discussed above [52]. The CPM can be simply implemented as the discretization is done using finite differences on a fixed point Cartesian grid. The method is discussed in detail in Chapter 2. The closest method typically leads to non-symmetric linear systems to solve [43]. On complex geometries or when varying scales arise, iterative solvers can be slow despite the sparsity of the underlying systems [44]. In order to develop an efficient iterative solver which is also capable of parallelism, parallel Schwarz and optimized parallel Schwarz algorithms have been applied to the CPM for (1.1) in [44]. The Schwarz methods have also been used as a preconditioner for Krylov space iterative methods [44] to boost the convergence. In [44], the CPM coupled with the Schwarz methods shows promising results and decent convergence, however, a robust convergence analysis is missing. The ultimate goal of this thesis is to provide a convergence analysis of such methods. Before proceeding, we give a brief litera-

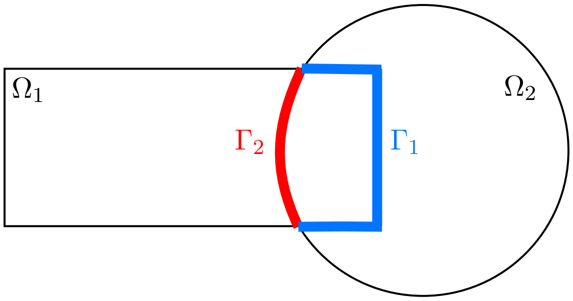

Figure 1.1: A complex domain decomposed into two simple subdomains, namely a rectangle and a circle.

ture review of domain decomposition methods, particularly Schwarz methods, on surface intrinsic differential equations.

Domain decomposition methods solve a boundary value problem by splitting the original problem into smaller boundary value problems called subproblems. The classical alternating Schwarz method is the first introduced domain decomposition method (Hermann Schwarz, 1860). At first, the main goal of the algorithm was to prove the Dirichlet principle over complex geometries, at a time when the principle had been introduced and proved by Riemann over simple geometries where Fourier analysis is applicable. Suppose the domain of interest Ω is decomposed into two overlapping subdomains, Ω_1 and Ω_2. In addition, the interfaces are defined as $\Gamma_1 = \partial\Omega_1 \cap \Omega_2$ and $\Gamma_2 = \partial\Omega_2 \cap \Omega_1$. These are illustrated in Figure 1.1. Schwarz introduced the first domain decomposition algorithm (which we call the classical alternating Schwarz method) for the Dirichlet problem $\Delta u = 0$ in Ω and $u = g$ on $\partial\Omega$ as:

$$\begin{aligned} \Delta u_1^{n+1} &= 0 && \text{in } \Omega_1, & \Delta u_2^{n+1} &= 0 && \text{in } \Omega_2, \\ u_1^{n+1} &= u_2^n && \text{on } \Gamma_1, & u_2^{n+1} &= u_1^{n+1} && \text{on } \Gamma_2. \end{aligned}$$

Note that u_1^{n+1} and u_2^{n+1} both must satisfy the boundary condition on $\partial\Omega$, but we have ignored them for simplicity. Since each subproblem uses the very last information from the other subdomain, the method is called alternating. Indeed, the subproblems communicate through the artificially imposed boundary conditions. The iteration continues until u_1^{n+1} and u_2^{n+1} match on the overlapping region. Schwarz also proved the convergence of the method at the continuous level. The convergence factor of the method for a one-dimensional positive Helmholtz equation at the continuous and discrete levels is obtained by explicitly solving the subproblems and can be found in [16]. Moreover, the convergence factor of the method on the whole $\mathbb{R}^2$ plane is found by Fourier analysis [16]. Later, in 1988 when parallel computers were becoming important, Pierre-Louis Lions proposed the parallel variant of the Schwarz method described above:

$$\begin{aligned} \Delta u_1^{n+1} &= 0 \quad \text{in } \Omega_1, & \Delta u_2^{n+1} &= 0 \quad \text{in } \Omega_2, \\ u_1^{n+1} &= u_2^n \quad \text{on } \Gamma_1, & u_2^{n+1} &= u_1^n \quad \text{on } \Gamma_2. \end{aligned}$$

We call this method the classical parallel Schwarz method and its only difference with the classical alternating Schwarz method is the indexing of the boundary condition of the second subproblem. The optimized Schwarz methods were proposed with the additional idea of a better communication between the subdomains by using linear operators across the interfaces. Imposing a Robin boundary condition, $\mathcal{B} = \partial/\partial\hat{n} + \alpha$ where $\hat{n}$ denotes the outward normal to the interface and α is called the Robin parameter, gives the optimized alternating Schwarz method:

$$\begin{aligned} \Delta u_1^{n+1} &= 0 \quad \text{in } \Omega_1, & \Delta u_2^{n+1} &= 0 \quad \text{in } \Omega_2, \\ \mathcal{B}u_1^{n+1} &= \mathcal{B}u_2^n \quad \text{on } \Gamma_1, & \mathcal{B}u_2^{n+1} &= \mathcal{B}u_1^{n+1} \quad \text{on } \Gamma_2, \end{aligned}$$

and the optimized parallel Schwarz method:

$$\begin{aligned} \Delta u_1^{n+1} &= 0 \quad \text{in } \Omega_1, & \Delta u_2^{n+1} &= 0 \quad \text{in } \Omega_2, \\ \mathcal{B}u_1^{n+1} &= \mathcal{B}u_2^n \quad \text{on } \Gamma_1, & \mathcal{B}u_2^{n+1} &= \mathcal{B}u_1^n \quad \text{on } \Gamma_2. \end{aligned}$$

The optimized methods benefit from better information exchange through subdomains and consequently converge faster compared to the classical methods [25]. However, the general convergence of the optimized Schwarz methods has been elusive [40]. See [23] for the convergence analysis of the optimized Schwarz methods for the Helmholtz equation defined over the free space $\mathbb{R}^d$. The convergence is shown for a special partitioning of the space and only for the case with two subdomains. For an extensive discussion on generalizing the methods for more subdomains, please refer to [16]. One can also see [16, 25] for the discretized versions of the methods. Although the Schwarz methods were introduced for elliptic PDEs, they have shown potential for solving other type of PDEs. For instance, the Schwarz methods have been applied to the advection diffusion equations [22] and parabolic equations [24].

While there has been substantial work carried out on Schwarz methods, they have not been widely applied to surface intrinsic differential operators. The Schwarz iterations have been applied to the shallow-water equation defined over a rotating sphere that typically arises in atmospheric and oceanic modelling [33, 57]. The domain used in [33, 57] is a cubed-sphere which is naturally decomposed to 6 subdomains, and the differential equations are discretized using a finite volume scheme. The classical parallel Schwarz [12] and optimized parallel Schwarz [39] iterations for the surface intrinsic Laplace equation have also been investigated on the unit sphere. In these works, the analysis is based on latitudinal subdomains that are periodic in longitude. The Schwarz methods have been proved to converge for the spherical Laplacian when the sphere is partitioned to two and three subdomains in a latitudinal fashion. Hence, the Fourier transform is a natural choice to solve the subproblems analytically and obtain the contraction factor. An optimal transmission condition is also proposed in [39] that improves the convergence. The classical and optimized parallel Schwarz methods are also analyzed with an overset grid for the shallow-water equation in [48]. In that work, the discretization in 1D is reduced to the positive definite Helmholtz problem on the unit circle. The unit circle case is investigated with two equal-sized subdomains, and a convergence factor is derived for the configuration in terms of the overlap parameter. Moreover, the optimization problem associated with the optimal Robin parameter is given, but no solution is provided. The 2D positive definite Helmholtz problem on the sphere is also analyzed where the subdomains are derived from a Yin-Yang grid system.

In this thesis, we study the convergence of the Schwarz iterations for the CPM at the continuous level for smooth, simple closed 1-manifolds where periodicity is inherent in the geometry. After a review of the CPM and Schwarz-CPM in Chapter 2, we will show in Chapter 3 that this problem, posed in $\mathbb{R}^d$, is equivalent to a one-dimensional periodic problem. This leads us to study the convergence of Schwarz methods for the 1-dimensional periodic problem in detail, an analysis that is missing in the literature. However, the convergence of the Schwarz iterations for general manifolds of co-dimension two remains unknown. It is worth noting a key difference between this thesis and [48]. In our problem, domain subdivision is carried out in the underlying embedding space. As a consequence, the unequal-sized subdomain case is essential to our understanding of the problem. In addition, we prove the convergence and derive the convergence factor for more than two subdomains, while the analysis in [48] is restricted to only two equal-sized subdomains. We also prove the convergence of the optimized Schwarz iterations for the one-dimensinonal periodic positive Helmholtz equation and derive the convergence factor. Although (1.1) on 1-manifolds can be simply solved through parameterization, we investigate the convergence of the Schwarz-CPM for 1-manifolds in this paper with the hope of extending our work to higher dimensional manifolds in the future. The optimal Robin parameter is also found for this problem.

The rest of the thesis is organized as follows: Chapter 2 reviews the CPM and the Schwarz iterations for the CPM. Chapter 3 studies the Schwarz-CPM combinations for the surface intrinsic positive Helmholtz equation (1.1) by analyzing an equivalent one-dimensional periodic problem. This section proves convergence and derives convergence factors. Chapter 4 provides a numerical experiment in which the Schwarz-CPM contraction factor converges to its Schwarz iteration counterpart by increasing the grid resolution. Finally, Chapter 5 gives conclusions.

Chapter 2

The Closest Point Method

In this chapter, we will introduce the Closest Point Method (CPM) for solving surface intrinsic partial and ordinary differential equations. We start with the CPM and extend our discussion to domain decomposition for the CPM (DDCPM).

2.1 The Closest Point Method

The Closest Point Method (CPM) is an embedding method that discretizes surface intrinsic PDEs in the embedding space. It was first introduced in [52] with the aim of solving evolutionary PDEs on surfaces. At the heart of the CPM, there is a closest point mapping $\text{cp}_{\mathcal{S}}$ which maps any point in the computational domain (each of which belongs to the embedding space) onto a point lying on the manifold:

$$\text{cp}_{\mathcal{S}}(x) = \underset{s \in \mathcal{S}}{\arg\min} ||x - s||. \tag{2.1}$$

This mapping gives the closest point in Euclidean distance to the surface $\mathcal{S}$ for any point x in the embedding space. It is well-defined for any point in the embedding space within a distance R_0 of a smooth surface, where R_0 is a lower bound for the surface radii of curvature [9]. We need the closest point mapping to extend functions and surface values defined on the surface to the embedding space. Hence, efficient and accurate methods are required to construct the closest point function. The closest point mapping can be computed analytically for simple manifolds with analytic representation such as circles, spheres, tori, while we need computational tools when it comes to complex manifolds. Standard numerical optimization techniques can be utilized to compute the closest point function for parameterized surfaces [45]. For triangulated surfaces, more complex methods such as the tree-based algorithms of Strain [55] might be used to determine the closest point function at grid nodes. However, a simple search algorithm over the computational nodes of the CPM for finding the closest nodes from the manifold is often effective. Further, restricting the radius of the search significantly improves the efficiency. This simple approach has a work estimate that scales linearly with the number of triangles for a triangulated surface [52]. Thus, this approach is often sufficient for problems of practical interest.

Although a rigorous convergence study of the method has not been provided in the literature, one can state results for the consistency of the CPM with the original surface intrinsic PDE. Two principles are fundamental to the CPM: *equivalence of gradients* and *equivalence of divergence* [52]. We state the principles and show that the CPM for the surface intrinsic positive Helmholtz equation is equivalent to the original PDE. Though, one may make use of the principles to show the consistency of the CPM for general PDEs. The principles are as follows:

1. **Equivalence of Gradients.** For any function v defined on $\mathbb{R}^d$ which is constant along the directions normal to a manifold $\mathcal{S}$ with a well-defined closest point function, the equivalence of gradients principle indicates the following on the manifold:

$$\nabla v = \nabla_{\mathcal{S}} v.$$

2. **Equivalence of Divergence.** Suppose $v \in \mathbb{R}^d$ is a vector field that is tangent to all level-sets of the distance function to $\mathcal{S}$ with a well-defined closest point representation. The equivalence of divergence principle states that on the manifold:

$$\nabla \cdot v = \nabla_{\mathcal{S}} \cdot v.$$

The first principle indicates that v only varies along the surface, while equivalence of divergence states that there is no flux going through the manifold when v is a vector field directed along the manifold.
Suppose the closest point mapping of the manifold $\mathcal{S}$ is well-defined over $\Omega \in \mathbb{R}^d$. We introduce $\tilde{u} : \Omega \to \mathbb{R}$ as the solution to the embedding CPM problem for the surface intrinsic positive Helmholtz equation (1.1). Since $\tilde{u}(\mathrm{cp}_{\mathcal{S}})$ is constant in the normal direction to the manifold, the equivalence of gradients principle gives us

$$\nabla \tilde{u}(\mathrm{cp}_{\mathcal{S}}) = \nabla_{\mathcal{S}} u,$$

on the surface, where u is the solution to the original surface PDE. Further, $\nabla \tilde{u}(\mathrm{cp}_{\mathcal{S}})$ is directed along the manifold. By applying the equivalence of divergence principle,

$$\nabla \cdot (\nabla \tilde{u}(\mathrm{cp}_{\mathcal{S}})) = \nabla_{\mathcal{S}} \cdot (\nabla \tilde{u}(\mathrm{cp}_{\mathcal{S}})),$$

is obtained on the surface. Therefore, on the manifold, we recover the surface differential operator by combining the two principles:

$$\Delta \tilde{u}(\mathrm{cp}_{\mathcal{S}}) = \nabla \cdot (\nabla \tilde{u}(\mathrm{cp}_{\mathcal{S}})) = \nabla_{\mathcal{S}} \cdot (\nabla \tilde{u}(\mathrm{cp}_{\mathcal{S}})) = \nabla_{\mathcal{S}} \cdot (\nabla_{\mathcal{S}} u) = \Delta_{\mathcal{S}} u. \tag{2.2}$$

It follows that the embedding PDE is consistent with the original surface PDE.

While the CPM was introduced for solving evolutionary surface differential equations, it is also capable of solving time-independent surface PDEs [43]. In the evolutionary case, given an initial condition, we extend values off the surface to the computational domain of the embedding space. Then, the embedding PDE is computed using regular discretization methods for one time step. In the last step, the surface values are interpolated using the embedding solution for the future extension to the embedding space. The procedure iterates with an explicit time-stepping to reach the ultimate time. It is shown that the implicit time-stepping lacks stability at the discrete level. A modified version of (2.2) offers improved stability at the discrete level and is normally used in elliptic problems [43, 41, 27]. The regularized Laplace operator is

$$\Delta_h^{\#}\tilde{u} = \Delta\tilde{u}(\mathrm{cp}_{\mathcal{S}}) - \frac{2d}{h^2}\left[\tilde{u} - \tilde{u}(\mathrm{cp}_{\mathcal{S}})\right], \tag{2.3}$$

where $0 < h \ll 1$. As in [43, 41], we take the parameter h to be equal to the mesh spacing in the fully discrete setting. In fact, $\Delta_h^{\#}\tilde{u}$ can be seen as $\Delta\tilde{u}(\mathrm{cp}_{\mathcal{S}})$ penalized for large change in the normal direction. Note that $\tilde{u} - \tilde{u}(\mathrm{cp}_{\mathcal{S}}) = 0$ on the manifold.

Equation (2.3) gives our replacement for the Laplace-Beltrami operator. Applying it, and extending the function f off the manifold using the closest point mapping gives our embedding equation for (1.1):

$$(c - \Delta_h^{\#})\tilde{u} = f(\mathrm{cp}_{\mathcal{S}}). \tag{2.4}$$

Standard numerical methods in the embedding space may be applied to (2.4) to complete the discretization. Herein, we apply standard second order finite differences on regular grids to approximate the derivative operators. Because discrete points do not necessarily lie on $\mathcal{S}$, an interpolation scheme is needed to recover surface values. Utilizing tensor product barycentric Lagrangian interpolation [7] in a dimension-by-dimension fashion, an extension matrix $\mathbf{E}$ is defined to extend values off the manifold. Note that the extension matrix may be viewed as a discretization of the closest point mapping.

In practice, one computes on a narrow tubular region around the manifold rather than the entire embedding space. As mentioned earlier, the manifold values are interpolated. In order to perform the interpolation to a desired accuracy, it is required to have sufficient nodes clustered around the interpolated node. We call the points associated with the interpolation *active nodes*. The active nodes appear in the interpolation stencil for at least one point on the manifold. The ultimate aim is to discretize the differential operator over the active nodes with the second order centred finite difference approximation of the Laplacian. Thus, we complete the computational domain by introducing another list of nodes called *ghost nodes*. The ghost nodes are located at the boundaries of the computational domain. Figure 2.1 illustrates the active and ghost nodes for an arbitrary 1-manifold in $\mathbb{R}^2$. Using a mesh spacing h and degree-p interpolation polynomials, it is sufficient to numerically approximate

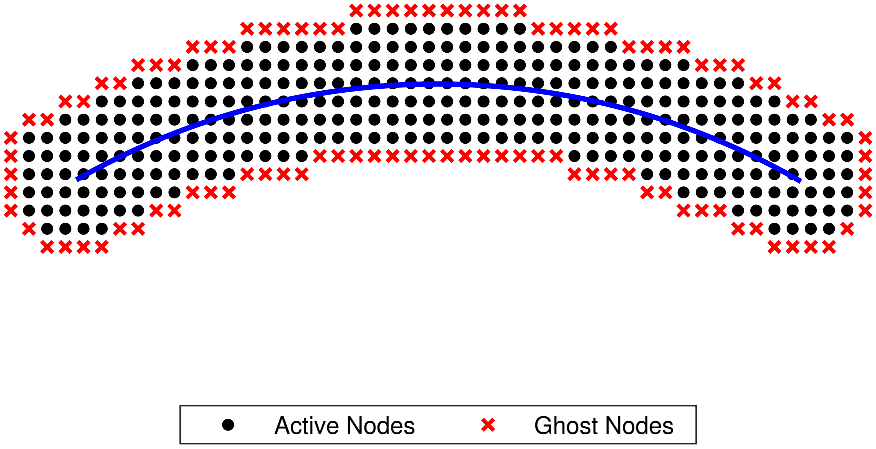

Figure 2.1: Active and ghost nodes for a curve with degree-four polynomial interpolation.

equation (2.4) in a narrow tube around $\mathcal{S}$ of radius [52]

$$\lambda = \sqrt{(d-1)(p+1)^2 + (p+3)^2} h/2. \tag{2.5}$$

Suppose n_a and n_g represent the number of the active and ghost nodes in a problem, respectively. Further, we have $n = n_a + n_g$ nodes lying on the manifold – each corresponds to a node in the computational domain. The extension matrix $\mathbf{E}$ is an $n \times n_a$ matrix that performs n linear interpolations over the active nodes for all points in the computational domain. The differential operator matrix $\mathbf{\Delta_h} \in \mathbb{R}^{n_a \times n}$ approximates the Laplacian on the active nodes with the aid of the ghost nodes. By defining $\widetilde{\mathbf{M}} = \mathbf{\Delta_h E}$, the embedding PDE at the discrete level for $\mathbf{u} \in \mathbb{R}^{n_a \times 1}$ is

$$(c\mathbf{I_{n_a}} - \widetilde{\mathbf{M}})\mathbf{u} = \mathbf{f}, \tag{2.6}$$

where $\mathbf{I_{n_a}} \in \mathbb{R}^{n_a \times n_a}$ denotes the identity matrix, and $\mathbf{f} \in \mathbb{R}^{n_a \times 1}$ is a vector corresponding to f in (1.1) and extends f to the active nodes in the embedding space. As mentioned before, Equation (2.6) is numerically unstable. The modified version with the regularized differential equation described in Equation (2.4) is given by:

$$\mathbf{M} = \text{diag } \mathbf{\Delta_h} + (\mathbf{\Delta_h} - \text{diag } \mathbf{\Delta_h})\mathbf{E}, \tag{2.7}$$

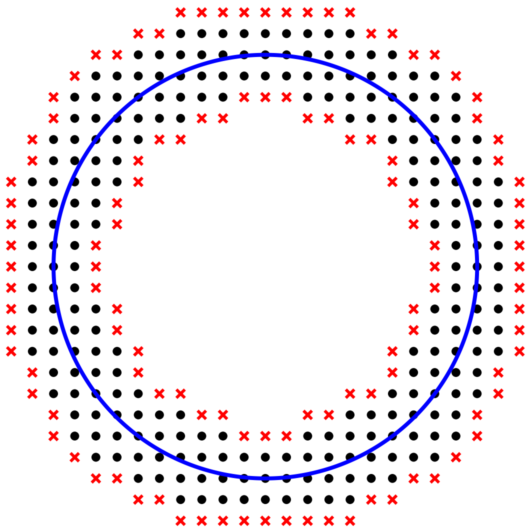

Figure 2.2: Active nodes (black circles) and ghost nodes (red cross marks) for the unit circle in $\mathbb{R}^2$ with $h = 0.1$ and $p = 2$.

or diagrammatically,

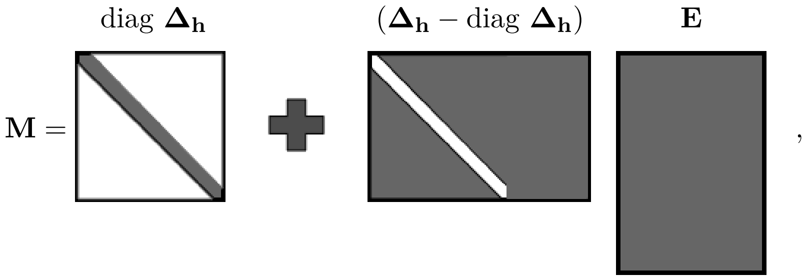

where the diag operator extracts the diagonal elements of the matrix and forms a square matrix with the extracted diagonal elements.

Assuming $\mathcal{S}$ is the unit circle in $\mathbb{R}^2$, the computational nodes in the embedding space for a degree-two interpolation with mesh spacing of $h = 0.1$ is shown in Figure 2.2. There are 240 active and 116 ghost points for this problem. Further, the structure of the associated extension and operator matrices along with the stabilized matrix $\mathbf{M}$ are shown in Figure 2.3. The number of nonzero elements in the matrix $\mathbf{M}$ is 3744, resulting in $\sim 93.3\%$ sparsity. Refining the mesh increases the sparsity of the matrix $\mathbf{M}$ [43]. This motivates the development of efficient algorithms for solving the linear system in Equation (2.6).

2.2 Domain Decomposition for The Closest Point Method

Following the discussion in Chapter 1, efficient solvers and preconditioners are required for the CPM. The linear system that arises from the discretization is usually large which makes a direct solve inefficient. On the other hand, iterative solvers can be slow for complex

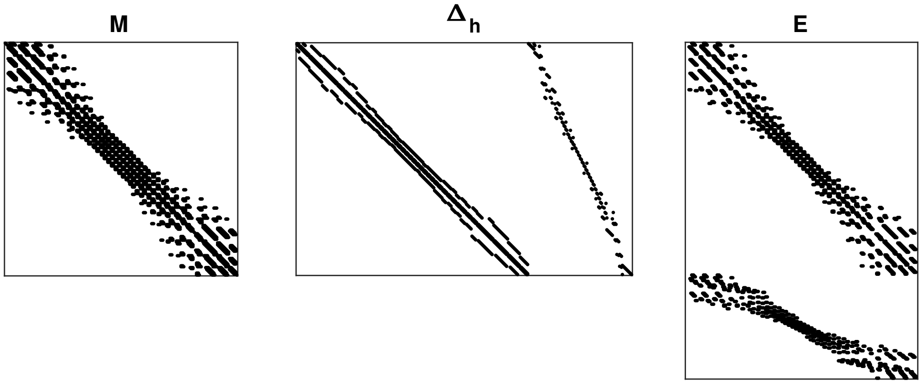

Figure 2.3: Sparsity structure of the CPM matrices for the unit circle shown in Figure 2.2.

geometries or when varying scales arise. Domain decomposition methods serve well when they are employed as solvers or preconditioners for the CPM [44]. The parallel classical and optimized Schwarz methods are coupled with the CPM for solving the surface intrinsic positive Helmholtz equation (1.1) on some manifolds of co-dimension one in [44]. Although one can apply other domain decomposition methods to the CPM, we herein mainly focus on the parallel and alternating Schwarz methods.

Before the computation begins, an appropriate decomposition of the domain is needed. Before detailing the decomposition at the discrete level, we state the partitioning at the continuous level, explained in the following definition.

Definition 2.2.1. Suppose the closed manifold $\mathcal{S}$ is split into N disjoint subdomains, each called $\tilde{\mathcal{S}}_j$ for $j = 1, \dots, N$. For a parallel algorithm, the ordering of the subdomains is not important as they all will be solved simultaneously. There is a family of domain decomposition methods introduced later in this chapter in which the ordering becomes notable. Hence, we order the subdomains in a way that $\tilde{\mathcal{S}}_j$ for $j = 2, \dots, N$ is adjacent to at least one of its previous subdomains on the list. That is, $\tilde{\mathcal{S}}_j$ has at least a common interface with $\tilde{\mathcal{S}}_k$ for $k = 1, \dots, j-1$. Note that there is no condition on the first subdomain. After having a set of disjoint subdomains, we expand each subdomain by a desired amount in the normal directions to the interfaces to form the overlapping subdomains, $\mathcal{S}_j$, for $j = 1, \dots, N$. We define $\gamma_{jk} := \partial\mathcal{S}_j \cap \mathcal{S}_k$, $j \neq k$, as the part of the boundary of the j^{th} overlapping subdomain located within the k^{th} overlapping subdomain. Now that a partitioning of the underlying geometry is in hand, we attempt to construct the overlapping subdomains for the CPM. Recall that the computational domain of the CPM is a tubular region around the manifold denoted as Ω, and the closest point representation of the manifold $\mathcal{S}$ is well-defined. The disjoint subdomain $\tilde{\Omega}_j$, $j = 1, \dots, N$, consists of all $x \in \Omega$ such that $\mathrm{cp}(x) \in \tilde{\mathcal{S}}_j$. Likewise, all $x \in \Omega$ such that $\mathrm{cp}(x) \in \mathcal{S}_j$ create the overlapping subdomain j for the CPM, Ω_j. Recall that before applying the CPM, a tubular neighbourhood around the manifold is

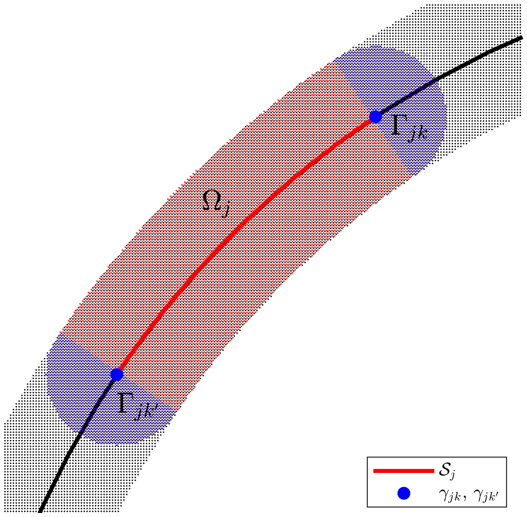

Figure 2.4: Illustration of the domain decomposition for the CPM at the continuous level detailed in Definition 2.2.1.

needed, while there is no such tube around the boundaries of the overlapping subdomains. This is more clear at the discrete level as the interpolation stencil associated with the CPM is not complete for the boundary nodes. In order to address the issue, we define the part of the boundary for the overlapping subdomain j lying in the subdomain k to be $\Gamma_{jk} := \{x \in \Omega_k | ||\gamma_{jk} - x|| \leq \lambda\}$ where λ is defined in Equation (2.5), and $||\cdot||$ denotes the Euclidean distance. It also gives a modification to the closest point representation of the subdomain j:

$$\mathrm{cp}_{\mathcal{S}_j}(x) = \begin{cases} \mathrm{cp}_{\mathcal{S}}(x); & x \in \Omega_j, \\ \\ \underset{s \in \gamma_{jk}}{\arg\min} ||x - s||; & x \in \Gamma_{jk}, k \neq j. \end{cases} \tag{2.8}$$

Definition 2.2.1 provides the details on the partitioning of the computational domain of the CPM at the continuous level which is sufficient for our analysis. See Figure 2.4 for an illustration. The black curve represents $\mathcal{S}$, and the black shaded area depicts the computational domain of the CPM, Ω.

Definition 2.2.1 provides no practical information on partitioning at the discrete level. We will introduce the partitioning at the discrete level in Chapter 4. A thorough explanation at the discrete level also can be found in [44].

Now with a rigorous partitioning of the closed manifold $\mathcal{S}$ detailed in Definition 2.2.1, the Schwarz-CPM for the positive surface intrinsic Helmholtz equation (1.1) reads:

$$\begin{cases} (c - \Delta_h^{\#})\tilde{u}_j^{n+1}(\mathrm{cp}_{\mathcal{S}_j}) = f(\mathrm{cp}_{\mathcal{S}_j}), & \text{in } \Omega_j, \\ \\ \mathcal{B}\tilde{u}_j^{n+1}(\mathrm{cp}_{\mathcal{S}_j}) = \mathcal{B}\tilde{u}_k^{{n+1}_{jk}^{(\mathrm{method})}}(\mathrm{cp}_{\mathcal{S}_j}), & \text{on } \Gamma_{jk}, k \neq j, \end{cases} \tag{2.9}$$

where the symbol $1_{jk}^{(\text{method})}$ is defined as

$$1_{jk}^{(\text{method})} = \begin{cases} 0; & \text{method} = 1, \\ 0; & \text{method} = 2, \quad j < k, \\ 1; & \text{method} = 2, \quad j > k, \end{cases} \tag{2.10}$$

method = 1 represents the parallel Schwarz methods, while method = 2 represents alternating Schwarz algorithm.

Parallel Schwarz algorithms are members of the vast family of Schwarz domain decomposition methods. These algorithms are iterative methods which concurrently solve subproblems and are perfect fits for parallel computing. One can simultaneously pass each subproblem to a different computational unit. Then, we modify the subproblems according to the solution of the adjacent subproblems on the central processing unit and pass the new subproblems to the computational units for the next iteration. We iterate until a desired convergence criteria is met.

Alternating Schwarz algorithms benefit from the most recent available information, and subsequently show better convergence as compared to parallel Schwarz algorithms. In these algorithms, each subproblem at an iteration is modified and solved based on the previous subproblems solved at the same iteration. If a subproblem has not been solved yet in the ongoing iteration, we use its solution at the previous iteration. Therefore, these methods are not capable of parallelism. Starting from the first subproblem $j = 1$ with boundary values obtained from the previous iteration n, one obtains $\tilde{u}_1^{n+1}$. By using the new solution obtained for the first subdomain $\tilde{u}_1^{n+1}$, the boundary values for the adjacent subproblem $j = 2$ are updated and its solution is computed.

It is possible to define different boundary operators $\mathcal{B}_k$ in Equation (2.9) for each interface k. This could improve the convergence of the iteration but increases the complexity of the analysis. Therefore, we only consider the case where the boundary operators remain the same among the interfaces, i.e., $\mathcal{B}_k = \mathcal{B}$.

Herein, we only investigate two well-known boundary operators. Assuming the boundary operator is the identity operator, i.e., $\mathcal{B} = \mathcal{I}$, we arrive at the classical Schwarz method which transmits the information subdomain-by-subdomain through Dirichlet boundary conditions. For a better performance, one can utilize the Robin boundary condition by setting $\mathcal{B} = \partial/\partial\hat{n} + \alpha$ where $\hat{n}$ denotes the outward normal to the interface and α is called the Robin parameter. This approach is called the optimized Schwarz method. It benefits from a better transmission of information throughout the subdomains at the cost of a more difficult implementation.

Using the two introduced algorithms – parallel and alternating Schwarz – and the identity and Robin boundary operators gives four Schwarz-CPM methods which are introduced in the following sections. Convergence analysis for these methods is provided in the next section.

2.2.1 Classical Parallel Schwarz

Assuming the identity operator for the boundary condition, i.e., $\mathcal{B} = \mathcal{I}$, Iteration (2.9) reduces to:

$$\begin{cases} (c - \Delta_h^{\#})\tilde{u}_j^{n+1}(\mathrm{cp}_{\mathcal{S}_j}) = f(\mathrm{cp}_{\mathcal{S}_j}), & \text{in } \Omega_j, \\ \tilde{u}_j^{n+1}(\mathrm{cp}_{\mathcal{S}_j}) = \tilde{u}_k^{n}(\mathrm{cp}_{\mathcal{S}_j}), & \text{on } \Gamma_{jk}, k \neq j. \end{cases} \tag{2.11}$$

We call this algorithm the Classical Parallel Schwarz for the CPM (CPS-CPM). This iteration is anticipated to have the slowest rate of convergence as it does not benefit from the newest available data in the alternating Schwarz methods nor does it use the extensive transmission of information associated with the Robin operator.

2.2.2 Classical Alternating Schwarz

From the definition of the alternating Schwarz methods and using the identity operator as the boundary operator, the Classical Alternating Schwarz applied to the CPM (CAS-CPM) for equation (1.1) reads:

$$\begin{cases} (c - \Delta_h^{\#})\tilde{u}_j^{n+1}(\mathrm{cp}_{\mathcal{S}_j}) = f(\mathrm{cp}_{\mathcal{S}_j}), & \text{in } \Omega_j, \\ \tilde{u}_j^{n+1}(\mathrm{cp}_{\mathcal{S}_j}) = \tilde{u}_k^{n+1}(\mathrm{cp}_{\mathcal{S}_j}), & \text{on } \Gamma_{jk}, k < j, \\ \tilde{u}_j^{n+1}(\mathrm{cp}_{\mathcal{S}_j}) = \tilde{u}_k^{n}(\mathrm{cp}_{\mathcal{S}_j}), & \text{on } \Gamma_{jk}, k > j. \end{cases} \tag{2.12}$$

2.2.3 Optimized Parallel Schwarz

By choosing the Robin boundary condition for the transmission operator, i.e., $\mathcal{B} = \partial/\partial\hat{n} + \alpha$, we arrive at Optimized Parallel Schwarz for the CPM (OPS-CPM):

$$\begin{cases} (c - \Delta_h^{\#})\tilde{u}_j^{n+1}(\mathrm{cp}_{\mathcal{S}_j}) = f(\mathrm{cp}_{\mathcal{S}_j}), & \text{in } \Omega_j, \\ \dfrac{\partial}{\partial\hat{n}}\tilde{u}_j^{n+1}(\mathrm{cp}_{\mathcal{S}_j}) + \alpha\tilde{u}_j^{n+1}(\mathrm{cp}_{\mathcal{S}_j}) = \dfrac{\partial}{\partial\hat{n}}\tilde{u}_k^{n}(\mathrm{cp}_{\mathcal{S}_j}) + \alpha\tilde{u}_k^{n}(\mathrm{cp}_{\mathcal{S}_j}), & \text{on } \Gamma_{jk}, k \neq j. \end{cases} \tag{2.13}$$

2.2.4 Optimized Alternating Schwarz

Similarly, the Optimized Alternating Schwarz method applied to the CPM (OAS-CPM) for equation (1.1) reads:

$$\begin{cases} (c-\Delta_h^{\#})\tilde{u}_j^{n+1}(\mathrm{cp}_{\mathcal{S}_j}) = f(\mathrm{cp}_{\mathcal{S}_j}), & \text{in } \Omega_j, \\ \dfrac{\partial}{\partial \hat{n}}\tilde{u}_j^{n+1}(\mathrm{cp}_{\mathcal{S}_j}) + \alpha \tilde{u}_j^{n+1}(\mathrm{cp}_{\mathcal{S}_j}) = \dfrac{\partial}{\partial \hat{n}}\tilde{u}_k^{n+1}(\mathrm{cp}_{\mathcal{S}_j}) + \alpha \tilde{u}_k^{n+1}(\mathrm{cp}_{\mathcal{S}_j}), & \text{on } \Gamma_{jk}, k<j, \\ \dfrac{\partial}{\partial \hat{n}}\tilde{u}_j^{n+1}(\mathrm{cp}_{\mathcal{S}_j}) + \alpha \tilde{u}_j^{n+1}(\mathrm{cp}_{\mathcal{S}_j}) = \dfrac{\partial}{\partial \hat{n}}\tilde{u}_k^{n}(\mathrm{cp}_{\mathcal{S}_j}) + \alpha \tilde{u}_k^{n}(\mathrm{cp}_{\mathcal{S}_j}), & \text{on } \Gamma_{jk}, k>j. \end{cases} \tag{2.14}$$

This iteration is anticipated to have the best convergence rate among the introduced methods as it gains benefit from both alternating iterates and the Robin operator.

In this format of Schwarz algorithm, there is no concept of a global solution. In order to construct the global solution, a weighted average of subdomain solutions is utilized. Throughout the thesis, we construct the global solution by gluing together the portion of local solutions restricted to their disjoint subdomains. This gives classical or optimized restricted additive Schwarz (RAS) methods.

Chapter 3

Convergence of the DDCPM

We wish to prove the convergence of the domain decomposition algorithms introduced in Chapter 2. Numerical experiments in [44] suggest that the classical and optimized parallel Schwarz methods coupled with the CPM are convergent. In this chapter, we prove the convergence of the Schwarz-CPM equation (2.9) for a one-manifold for two different iterations and with the two different transmission operators.

3.1 Convergence of the Schwarz-CPM

This section begins with a fundamental theorem relating the Schwarz-CPM to an equivalent Schwarz domain decomposition iteration at the continuous level.

Theorem 3.1.1. Consider the following Schwarz-CPM applied to the positive surface intrinsic Helmholtz equation (1.1) on a closed, smooth manifold $\mathcal{S}$ with the partitioning detailed in Definition 2.2.1:

$$\begin{cases} (c - \Delta_h^{\#})\tilde{u}_j^{n+1}(\mathrm{cp}_{\mathcal{S}_j}) = f(\mathrm{cp}_{\mathcal{S}_j}), & \text{in } \Omega_j, \\ \mathcal{B}\tilde{u}_j^{n+1}(\mathrm{cp}_{\mathcal{S}_j}) = \mathcal{B}\tilde{u}_k^{{n+1}_{jk}^{(\text{method})}}(\mathrm{cp}_{\mathcal{S}_j}), & \text{on } \Gamma_{jk}, k \neq j, \end{cases}$$

In the limit $h \to 0$, this is equivalent to:

$$\begin{cases} (c - \Delta_{\mathcal{S}})u_j^{n+1} = f, & \text{in } \mathcal{S}_j, \\ \mathcal{B}u_j^{n+1} = \mathcal{B}u_k^{{n+1}_{jk}^{(\text{method})}}, & \text{on } \gamma_{jk}, k \neq j, \end{cases} \tag{3.1}$$

for $j, k = 1, \dots, N$, where u is the solution on the manifold.

Proof. For a closed, smooth manifold $\mathcal{S}$, the regularized operator is consistent with the Laplace operator on the manifold [43]. Moreover, the CPM without the regularization is consistent with the surface intrinsic PDE problems in the limit $h \to 0$ where h denotes the mesh size. This yields our result. □

Theorem 3.1.1 plays an important role in our analysis. In order to prove the convergence of the Schwarz-CPM at the continuous level for a closed, smooth manifold with a well-defined closest point representation, the theorem suggests that it is sufficient to show the convergence of the equivalent Schwarz method. Notice that the limit $h \to 0$ yields the continuous problem.

Furthermore, we may use the linearity of the positive surface intrinsic Helmholtz equation (1.1) to remove f from the Schwarz method in (3.1). We define the subdomain error,

$$\epsilon_j = u_j - u\Big|_{\mathcal{S}_j},$$

where $u\Big|_{\mathcal{S}_j}$ is the exact solution on subdomain j for $j = 1, \ldots, N$. Thus, from the linearity of Equation (1.1), we have the following iteration for the subdomains error for $j, k = 1, \ldots, N$:

$$\begin{cases} (c - \Delta_{\mathcal{S}})\epsilon_j^{n+1} = 0, & \text{in } \mathcal{S}_j, \\ \mathcal{B}\epsilon_j^{n+1} = \mathcal{B}\epsilon_k^{{n+1}_{jk}^{(\text{method})}}, & \text{on } \gamma_{jk}, k \neq j. \end{cases} \tag{3.2}$$

Equation (3.2) is a homogeneous PDE which is easier to solve than the non-homogeneous PDE of Equation (3.1). Note that both share the same convergence behaviour.

To provide a rigorous proof of convergence for Iteration (3.2), we need to analytically solve the PDE. In general, it is not possible to obtain an analytic solution for Equation (3.2). We therefore introduce some simplifications on the manifold to help us to find the solution. For instance, if we assume that $\mathcal{S}$ is a curve in $\mathbb{R}^d$ (i.e., of dimension one) then the Laplace-Beltrami operator $\Delta_{\mathcal{S}}$ becomes the ordinary differential operator $\mathrm{d}^2/\,\mathrm{d}s^2$ where s denotes the arclength.

Theorem 3.1.1 indicates that the Schwarz-CPM converges with the same rate that the equivalent Schwarz method converges at the continuous level. Thus, our problem has reduced to the convergence of the equivalent Schwarz method on the manifold. That is, supposing $\mathcal{S}$ is a curve, we are required to show convergence of iterations (3.1). Convergence of the classical alternating Schwarz for the 1D positive Helmholtz equation with two subdomains is investigated in [16] where the boundary conditions of the differential equation are the homogeneous Dirichlet. Herein, we consider simple closed one-manifolds where the boundary condition is naturally periodic. The convergence of Equation (3.1) on closed one-manifolds has not been widely investigated. In [48], the convergence of (3.1) is studied on the unit circle partitioned into two equal-sized subdomains. The partitioning arising from the Schwarz-CPM problems in (2.9) is performed within the embedding space. As a consequence, our subdomains are more likely to be unequal. This motivates us to investigate the convergence of the methods for an unequal-sized partitioning of a closed curve in $\mathbb{R}^d$. Furthermore, we restrict the closed manifold to be simple. That is, the manifold does not self-intersect.

To start analyzing this case, we need to refine the subdomain definitions. The following definition provides essential details for the subdomains in the 1-manifold case.

Definition 3.1.1 (Subdomains for 1-Manifolds)**.** We introduce N disjoint subdomains and let them be $\tilde{\mathcal{S}}_j$, $j = 1, \ldots, N$. We parameterize the one-manifold by arclength s starting at a boundary of $\tilde{\mathcal{S}}_1$. Next, by extending the disjoint subdomains, we let the overlapping subdomains be $\mathcal{S}_j = [a_j, b_j]$ and define $\ell_j \equiv b_j - a_j$ to be the subdomain lengths. Further, let δ_j denote the subdomain overlaps given by:

$$\delta_j = \begin{cases} b_j - a_{j+1}, & j = 1, \ldots, N-1, \\ \\ b_N - (a_1 + L), & j = N. \end{cases}$$

Now, we establish some restrictions on the introduced parameters. First, $\ell_j = b_j - a_j > 0$ to avoid negative length for the subdomains. To ensure that the whole curve is included, we set $a_1 \leq 0$ and $b_N \geq L$ where L is the curve length. We also assume $\delta_{j-1} + \delta_j < \ell_j$, otherwise subdomain j would be enfolded by the overlap of the adjacent subdomains. In this case, subdomains $j-1$ and $j+1$ are overlapping, and consequently, we can eliminate subdomain j. Finally, negative overlaps are not permitted, i.e., we require $\delta_j \geq 0$, otherwise our partitioning would not cover the original manifold. In addition, we define an overlapping partitioning by restricting the overlap parameters to be positive, i.e., $\delta_j > 0$ for all subdomains.

Remark. Since the periodicity is intrinsic to closed manifolds, we set $\delta_0 \equiv \delta_N$ and $\delta_{N+1} \equiv \delta_1$ throughout the thesis for ease of notation.

Before beginning the proof of convergence, we provide a careful definition of equal-sized partitioning since it is central to our analysis.

Definition 3.1.2 (Equal-Sized Subdomains for 1-Manifolds)**.** Borrowing the parameters introduced in Definition 3.1.1 for an equal-sized partitioning of a curve with length L, we have N disjoint partitions each with the length of L/N. Extending the disjoint subdomains by $\delta/2$ from each side, we arrive at the subdomain lengths $L/N + \delta$. Notice that $\delta_j = \delta$ and $\ell_j = \ell = L/N + \delta$ for all $j = 1, \ldots, N$. Following the discussion in Definition 3.1.1 regarding the restrictions, we have $0 \leq \delta < L/N$ in this case. Note that for an overlapping partitioning, the inequality becomes $0 < \delta < L/N$.

Using the assumption that $\mathcal{S}$ is a 1-manifold partitioned according to Definition 3.1.1, we rewrite Equation (3.2) as:

$$\begin{cases} (c - \dfrac{\mathrm{d}^2}{\mathrm{d}s^2})\epsilon_j^{n+1} = 0, & \text{for } s \in [a_j, b_j], \\ \mathcal{B}\epsilon_j^{n+1}(a_j) = \mathcal{B}\epsilon_{j-1}^{n+1^{(\text{method})}}(a_j), & \\ \mathcal{B}\epsilon_j^{n+1}(b_j) = \mathcal{B}\epsilon_{j+1}^{n}(b_j), & \end{cases} \tag{3.3}$$

for $j = 1, \ldots, N$ where

$$1^{(\text{method})} = \begin{cases} 0; & \text{method} = 1, \\ 1; & \text{method} = 2, \end{cases}$$

where method $= 1$ represents the parallel Schwarz methods, while method $= 2$ represents alternating Schwarz algorithm.

Remark. The boundary conditions of the first and last subdomains are $\mathcal{B}\epsilon_1^{n+1}(a_1) = \mathcal{B}\epsilon_0^{n+1^{(\text{method})}}(a_1)$ and $\mathcal{B}\epsilon_N^{n+1}(b_N) = \mathcal{B}\epsilon_{N+1}^{n}(b_N)$, respectively. We need to clarify the notation since the terms $\mathcal{B}\epsilon_0^{n}(a_1)$ and $\mathcal{B}\epsilon_{N+1}^{n}(b_N)$ are not explicitly defined. Hence, we set

$$\mathcal{B}\epsilon_0^{n+1^{(\text{method})}}(a_1) \equiv \mathcal{B}\epsilon_N^{n}(a_1 + L), \qquad \mathcal{B}\epsilon_{N+1}^{n}(b_N) \equiv \mathcal{B}\epsilon_1^{n+1^{(\text{method})}}(b_N - L). \tag{3.4}$$

We added (and subtracted) the manifold length L because ϵ_N^n (and ϵ_1^n) is not defined for a_1 (and b_N), hence, we use the periodicity of the problem to evaluate ϵ_N^n (and ϵ_1^n) at the mirror point $a_1 + L$ (and $b_{N_S} - L$). This is done for the sake of simplicity, however, one can suggest different equations for $j = 1$, $1 < j < N$, and $j = N$. Equation (3.4) is applicable throughout this thesis.

We say a domain decomposition iteration is convergent if and only if ϵ_j converges to zero for all j. Moreover, by the maximum principle for Equation (3.3), the maximum of $|\epsilon_j|$ occurs at the boundaries. Note that we can still utilize the maximum principle for the Robin boundary condition [26]. Therefore, ϵ_j converges to zero if and only if the boundary values converge to zero. Thus, the ultimate goal is to evaluate boundary values at each iteration and determine how fast they decay.

Equation (3.3) is a system of decoupled ordinary differential equations and can be solved analytically if the boundary operator and the iterating option are specified. Since the solution depends on the boundary operator and the choice of iteration, we need to separately prove the convergence for the different boundary operators.

3.1.1 The CPS-CPM

Using Theorem 3.1.1 and the subdomains detailed in Definition 3.1.1, the CPS-CPM algorithm (2.11) for the positive surface intrinsic Helmholtz equation on a closed, smooth

1-manifold is equivalent to the following reduction of Equation (3.3) at the continuous level:

$$\begin{cases} (c - \dfrac{\mathrm{d}^2}{\mathrm{d}s^2})\epsilon_j^{n+1} = 0, \qquad \text{for } s \in [a_j, b_j], \\ \epsilon_j^{n+1}(a_j) = \epsilon_{j-1}^n(a_j), \\ \epsilon_j^{n+1}(b_j) = \epsilon_{j+1}^n(b_j). \end{cases} \tag{3.5}$$

This has the solution

$$\epsilon_j^{n+1}(s) = \frac{e^{\sqrt{c}(s-a_j)} - e^{\sqrt{c}(b_j - s + \ell_j)}}{1 - e^{2\sqrt{c}\ell_j}} \epsilon_{j-1}^n(a_j) + \frac{e^{\sqrt{c}(b_j - s)} - e^{\sqrt{c}(s - a_j + \ell_j)}}{1 - e^{2\sqrt{c}\ell_j}} \epsilon_{j+1}^n(b_j), \tag{3.6}$$

for $j = 1, \ldots, N$. Note that (3.4) still applies to Equation (3.6).

We define an error vector at iteration n which is comprised of the error values at the boundaries:

$$\boldsymbol{\epsilon}^n := [\epsilon_1^n(b_N - L), \epsilon_1^n(a_2), \epsilon_2^n(b_1), \epsilon_2^n(a_3), \ldots, \epsilon_N^n(b_{N-1}), \epsilon_N^n(a_1 + L)]^T. \tag{3.7}$$

One can evaluate the errors at the boundaries using the solution provided in Equation (3.6) in terms of the error values at the boundaries in the previous iteration:

$$\begin{cases} \epsilon_j^{n+1}(b_{j-1}) = p_j \epsilon_{j-1}^n(a_j) + r_j \epsilon_{j+1}^n(b_j), \\ \epsilon_j^{n+1}(a_{j+1}) = s_j \epsilon_{j-1}^n(a_j) + q_j \epsilon_{j+1}^n(b_j), \end{cases} \tag{3.8}$$

where for $j = 1, \ldots, N$,

$$\begin{aligned} p_j &= \frac{1 - e^{2\sqrt{c}(\ell_j - \delta_{j-1})}}{1 - e^{2\sqrt{c}\ell_j}} e^{\sqrt{c}\delta_{j-1}}, & r_j &= \frac{1 - e^{2\sqrt{c}\delta_{j-1}}}{1 - e^{2\sqrt{c}\ell_j}} e^{\sqrt{c}(\ell_j - \delta_{j-1})}, \\ q_j &= \frac{1 - e^{2\sqrt{c}(\ell_j - \delta_j)}}{1 - e^{2\sqrt{c}\ell_j}} e^{\sqrt{c}\delta_j}, & s_j &= \frac{1 - e^{2\sqrt{c}\delta_j}}{1 - e^{2\sqrt{c}\ell_j}} e^{\sqrt{c}(\ell_j - \delta_j)}, \end{aligned} \tag{3.9}$$

are constants depending only on the partitioning.

Now that the error values at the boundaries at iteration $n+1$ are evaluated in terms of the error values at the boundaries at iteration n in Equation (3.8), we may collect them in matrix form using the quantities defined in (3.9),

$$\boldsymbol{\epsilon}^{n+1} = \mathbf{M}_{\mathrm{CPS}} \boldsymbol{\epsilon}^n, \tag{3.10}$$

where $\mathbf{M}_{\text{CPS}}$ is a $2N \times 2N$ matrix called the iteration matrix for the classical parallel Schwarz method, and is given by

$$\mathbf{M}_{\text{CPS}} = \left[\begin{array}{ccccccccccccc}
0 & 0 & r_1 & & & & & & & & & & p_1 \\
0 & 0 & q_1 & & & & & & & & & & s_1 \\
 & p_2 & 0 & 0 & r_2 & & & & & & & & \\
 & s_2 & 0 & 0 & q_2 & & & & & & & & \\
 & & & p_3 & 0 & 0 & r_3 & & & & & & \\
 & & & s_3 & 0 & 0 & q_3 & & & & & & \\
 & & & & & \ddots & \ddots & \ddots & \ddots & & & & \\
 & & & & & & \ddots & \ddots & \ddots & \ddots & & & \\
 & & & & & & & & p_{N-1} & 0 & 0 & r_{N-1} & \\
 & & & & & & & & s_{N-1} & 0 & 0 & q_{N-1} & \\
r_N & & & & & & & & & & p_N & 0 & 0 \\
q_N & & & & & & & & & & s_N & 0 & 0
\end{array}\right]. \tag{3.11}$$

Definition 3.1.3. We define the convergence factor κ as the ratio of the ∞-norm of the error vector at two consecutive steps,

$$\kappa = \frac{||\boldsymbol{\epsilon}^{n+1}||_\infty}{||\boldsymbol{\epsilon}^{n}||_\infty}.$$

Note that for the equation $\boldsymbol{\epsilon}^{n+1} = \mathbf{M}\boldsymbol{\epsilon}^{n}$, $||\mathbf{M}||_\infty$ is an upper bound for the convergence factor since $||\boldsymbol{\epsilon}^{n+1}||_\infty \leq ||\mathbf{M}||_\infty ||\boldsymbol{\epsilon}^{n}||_\infty$. That is,

$$\kappa \leq ||\mathbf{M}||_\infty.$$

To prove the convergence, the following lemma and corollaries for the quantities defined in Equation (3.9) are essential for the analysis.

Lemma 3.1.2. For a partitioning as specified in Definition 3.1.1 with overlap ($\delta_j > 0$ for $1 \leq j \leq N$), the following inequalities hold for the quantities introduced in (3.9):

$$|p_j| + |r_j| < 1,$$
$$|q_j| + |s_j| < 1.$$

Proof. From the restrictions partitioning in Definition 3.1.1 with overlap, we have $\delta_{j-1} + \delta_j < \ell_j$ and $\delta_j > 0$. The assumptions $\delta_{j-1} + \delta_j < \ell_j$ and $\delta_j > 0$ together result in $0 < \delta_{j-1} < \ell_j$ and $0 < \delta_j < \ell_j$. Thus, we obtain $e^{2\sqrt{c}(\ell_j - \delta_{j-1})} > 1$, $e^{2\sqrt{c}(\ell_j - \delta_j)} > 1$, $e^{2\sqrt{c}\delta_{j-1}} > 1$, and $e^{2\sqrt{c}\delta_j} > 1$. The denominators in (3.9) are negative, hence,

$$p_j, r_j, q_j, s_j > 0.$$

Applying this and (3.9),

$$\begin{aligned}
|p_j| + |r_j| &= p_j + r_j, \\
&= \frac{e^{\sqrt{c}\delta_{j-1}} - e^{\sqrt{c}(2\ell_j - \delta_{j-1})}}{1 - e^{2\sqrt{c}\ell_j}} + \frac{e^{\sqrt{c}(\ell_j - \delta_{j-1})} - e^{\sqrt{c}(\ell_j + \delta_{j-1})}}{1 - e^{2\sqrt{c}\ell_j}}, \\
&= \frac{e^{\sqrt{c}\delta_{j-1}}(1 - e^{\sqrt{c}\ell_j}) + e^{\sqrt{c}(\ell_j - \delta_{j-1})}(1 - e^{\sqrt{c}\ell_j})}{1 - e^{2\sqrt{c}\ell_j}}, \\
&= \frac{(e^{\sqrt{c}\delta_{j-1}} + e^{\sqrt{c}(\ell_j - \delta_{j-1})})(1 - e^{\sqrt{c}\ell_j})}{1 - e^{2\sqrt{c}\ell_j}}, \\
&= \frac{e^{\sqrt{c}(\ell_j - \delta_{j-1})} + e^{\sqrt{c}\delta_{j-1}}}{e^{\sqrt{c}\ell_j} + 1}, \\
&= 1 + \frac{e^{\sqrt{c}(\ell_j - \delta_{j-1})} - e^{\sqrt{c}\ell_j} + e^{\sqrt{c}\delta_{j-1}} - 1}{e^{\sqrt{c}\ell_j} + 1}, \\
&= 1 + \frac{e^{\sqrt{c}\ell_j}(e^{-\sqrt{c}\delta_{j-1}} - 1) - e^{\sqrt{c}\delta_{j-1}}(e^{-\sqrt{c}\delta_{j-1}} - 1)}{e^{\sqrt{c}\ell_j} + 1}, \\
&= 1 + (e^{-\sqrt{c}\delta_{j-1}} - 1) \cdot \frac{e^{\sqrt{c}\ell_j} - e^{\sqrt{c}\delta_{j-1}}}{e^{\sqrt{c}\ell_j} + 1}, \\
&< 1,
\end{aligned}$$

where the last inequality uses $e^{-\sqrt{c}\delta_{j-1}} < 1$ and $e^{\sqrt{c}\ell_j} > e^{\sqrt{c}\delta_{j-1}}$. Similarly,

$$|q_j| + |s_j| < 1,$$

and the proof is complete. □

Now, the proof of convergence for the CPS algorithm shown in Equation (3.5) is given by the following theorem.

Theorem 3.1.3. Under the restrictions on the partitioning of the 1-manifold $\mathcal{S}$ detailed in Definition 3.1.1 with $\delta_j \neq 0$ for all j, the CPS iterations (3.5), with $N \geq 2$, for the positive Helmholtz equation on any closed 1-manifold converges globally on an arbitrary number of subdomains.

Proof. We must show the spectral radius of the iteration matrix is less than one, i.e., $\rho(\mathbf{M}_{\text{CPS}}) < 1$, to prove the convergence. Any submultiplicative matrix norm is an upper bound for the spectral radius. By picking the ∞-norm, we have

$$\rho(\mathbf{M}_{\text{CPS}}) \leq ||\mathbf{M}_{\text{CPS}}||_\infty.$$

Therefore, convergence is obtained if $||\mathbf{M}_{\text{CPS}}||_\infty < 1$. In addition, the max-norm is equal to the maximum of the absolute row sums. Then, the max-norm of $\mathbf{M}_{\text{CPS}}$ is

$$||\mathbf{M}_{\text{CPS}}||_\infty = \max\{|p_1| + |r_1|, |q_1| + |s_1|, \ldots, |p_N| + |r_N|, |q_N| + |s_N|\}.$$

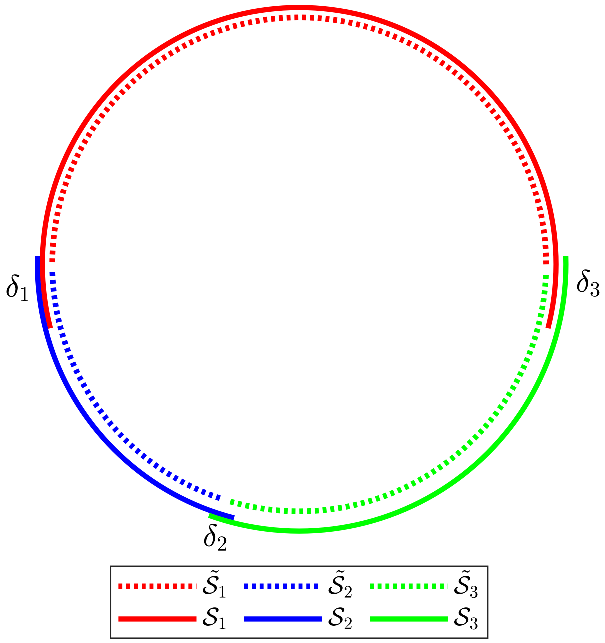

Figure 3.1: Three disjoint and overlapping subdomains for the unit circle.

In Lemma 3.1.2, we have shown that $|p_j| + |r_j| < 1$ and $|q_j| + |s_j| < 1$ for all $j = 1, \ldots, N$ for the partitioning explained in Definition 3.1.1 with overlap. Consequently,

$$\rho(\mathbf{M}_{\text{CPS}}) \leq ||\mathbf{M}_{\text{CPS}}||_\infty = \max\{|p_1| + |r_1|, |q_1| + |s_1|, \ldots, |p_N| + |r_N|, |q_N| + |s_N|\} < 1.$$

Hence, the algorithm is convergent for any finite number of subdomains as long as they overlap. □

We now numerically verify the result in Theorem 3.1.3. Iterations (3.5) are implemented in MATLAB. The closed one-manifold $\mathcal{S}$ is given as a set of discrete points in $\mathbb{R}^d$. The disjoint subdomains are created by splitting the one-manifold by some desired ratios. Next, given a set of integers N_o that denotes the number of overlapping nodes, we form the overlapping subdomains. Figure 3.1 depicts a partitioning of the unit circle with three unequal-sized subdomains and different overlaps. The dotted curves are disjoint subdomains, while the solid lines correspond to the overlapping partitioning.

The positive Helmholtz equation is locally discretized using a second-order centred finite difference scheme for each subdomain. By identifying the boundary nodes in each overlapping subdomain, the Dirichlet boundary conditions can be simply enforced. Using $c = 1$ and the initial guess $u(s) = 1$, the solution at several iterations are shown in Figure 3.2. To construct the global solution, the local solutions at the disjoint parts are glued together, i.e., $\epsilon^n = \bigcup_{j=1}^{N} \epsilon_j^n\Big|_{\tilde{\mathcal{S}}_j}$. In Figure 3.2, the maximum of error occurs at $s = b_2$. To verify Theorem 3.1.3, we provide Figure 3.3 which illustrates the max-norm of the error vector (3.8)

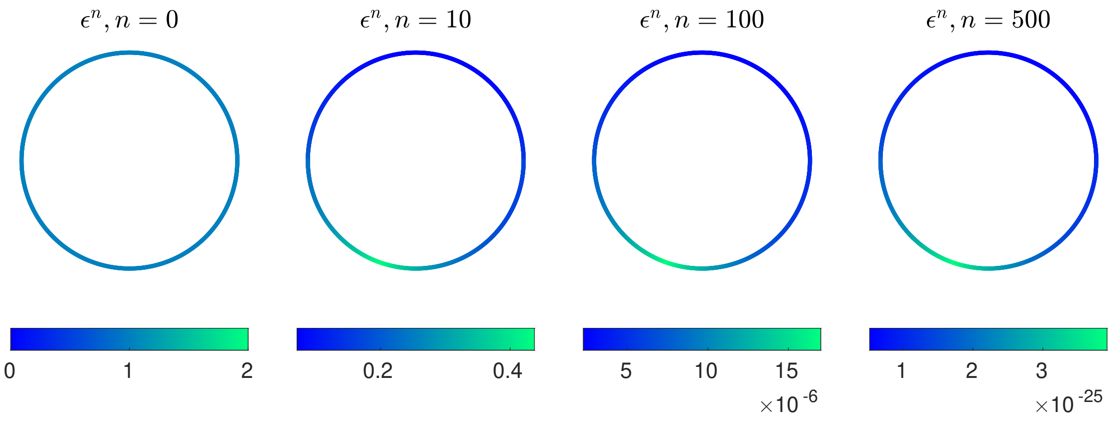

Figure 3.2: Global solution to (3.5) on the unit circle at different iterations with $c = 1$.

over different iterations along with the theoretical convergence factor and an upper bound found in Theorem 3.1.3. The theoretical error in the figure is an error decaying with the theoretical convergence factor, $\rho(\mathbf{M}_{\text{CPS}})$. The theoretical convergence factor is computed by explicitly constructing the iteration matrix and determining the spectral radius. In addition, the upper bound on the theoretical error is obtained by multiplying the initial error by $||\mathbf{M}_{\text{CPS}}||_\infty$. Figure 3.3 clearly verifies our analysis for the CPS method. The algorithm converges with the convergence factor $\rho(\mathbf{M}_{\text{CPS}})$, and the convergence factor κ is bounded by $||\mathbf{M}_{\text{CPS}}||_\infty$.

Since our theoretical analysis has been carried out at the continuous level, we should ensure that the computations are independent of the mesh size Δs. The convergence behaviours with three mesh sizes $\Delta s = \pi/500, \pi/1000, \pi/2000$ are shown in Figure 3.4. As we observe, the decay rates are quite similar since the error plots are parallel. It indicates that the experiments are mesh independent. We have to address the fact that the simulations for $\Delta s = \pi/500, \pi/1000, \pi/2000$ are not identical. When we halve the mesh size, N_o must be doubled to keep the partitioning the same. However, since the overlapping subdomains are constructed by adding N_o discrete points to the corresponding disjoint subdomains, the overlapping subdomains obtained from different mesh sizes are not identical due to numerical round-off errors. We provide an example to clarify this. The overlapping subdomains shown in Figure 3.1 are $\mathcal{S}_1 = [-0.25133, 3.3929]$, $\mathcal{S}_2 = [3.0819, 4.4611]$, and $\mathcal{S}_3 = [4.3385, 6.3429]$, while doubling the resolution and N_o yields $\mathcal{S}_1 = [-0.25133, 3.3929]$, $\mathcal{S}_2 = [3.0803, 4.4611]$, and $\mathcal{S}_3 = [4.337, 6.3444]$. These slight changes in the subdomains result in slightly different theoretical convergence factors. We have ensured that the results obtained in the future sections are mesh independent, but we omit the discussion on mesh-independency.

We now explore the case where subdomains are identical in terms of length and overlap. This is an ideal setup which equally distributes computational load to each processor unit.

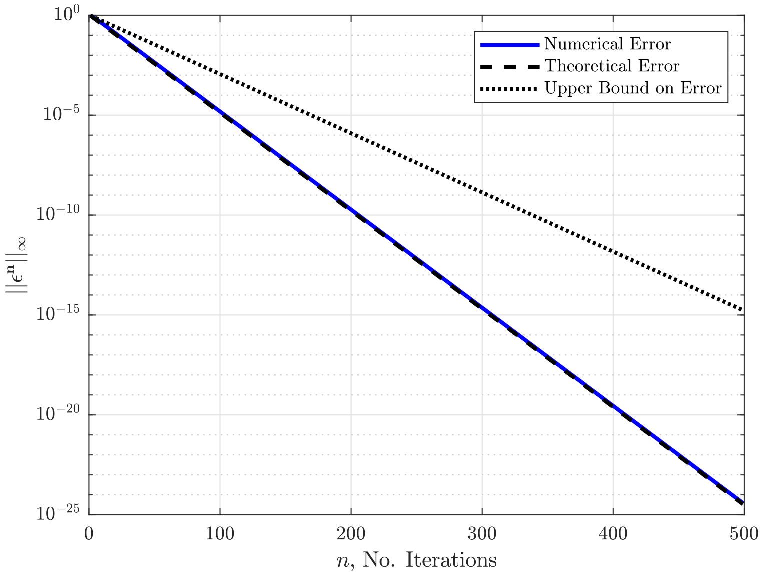

Figure 3.3: Error decay for (3.5) with $c = 1$ on the unit circle shown in Figure 3.1.

Corollary 3.1.1. For an equal-sized overlapping partitioning of a simple closed 1-manifold $\mathcal{S}$ based on Definition 3.1.2, the CPS iterations (3.5) with $N \geq 2$ for the positive Helmholtz equation on $\mathcal{S}$ converges globally on an arbitrary number of subdomains with the convergence factor

$$\kappa = \frac{e^{\sqrt{c}L/N} + e^{\sqrt{c}\delta}}{e^{\sqrt{c}(L/N+\delta)} + 1},$$

where L is the manifold length, and δ is the overlap.

Proof. For the overlapping equal-sized partitioning in Definition 3.1.2 with $0 < \delta < L/N$, we have

$$p_1 = p_2 = \cdots = p_N = q_1 = q_2 = \cdots = q_N,$$
$$r_1 = r_2 = \cdots = r_N = s_1 = s_2 = \cdots = s_N.$$

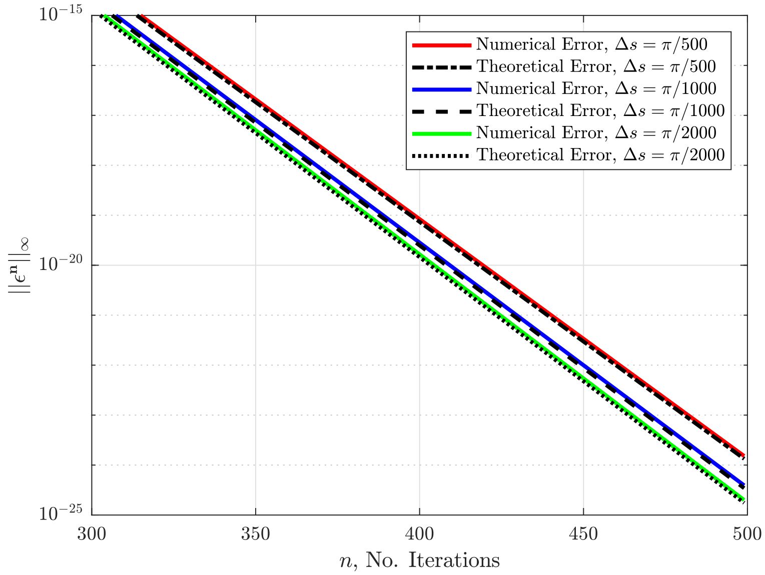

Figure 3.4: Error decay for (3.5) with $c = 1$ and three different mesh sizes on the unit circle shown in Figure 3.1.

Define $p = p_j$ and $r = r_j$ for $j = 1, \ldots, N$. Thus, the iteration matrix becomes

$$\mathbf{M}_{\text{CPS}} = \begin{bmatrix}
0 & 0 & r & & & & & & & & & & p \\
0 & 0 & p & & & & & & & & & & r \\
 & p & 0 & 0 & r & & & & & & & & \\
 & r & 0 & 0 & p & & & & & & & & \\
 & & & p & 0 & 0 & r & & & & & & \\
 & & & r & 0 & 0 & p & & & & & & \\
 & & & & & \ddots & \ddots & \ddots & \ddots & & & & \\
 & & & & & & \ddots & \ddots & \ddots & \ddots & & & \\
 & & & & & & & & p & 0 & 0 & r & \\
 & & & & & & & & r & 0 & 0 & p & \\
r & & & & & & & & & & p & 0 & 0 \\
p & & & & & & & & & & r & 0 & 0
\end{bmatrix}. \tag{3.12}$$

The convergence is a direct consequence of Theorem 3.1.3, but we provide the convergence factor in terms of manifold length L, number of subdomains N, and overlap parameter δ. The iteration matrix is non-negative, i.e, all entries of the matrix are non-negative. The Perron-Frobenius theorem states that the maximal eigenvalue in modulus of a non-negative irreducible matrix is bounded by the minimum and maximum of the row sums [6]:

$$\min_{1 \le i \le 2N} \sigma_i \le \rho(\mathbf{M}_{\text{CPS}}) \le \max_{1 \le i \le 2N} \sigma_i,$$

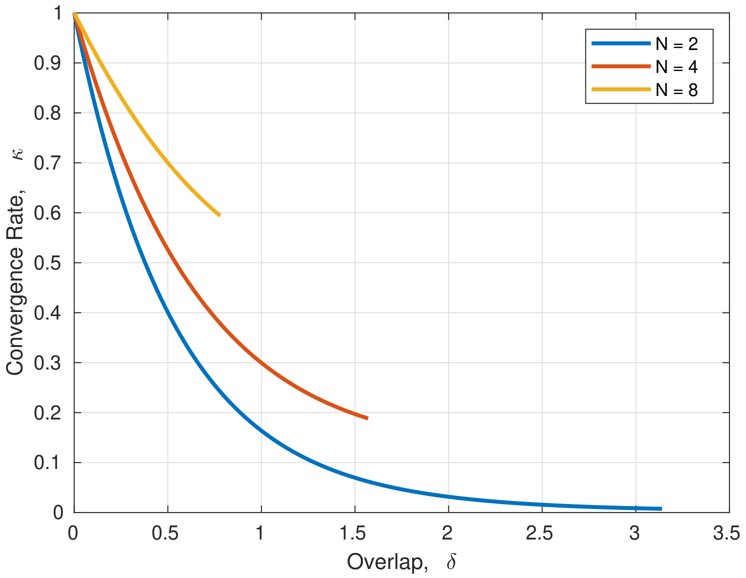

Figure 3.5: The CPS convergence factor obtained in Corollary 3.1.1 for equal-sized partitioning of the unit circle.

where σ_i denotes the sum of entries in row i. Non-negativity of the iteration matrix (3.11) is trivial. To show that it is irreducible, consider a directed graph with $2N$ vertices for the matrix in which there is an edge from vertex i to vertex j when $\mathbf{M}_{\text{CPS}ij} > 0$. Then, the matrix $\mathbf{M}_{\text{CPS}}$ is irreducible if and only if the graph is strongly connected, i.e., every vertex is reachable from every other vertex. The maximum and minimum row sums are equal since $\sigma_1 = \cdots = \sigma_N = p + r$. Thus,

$$\kappa = \rho(\mathbf{M}_{\text{CPS}}) = ||\mathbf{M}_{\text{CPS}}||_\infty = p + r = \frac{e^{\sqrt{c}L/N} + e^{\sqrt{c}\delta}}{e^{\sqrt{c}(L/N+\delta)} + 1},$$

which proves the corollary. □

Figure 3.5 shows the convergence factor for the unit circle ($L = 2\pi$) with different numbers of subdomains plotted against the overlap parameter. By increasing the number of subdomains, it is more difficult to reach convergence. Moreover, increasing the amount of overlap exponentially improves the convergence with an added computational load. The result obtained in Corollary 3.1.1 can be interpreted differently. The convergence factor depends on the overlap parameter δ and the length of disjoint subdomains L/N. That is, the unit circle partitioned with four subdomains has the same convergence factor as a circle with radius 2 which is partitioned with eight subdomains.

We finish this section by pointing out the fact that the CPS is an overlapping domain decomposition method. For an equal-sized partitioning without overlap, the convergence factor is equal to one as we can see in Figure 3.5. We now prove this for a set of arbitrary non-overlapping subdomains in the following corollary.

Corollary 3.1.2. For a non-overlapping partitioning of a 1-manifold based on Definition 3.1.1, the CPS iterations (3.5) for the positive Helmholtz equation on a closed surface does not converge to zero.

Proof. For non-overlapping subdomains, that is $\delta_j = 0$, we obtain $p_j = q_j = 1$ and $r_j = s_j = 0$ by a direct substitution in Equation (3.9). Thus, the iteration matrix becomes

$$\mathbf{M}_{\text{CPS}} = \begin{bmatrix} 0 & 0 & 0 & & & & & & & & & & 1 \\ 0 & 0 & 1 & & & & & & & & & & 0 \\ & 1 & 0 & 0 & 0 & & & & & & & & \\ & 0 & 0 & 0 & 1 & & & & & & & & \\ & & & 1 & 0 & 0 & 0 & & & & & & \\ & & & 0 & 0 & 0 & 1 & & & & & & \\ & & & & & \ddots & \ddots & \ddots & \ddots & & & & \\ & & & & & & \ddots & \ddots & \ddots & \ddots & & & \\ & & & & & & & & 1 & 0 & 0 & 0 & \\ & & & & & & & & 0 & 0 & 0 & 1 & \\ 0 & & & & & & & & & & 1 & 0 & 0 \\ 1 & & & & & & & & & & 0 & 0 & 0 \end{bmatrix}. \tag{3.13}$$

The matrix in (3.13) is a doubly stochastic matrix with row and column sums of one and is known to have spectral radius of one. To see this, the Greshgorin circle theorem [28] shows that the eigenvalues of the matrix are within the unit circle, providing $\lambda \leq 1$. Now, we show that one is an eigenvalue of the stochastic matrix. Suppose $\mathbf{v}$ is the all-ones vector of dimension $2N$. Trivially, one can find $\mathbf{M}_{\text{CPS}}\mathbf{v} = 1 \cdot \mathbf{v}$. Hence, it follows that one is an eigenvalue. Hence,

$$\rho(\mathbf{M}_{\text{PCS}}) = 1,$$

and the algorithm stagnates and does not converge to the zero solution. □

3.1.2 The CAS-CPM

Using Theorem 3.1.1 and the partitioning detailed in Definition 3.1.1, the CAS-CPM for a closed 1-manifold at the continuous level is equivalent to:

$$\begin{cases} (c - \dfrac{\mathrm{d}^2}{\mathrm{d}s^2})\epsilon_j^{n+1} = 0, \qquad \text{for } s \in [a_j, b_j], \\ \epsilon_j^{n+1}(a_j) = \epsilon_{j-1}^{n+1}(a_j), \\ \epsilon_j^{n+1}(b_j) = \epsilon_{j+1}^{n}(b_j), \end{cases} \tag{3.14}$$

which has the solution

$$\epsilon_j^{n+1}(s) = \frac{e^{\sqrt{c}(s-a_j)} - e^{\sqrt{c}(b_j-s+\ell_j)}}{1-e^{2\sqrt{c}\ell_j}}\epsilon_{j-1}^{n+1}(a_j) + \frac{e^{\sqrt{c}(b_j-s)} - e^{\sqrt{c}(s-a_j+\ell_j)}}{1-e^{2\sqrt{c}\ell_j}}\epsilon_{j+1}^{n}(b_j), \tag{3.15}$$

for $j = 1, \ldots, N$. Note that (3.4) still applies to Equation (3.15).

One can evaluate the errors at the boundaries using the solution provided in Equation (3.15) in terms of the error values at the boundaries:

$$\begin{cases} \epsilon_j^{n+1}(b_{j-1}) = p_j\epsilon_{j-1}^{n+1}(a_j) + r_j\epsilon_{j+1}^{n}(b_j), \\ \epsilon_j^{n+1}(a_{j+1}) = s_j\epsilon_{j-1}^{n+1}(a_j) + q_j\epsilon_{j+1}^{n}(b_j), \end{cases} \tag{3.16}$$

where p_j, r_j, s_j, and q_j are quantities defined in (3.9). We wish to replace the terms containing $\epsilon_{j-1}^{n+1}(a_j)$ with an expression involving values from the previous iteration. By working from the first subdomain to the j^{th} subdomain in the second part (3.16), we can write $\epsilon_{j-1}^{n+1}(a_j)$ as

$$\begin{aligned} \epsilon_{j-1}^{n+1}(a_j) = s_{j-1}s_{j-2}\ldots s_2q_1\epsilon_2^n(b_1) + s_{j-1}s_{j-2}\ldots s_3q_2\epsilon_3^n(b_2) + \ldots \\ + q_{j-1}\epsilon_j^n(b_{j-1}) + s_{j-1}s_{j-2}\ldots s_1\epsilon_N^n(a_1+L). \end{aligned} \tag{3.17}$$

Substituting (3.17) back into Equation (3.16), we obtain

$$\begin{cases} \epsilon_j^{n+1}(b_{j-1}) &= p_j\Big[s_{j-1}s_{j-2}\ldots s_2q_1\epsilon_2^n(b_1) + s_{j-1}s_{j-2}\ldots s_3q_2\epsilon_3^n(b_2) + \ldots \\ &\qquad +q_{j-1}\epsilon_j^n(b_{j-1}) + s_{j-1}s_{j-2}\ldots s_1\epsilon_N^n(a_1+L)\Big] + r_j\epsilon_{j+1}^n(b_j), \\ \epsilon_j^{n+1}(a_{j+1}) &= s_j\Big[s_{j-1}s_{j-2}\ldots s_2q_1\epsilon_2^n(b_1) + s_{j-1}s_{j-2}\ldots s_3q_2\epsilon_3^n(b_2) + \ldots \\ &\qquad +q_{j-1}\epsilon_j^n(b_{j-1}) + s_{j-1}s_{j-2}\ldots s_1\epsilon_N^n(a_1+L)\Big] + q_j\epsilon_{j+1}^n(b_j). \end{cases} \tag{3.18}$$

Now that the error expressions at the interfaces only depend on $\epsilon_j^n(b_{j-1})$, we define an error vector at iteration n which is comprised solely of the error values at the endpoints b_{j-1}:

$$\boldsymbol{\epsilon}^n = [\epsilon_2^n(b_1), \epsilon_3^n(b_2), \ldots, \epsilon_N^n(b_{N-1}), \epsilon_N^n(a_1 + L)]^T. \tag{3.19}$$

Next, we recast this in matrix form using the quantities defined in (3.9),

$$\boldsymbol{\epsilon}^{n+1} = \mathbf{M}_{\text{CAS}} \boldsymbol{\epsilon}^n, \tag{3.20}$$

where $\mathbf{M}_{\text{CAS}}$ is referred to as the iteration matrix. It has dimension of $N \times N$ for the classical alternating Schwarz method, and is given by

$$\mathbf{M}_{\mathrm{CAS}} = \begin{bmatrix} p_2q_1 & r_2 & & & & & p_2s_1 \\ p_3s_2q_1 & p_3q_2 & r_3 & & & & p_3s_2s_1 \\ p_4s_3s_2q_1 & p_4s_3q_2 & p_4q_3 & r_4 & & & p_4s_3s_2s_1 \\ \vdots & & & \ddots & \ddots & & \vdots \\ p_{N-1}s_{N-2}\cdots s_2q_1 & p_{N-1}s_{N-2}\cdots s_3q_2 & \cdots & & p_{N-1}q_{N-2} & r_{N-1} & p_{N-1}s_{N-2}\cdots s_1 \\ r_Nr_1 + p_Ns_{N-1}\cdots s_2q_1 & p_Ns_{N-1}\cdots s_3q_2 & \cdots & & p_Ns_{N-1}q_{N-2} & p_Nq_{N-1} & r_Np_1 + p_Ns_{N-1}\cdots s_1 \\ q_Nr_1 + s_Ns_{N-1}\cdots s_2q_1 & s_Ns_{N-1}\cdots s_3q_2 & \cdots & & s_Ns_{N-1}q_{N-2} & s_Nq_{N-1} & q_Np_1 + s_Ns_{N-1}\cdots s_1 \end{bmatrix}. \qquad (3.21)$$

Theorem 3.1.4. Under the restrictions on the partitioning of the 1-manifold $\mathcal{S}$ detailed in Definition 3.1.1 with $\delta_j \neq 0$ for $j = 1, \dots, N$, the CAS iterations (3.14), with $N \geq 2$, for the positive Helmholtz equation on any closed 1-manifold converges globally on an arbitrary number of subdomains.

Proof. Following the discussion in Theorem 3.1.3, the convergence can be concluded if we show $||\mathbf{M}_{\text{CAS}}||_\infty < 1$. The max-norm is equal to the maximum of the absolute row sums:

$$||\mathbf{M}_{\text{CAS}}||_\infty = \max\{\sigma_1, \sigma_2, \dots, \sigma_{N-1}, \sigma_N\},$$

where σ_j is the absolute sum of entities in the j^{th} row. Considering the fact that the quantities are all non-negative, the absolute row sums for $1 \leq j \leq N-2$ are

$$\sigma_j = p_{j+1}s_j \dots s_2 q_1 + p_{j+1}s_j \dots s_3 q_2 + \dots + p_{j+1}q_j + r_{j+1} + p_{j+1}s_j \dots s_1,$$

which can be expressed using the nested product:

$$\sigma_j = p_{j+1}(s_j(s_{j-1}(\dots(s_2(s_1 + q_1) + q_2) + \dots) + q_{j-1}) + q_j) + r_{j+1}.$$

Starting at the innermost bracket in the first term, we have $s_1 + q_1 < 1$ from Lemma 3.1.2. The next bracket is $s_2(s_1 + q_1) + q_2 < s_2 + q_2 < 1$. Moving to the next set of brackets, we have $s_3(s_2(s_1 + q_1) + q_2) + q_3 < s_3 + q_3 < 1$. Proceeding in this manner, we know that each term contained within brackets will be less than one in magnitude, and as such we have:

$$\begin{aligned}\sigma_j &= p_{j+1}(s_j(s_{j-1}(\dots(s_2(s_1 + q_1) + q_2) + \dots) + q_{j-1}) + q_j) + r_{j+1},\\ &< p_{j+1}(s_j(s_{j-1}(\dots(s_2 + q_2) + \dots) + q_{j-1}) + q_j) + r_{j+1},\\ &\vdots\\ &< p_{j+1} + r_{j+1},\\ &< 1.\end{aligned}$$

Similarly, for the last two rows,

$$\begin{aligned}\sigma_{N-1} &= r_N r_1 + p_N s_{N-1} \dots s_2 q_1 + p_N s_{N-1} \dots s_3 q_2 + \dots + p_N s_{N-1} q_{N-2} + p_N q_{N-1}\\ &\qquad + r_N p_1 + p_N s_{N-1} \dots s_1,\\ &= p_N(s_{N-1}(s_{N-2}(\dots(s_2(s_1 + q_1) + q_2) + \dots) + q_{N-2}) + q_{N-1}) + r_N(p_1 + r_1),\\ &< p_N(s_{N-1}(s_{N-2}(\dots(s_2 + q_2) + \dots) + q_{N-2}) + q_{N-1}) + r_N(p_1 + r_1),\\ &\vdots\\ &< p_N + r_N,\\ &< 1,\end{aligned}$$

and

$$\begin{aligned}\sigma_N &= q_N r_1 + s_N s_{N-1} \dots s_2 q_1 + s_N s_{N-1} \dots s_3 q_2 + \cdots + s_N s_{N-1} q_{N-2} + s_N q_{N-1}, \\ &\qquad\qquad\qquad\qquad\qquad\qquad\qquad\qquad\qquad\qquad + q_N p_1 + s_N s_{N-1} \dots s_1, \\ &= s_N(s_{N-1}(s_{N-2}(\dots(s_2(s_1+q_1)+q_2)+\dots)+q_{N-2})+q_{N-1})+q_N(p_1+r_1), \\ &< s_N(s_{N-1}(s_{N-2}(\dots(s_2+q_2)+\dots)+q_{N-2})+q_{N-1})+q_N(p_1+r_1), \\ &\vdots \\ &< s_N + q_N, \\ &< 1.\end{aligned}$$

Now that the absolute row sums have been shown to be less than one, we have

$$\rho(\mathbf{M}_{\text{CAS}}) \leq ||\mathbf{M}_{\text{CAS}}||_\infty < 1.$$

Hence, the algorithm converges for any finite number of overlapping subdomains. □

We now investigate the sharpness of the theorem above. The CAS method (3.14) is implemented in MATLAB for the unit square. We will also use this example to verify the fact that the smoothness of the manifold is not a necessary condition for the convergence as the curve is parameterized along the curve length. Figure 3.6 depicts the unit square partitioned with four subdomains with different overlaps. Having $c = 1$ and the initial guess $u(s) = 1$, the solution at several iterations with the resolution $\Delta s = 0.001$ is shown in Figure 3.7. According to the figure, the last subdomain (the shortest in length) is disruptive to the convergence. Finally, Figure 3.3 illustrates the max-norm of the error vector (3.18) over different iterations along with the theoretical error $[\rho(\mathbf{M}_{\text{CAS}})]^n||\boldsymbol{\epsilon}^{\mathbf{0}}||_\infty$ and the upper bound found in Theorem 3.1.4, $||\mathbf{M}_{\text{CAS}}||_\infty^n||\boldsymbol{\epsilon}^{\mathbf{0}}||_\infty$. The Figure 3.8 validates our analysis in Theorem 3.1.4 for the CAS method.

Corollary 3.1.3. For an equal-sized overlapping partitioning of a closed 1-manifold $\mathcal{S}$ based on Definition 3.1.2, the CAS iterations (3.14) with $N \geq 3$ for the positive Helmholtz equation on $\mathcal{S}$ converge with κ bounded as:

$$\kappa \leq p^2 + pr + r,$$

and for $N = 2$:

$$\kappa = p^2 + 2pr + r^2.$$

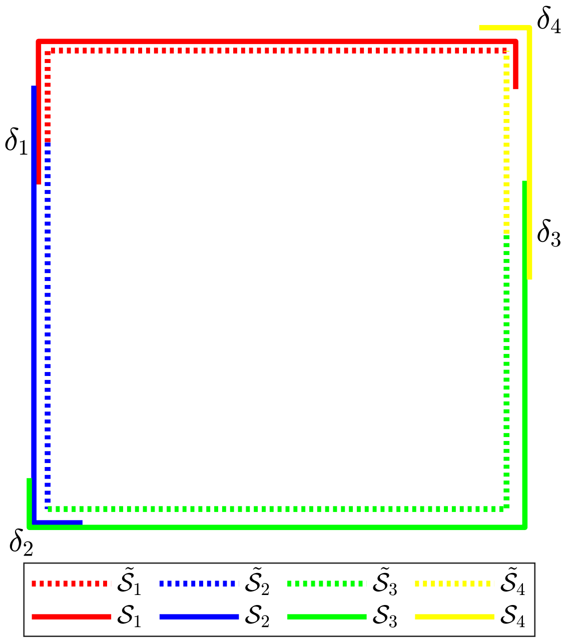

Figure 3.6: The unit square with four overlapping subdomains.

Proof. The convergence can be concluded from Theorem 3.1.4. For an equal-sized partitioning, we have

$$\begin{aligned} p_1 = p_2 = \cdots = p_N = q_1 = q_2 = \cdots = q_N, \\ r_1 = r_2 = \cdots = r_N = s_1 = s_2 = \cdots = s_N. \end{aligned}$$

We set $p = p_j$ and $r = r_j$ for $j = 1, \ldots, N$. Thus, the iteration matrix becomes:

$$\mathbf{M}_{\text{CAS}} = \begin{bmatrix} p^2 & r & & & & & pr \\ p^2 r & p^2 & r & & & & pr^2 \\ p^2 r^2 & p^2 r & p^2 & r & & & pr^3 \\ \vdots & & & \ddots & \ddots & & \vdots \\ p^2 r^{N-3} & p^2 r^{N-4} & \cdots & & p^2 & r & pr^{N-2} \\ r^2 + p^2 r^{N-2} & p^2 r^{N-3} & \cdots & & p^2 r & p^2 & pr + pr^{N-1} \\ pr + pr^{N-1} & pr^{N-2} & \cdots & & pr^2 & r^2 & p^2 + r^N \end{bmatrix}.$$

The spectral radius is bounded by the max-norm of the iteration matrix, and the max-norm is the maximal absolute row sum. Suppose j is any row index from $2, \ldots, N-2$. Since the

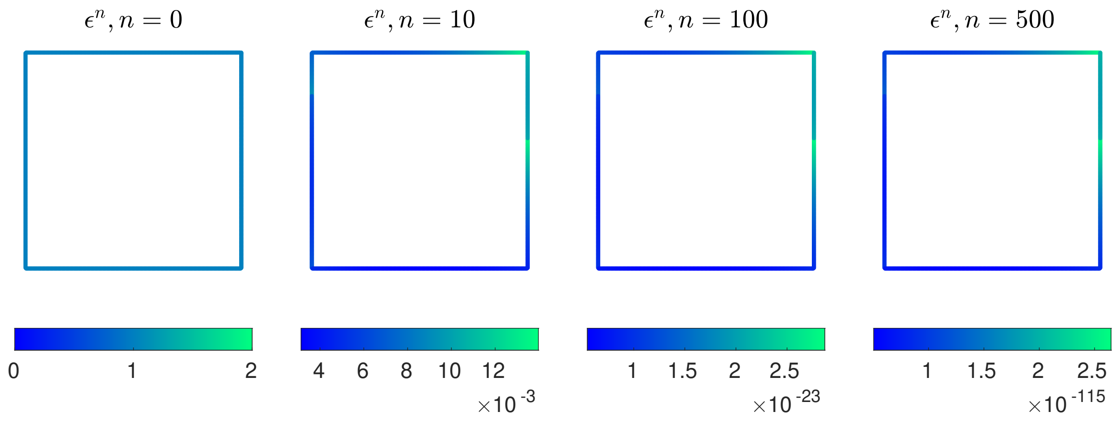

Figure 3.7: Global solution to (3.14) on the unit square at different iterations with $c = 1$.

only differences between the rows $j-1$ and j are the entries in the first and last columns, we write

$$\sigma_j - \sigma_{j-1} = \left[p^2 r^{j-1} + pr^j\right] - \left[pr^{j-1}\right] = pr^{j-1}\left(p + r - 1\right) < 0,$$

because $p+r < 1$. Hence, $\sigma_j < \sigma_{j-1}$ for the rows 2 to $N-2$. Similarly by comparing σ_{N-2} and σ_{N-1}, one observes that $\sigma_{N-1} < \sigma_{N-2}$. Hence, we obtain $\sigma_{N-1} < \sigma_{N-2} < \cdots < \sigma_2 < \sigma_1$. We only need to compare σ_1 and σ_N to find the maximum row sum:

$$\begin{aligned}\sigma_N &= r(r(r(\ldots(r(r+p)+p)+\ldots)+p)+p)+pr+p^2,\\ &< r + pr + p^2,\\ &= \sigma_1.\end{aligned}$$

Hence,

$$\kappa \leq ||\mathbf{M}_{\text{CAS}}||_\infty = p^2 + pr + r.$$

For the two-subdomain case, we can theoretically derive the convergence factor. In this case, the iteration matrix reduces to

$$\mathbf{M}_{\text{CAS}} = \begin{bmatrix} r^2 + p^2 & 2pr \\ 2pr & p^2 + r^2 \end{bmatrix},$$

where its spectral radius is $\kappa = ||\mathbf{M}_{\text{CAS}}||_\infty = p^2 + 2pr + r^2$. □

Unfortunately, we are not able to derive an analytical convergence factor for the equal-sized partitioning with any number of subdomains. However, Corollary 3.1.3 gives us an insight into the convergence factor by providing an upper bound. Figure 3.9 illustrates the convergence factor of the CAS method on the square with side length two ($L = 8$) partitioned equally into two, four, and eight subdomains. While the spectral radii are shown for each case by explicitly constructing the iteration matrix, they are bounded by the max-

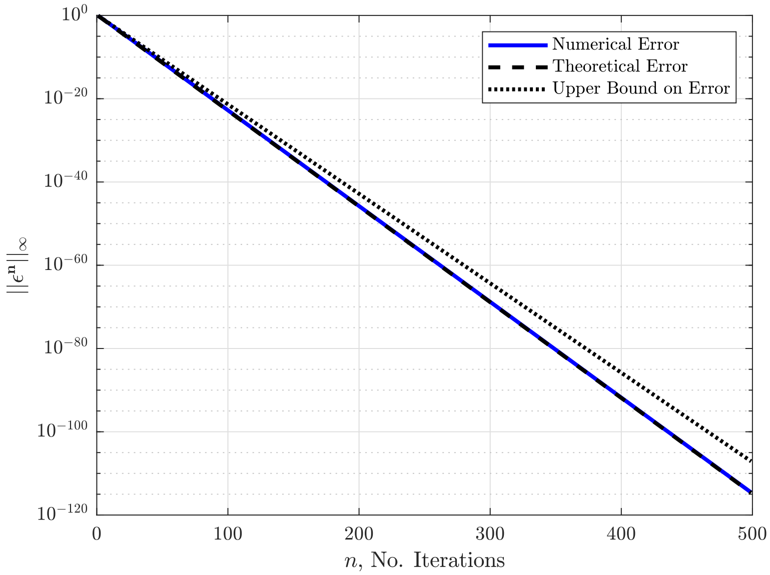

Figure 3.8: Error decay for (3.14) with $c = 1$ on the unit square shown in Figure 3.6.

norm of the matrix. The obtained upper bound is quite close to the convergence factor when the overlap is small (approximately less than $0.25\delta_{\max}$), while the spectral radius diverges from the max-norm for larger overlaps. Notice that the convergence of the method is improved when we increase the overlap. This is expected in domain decomposition methods as the iterations on larger subdomains better mimic the original problem.

Similar to the CPS method, the CAS method (3.14) is only convergent to the zero solution for an overlapping partitioning. This is proved in the following corollary.

Corollary 3.1.4. For a non-overlapping partitioning of a closed 1-manifold provided in Definition 3.1.1, the CAS algorithm in (3.5) for the positive Helmholtz equation does not converge.

Proof. In Corollary 3.1.2, we indicated that $p_j = q_j = 1$ and $r_j = s_j = 0$ for a non-overlapping set of subdomains. Thus, the iteration matrix becomes

$$\mathbf{M}_{\text{CAS}} = \begin{bmatrix} 1 & & & & & & \\ & 1 & & & & & \\ & & 1 & & & & \\ & & & \ddots & & & \\ & & & & 1 & & \\ & & & & & 1 & \\ & & & & & & 1 \end{bmatrix}.$$

Consequently, $\rho(\mathbf{M}_{\text{CAS}}) = 1$, and the algorithm does not converge to the desired zero solution unless the initial guess is zero. □

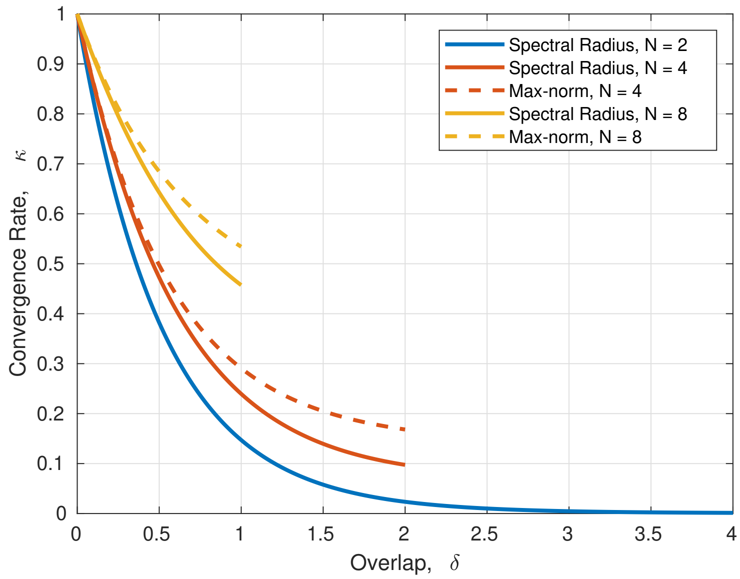

Figure 3.9: Convergence factor of the CAS method versus the overlap in an equal-sized partitioning configuration.

As we have seen, the classical Schwarz methods only converge on subdomains with overlap. This is the reason that the classical Schwarz algorithms are called overlapping domain decomposition methods, while the optimized Schwarz methods are also convergent without overlap. We will explore two optimized Schwarz methods in the following sections.

3.1.3 The OPS-CPM

Assume $\mathcal{B} = \partial/\partial\hat{n} + \alpha$ is the Robin boundary operator where $\hat{n}$ represents the outward normal to the interface and $\alpha \geq 0$. Since we solve a one dimensional differential equation along the curve length s, the boundary operator is either $\mathcal{B}^+ := \mathrm{d}/\,\mathrm{d}s + \alpha$ or $\mathcal{B}^- := -\,\mathrm{d}/\,\mathrm{d}s + \alpha$. Hence, the equivalent Schwarz method to the OPS-CPM at the continuous level is:

$$\begin{cases} \left(c - \dfrac{\mathrm{d}^2}{\mathrm{d}s^2}\right)\epsilon_j^{n+1} = 0, & \text{for } s \in [a_j, b_j], \\ \left(\alpha - \dfrac{\mathrm{d}}{\mathrm{d}s}\right)\epsilon_j^{n+1}(a_j) = \left(\alpha - \dfrac{\mathrm{d}}{\mathrm{d}s}\right)\epsilon_{j-1}^{n}(a_j), \\ \left(\alpha + \dfrac{\mathrm{d}}{\mathrm{d}s}\right)\epsilon_j^{n+1}(b_j) = \left(\alpha + \dfrac{\mathrm{d}}{\mathrm{d}s}\right)\epsilon_{j+1}^{n}(b_j). \end{cases} \tag{3.22}$$

The solution can be found in the form of:

$$\epsilon_j^{n+1}(s) = \frac{e^{\sqrt{c}(s-a_j)} - e^{\sqrt{c}(b_j-s+\ell_j)}}{1-e^{2\sqrt{c}\ell_j}}\mathcal{B}^-\epsilon_{j-1}^{n}(a_j) + \frac{e^{\sqrt{c}(b_j-s)} - e^{\sqrt{c}(s-a_j+\ell_j)}}{1-e^{2\sqrt{c}\ell_j}}\mathcal{B}^+\epsilon_{j+1}^{n}(b_j), \tag{3.23}$$

for $j = 1, \ldots, N$, with (3.4) defining $\epsilon_0^n(a_1)$ and $\epsilon_{N+1}^n(b_N)$.

We have to evaluate the errors at the boundaries in terms of the error values at the boundaries in the previous iteration. Using Equation (3.23), we obtain

$$\begin{cases} \epsilon_j^{n+1}(b_{j-1}) = p_j\mathcal{B}^-\epsilon_{j-1}^{n}(a_j) + r_j\mathcal{B}^+\epsilon_{j+1}^{n}(b_j), \\ \epsilon_j^{n+1}(a_{j+1}) = s_j\mathcal{B}^-\epsilon_{j-1}^{n}(a_j) + q_j\mathcal{B}^+\epsilon_{j+1}^{n}(b_j), \end{cases} \tag{3.24}$$

where for $1 \leq j \leq N$,

$$\begin{aligned} p_j &= \frac{(\alpha-1)-(\alpha+1)e^{2\sqrt{c}(\ell_j-\delta_{j-1})}}{(\alpha-1)^2-(\alpha+1)^2e^{2\sqrt{c}\ell_j}}e^{\sqrt{c}\delta_{j-1}}, \quad & r_j &= \frac{(\alpha-1)-(\alpha+1)e^{2\sqrt{c}\delta_{j-1}}}{(\alpha-1)^2-(\alpha+1)^2e^{2\sqrt{c}\ell_j}}e^{\sqrt{c}(\ell_j-\delta_{j-1})} \\ q_j &= \frac{(\alpha-1)-(\alpha+1)e^{2\sqrt{c}(\ell_j-\delta_j)}}{(\alpha-1)^2-(\alpha+1)^2e^{2\sqrt{c}\ell_j}}e^{\sqrt{c}\delta_j}, & s_j &= \frac{(\alpha-1)-(\alpha+1)e^{2\sqrt{c}\delta_j}}{(\alpha-1)^2-(\alpha+1)^2e^{2\sqrt{c}\ell_j}}e^{\sqrt{c}(\ell_j-\delta_j)}. \end{aligned} \tag{3.25}$$

We wish to have the right-hand-side of Equation (3.24) solely in terms of the error values. By applying the boundary operator to Equation (3.23), one arrives at

$$\begin{cases} \mathcal{B}^+\epsilon_j^{n+1}(b_{j-1}) = p_j^\dagger\mathcal{B}^-\epsilon_{j-1}^{n}(a_j) + r_j^\dagger\mathcal{B}^+\epsilon_{j+1}^{n}(b_j), \\ \mathcal{B}^-\epsilon_j^{n+1}(a_{j+1}) = s_j^\dagger\mathcal{B}^-\epsilon_{j-1}^{n}(a_j) + q_j^\dagger\mathcal{B}^+\epsilon_{j+1}^{n}(b_j), \end{cases} \tag{3.26}$$

where

$$p_j^\dagger = \frac{(\alpha^2-1)-(\alpha^2-1)e^{2\sqrt{c}(\ell_j-\delta_{j-1})}}{(\alpha-1)^2-(\alpha+1)^2e^{2\sqrt{c}\ell_j}}e^{\sqrt{c}\delta_{j-1}}, \quad r_j^\dagger = \frac{(\alpha-1)^2-(\alpha+1)^2e^{2\sqrt{c}\delta_{j-1}}}{(\alpha-1)^2-(\alpha+1)^2e^{2\sqrt{c}\ell_j}}e^{\sqrt{c}(\ell_j-\delta_{j-1})},$$

$$q_j^\dagger = \frac{(\alpha^2-1)-(\alpha^2-1)e^{2\sqrt{c}(\ell_j-\delta_j)}}{(\alpha-1)^2-(\alpha+1)^2e^{2\sqrt{c}\ell_j}}e^{\sqrt{c}\delta_j}, \qquad s_j^\dagger = \frac{(\alpha-1)^2-(\alpha+1)^2e^{2\sqrt{c}\delta_j}}{(\alpha-1)^2-(\alpha+1)^2e^{2\sqrt{c}\ell_j}}e^{\sqrt{c}(\ell_j-\delta_j)}. \tag{3.27}$$

Now, we define an error vector for iteration n which includes the error values at the interfaces:

$$\boldsymbol{\epsilon}^n := [\epsilon_1^n(b_N-L), \epsilon_1^n(a_2), \epsilon_2^n(b_1), \epsilon_2^n(a_3), \ldots, \epsilon_N^n(b_{N-1}), \epsilon_N^n(a_1+L)]^T.$$

We also collect $\mathcal{B}\epsilon_j^n$ at the interfaces (these quantities appear in the error solutions) in another vector:

$$\boldsymbol{\mathcal{B}\epsilon}^n := [\mathcal{B}^+\epsilon_1^n(b_S-L), \mathcal{B}^-\epsilon_1^n(a_2), \mathcal{B}^+\epsilon_2^n(b_1), \ldots, \mathcal{B}^+\epsilon_N^n(b_{N-1}), \mathcal{B}^-\epsilon_N^n(a_1+L)]^T.$$

By recasting the error values at the interfaces in Equation (3.24) in matrix form,

$$\boldsymbol{\epsilon}^{n+1} = \mathbf{M}\boldsymbol{\mathcal{B}\epsilon}^n, \tag{3.28}$$

and similarly Equation (3.26) in matrix form is

$$\boldsymbol{\mathcal{B}\epsilon}^n = \mathrm{M}^\dagger\boldsymbol{\mathcal{B}\epsilon}^{n-1}, \tag{3.29}$$

where $\mathbf{M}$ and $\mathbf{M}^{\dagger}$ are $2N \times 2N$ matrices defined as follows:

$$\mathbf{M} = \begin{bmatrix} 0 & 0 & r_1 & & & & & & & & & & p_1 \\ 0 & 0 & q_1 & & & & & & & & & & s_1 \\ & p_2 & 0 & 0 & r_2 & & & & & & & & \\ & s_2 & 0 & 0 & q_2 & & & & & & & & \\ & & & p_3 & 0 & 0 & r_3 & & & & & & \\ & & & s_3 & 0 & 0 & q_3 & & & & & & \\ & & & & & \ddots & \ddots & \ddots & \ddots & & & & \\ & & & & & & \ddots & \ddots & \ddots & \ddots & & & \\ & & & & & & & & p_{N-1} & 0 & 0 & r_{N-1} & \\ & & & & & & & & s_{N-1} & 0 & 0 & q_{N-1} & \\ r_N & & & & & & & & & & p_N & 0 & 0 \\ q_N & & & & & & & & & & s_N & 0 & 0 \end{bmatrix}, \tag{3.30}$$

$$\mathbf{M}^{\dagger} = \begin{bmatrix} 0 & 0 & r_1^{\dagger} & & & & & & & & & & p_1^{\dagger} \\ 0 & 0 & q_1^{\dagger} & & & & & & & & & & s_1^{\dagger} \\ & p_2^{\dagger} & 0 & 0 & r_2^{\dagger} & & & & & & & & \\ & s_2^{\dagger} & 0 & 0 & q_2^{\dagger} & & & & & & & & \\ & & & p_3^{\dagger} & 0 & 0 & r_3^{\dagger} & & & & & & \\ & & & s_3^{\dagger} & 0 & 0 & q_3^{\dagger} & & & & & & \\ & & & & & \ddots & \ddots & \ddots & \ddots & & & & \\ & & & & & & \ddots & \ddots & \ddots & \ddots & & & \\ & & & & & & & & p_{N-1}^{\dagger} & 0 & 0 & r_{N-1}^{\dagger} & \\ & & & & & & & & s_{N-1}^{\dagger} & 0 & 0 & q_{N-1}^{\dagger} & \\ r_N^{\dagger} & & & & & & & & & & p_N^{\dagger} & 0 & 0 \\ q_N^{\dagger} & & & & & & & & & & s_N^{\dagger} & 0 & 0 \end{bmatrix}. \tag{3.31}$$

Equation (3.28) and Equation (3.29) together result in:

$$\boldsymbol{\epsilon}^{n+1} = \mathbf{M}_{\mathrm{OPS}} \boldsymbol{\epsilon}^{n} \tag{3.32}$$

where $\mathbf{M}_{\mathrm{OPS}} = \mathbf{M}\mathbf{M}^{\dagger}\mathbf{M}^{-1}$.

Before proving the general convergence of the method, we need to state the following lemma for the quantities in (3.27). Notice that the partitioning used in the lemma is not necessarily overlapping.

Lemma 3.1.5. Consider the partitioning specified in Definition 3.1.1. The quantities introduced in (3.27) satisfy

$$\begin{aligned} |p_j^\dagger| + |r_j^\dagger| &< 1, \\ |q_j^\dagger| + |s_j^\dagger| &< 1, \end{aligned}$$

for all $\alpha \geq 0$.

Proof. Due to the restrictions on the overlap and length parameters, all exponential terms are greater than one. All four quantities have the same denominator which is always negative for non-negative α since $(\alpha - 1)^2 < (\alpha + 1)^2$ and $e^{2\ell_j} > 1$ for all subdomains. The same logic applies to the numerator of $r_j^\dagger$ and $s_j^\dagger$, resulting in $r_j^\dagger > 0$ and $s_j^\dagger > 0$. By factoring out $(\alpha^2 - 1)$ from the numerator of $p_j^\dagger$, we obtain

$$p_j^\dagger = (\alpha^2 - 1) \cdot \frac{1 - e^{2\sqrt{c}(\ell_j - \delta_{j-1})}}{(\alpha - 1)^2 - (\alpha + 1)^2 e^{2\sqrt{c}\ell_j}} e^{\sqrt{c}\delta_{j-1}},$$

that is positive for $\alpha > 1$ and negative for $0 < \alpha < 1$. We have to explore these two cases separately. Starting with $\alpha \geq 1$:

$$
\begin{aligned}
|p_j^\dagger| + |r_j^\dagger| &= p_j^\dagger + r_j^\dagger, \\
&= \frac{(\alpha^2-1)e^{\sqrt{c}\delta_{j-1}} - (\alpha^2-1)e^{\sqrt{c}(2\ell_j-\delta_{j-1})}}{(\alpha-1)^2 - (\alpha+1)^2 e^{2\sqrt{c}\ell_j}} \\
&\qquad\qquad\qquad + \frac{(\alpha-1)^2 e^{\sqrt{c}(\ell_j-\delta_{j-1})} - (\alpha+1)^2 e^{\sqrt{c}(\ell_j+\delta_{j-1})}}{(\alpha-1)^2 - (\alpha+1)^2 e^{2\sqrt{c}\ell_j}}, \\
&= \frac{(\alpha+1)e^{\sqrt{c}\delta_{j-1}}\big[(\alpha-1) - (\alpha+1)e^{\sqrt{c}\ell_j}\big]}{(\alpha-1)^2 - (\alpha+1)^2 e^{2\sqrt{c}\ell_j}}, \\
&\qquad\qquad\qquad + \frac{(\alpha-1)e^{\sqrt{c}(\ell_j-\delta_{j-1})}\big[(\alpha-1) - (\alpha+1)e^{\sqrt{c}\ell_j}\big]}{(\alpha-1)^2 - (\alpha+1)^2 e^{2\sqrt{c}\ell_j}}, \\
&= \frac{\big[(\alpha-1)e^{\sqrt{c}(\ell_j-\delta_{j-1})} + (\alpha+1)e^{\sqrt{c}\delta_{j-1}}\big]\big[(\alpha-1) - (\alpha+1)e^{\sqrt{c}\ell_j}\big]}{(\alpha-1)^2 - (\alpha+1)^2 e^{2\sqrt{c}\ell_j}}, \\
&= \frac{(\alpha-1)e^{\sqrt{c}(\ell_j-\delta_{j-1})} + (\alpha+1)e^{\sqrt{c}\delta_{j-1}}}{(\alpha+1)e^{\sqrt{c}\ell_j} + (\alpha-1)}, \qquad (3.33) \\
&= 1 + \frac{(\alpha-1)e^{\sqrt{c}(\ell_j-\delta_{j-1})} + (\alpha+1)e^{\sqrt{c}\delta_{j-1}} - (\alpha+1)e^{\sqrt{c}\ell_j} - (\alpha-1)}{(\alpha+1)e^{\sqrt{c}\ell_j} + (\alpha-1)}, \\
&= 1 + \frac{(\alpha-1)(e^{\sqrt{c}(\ell_j-\delta_{j-1})} - 1) + (\alpha+1)e^{\sqrt{c}\delta_{j-1}}(1 - e^{\sqrt{c}(\ell_j-\delta_{j-1})})}{(\alpha+1)e^{\sqrt{c}\ell_j} + (\alpha-1)}, \\
&= 1 - (e^{\sqrt{c}(\ell_j-\delta_{j-1})} - 1) \cdot \frac{(\alpha+1)e^{\sqrt{c}\delta_{j-1}} - (\alpha-1)}{(\alpha+1)e^{\sqrt{c}\ell_j} + (\alpha-1)}, \\
&< 1,
\end{aligned}
$$

where the last inequality is concluded from $e^{\sqrt{c}(\ell_j-\delta_{j-1})} > 1$ and $(\alpha+1)e^{\sqrt{c}\delta_{j-1}} > (\alpha-1)$. Similarly for $\alpha \geq 1$,

$$|q_j^\dagger| + |s_j^\dagger| < 1.$$

For $\alpha < 1$, we need to change the sign of $p_j^\dagger$:

$$\begin{aligned}
|p_j^\dagger| + |r_j^\dagger| &= -p_j^\dagger + r_j^\dagger, \\
&= -\frac{(\alpha^2-1)e^{\sqrt{c}\delta_{j-1}} - (\alpha^2-1)e^{\sqrt{c}(2\ell_j-\delta_{j-1})}}{(\alpha-1)^2-(\alpha+1)^2e^{2\sqrt{c}\ell_j}} \\
&\qquad\qquad + \frac{(\alpha-1)^2e^{\sqrt{c}(\ell_j-\delta_{j-1})} - (\alpha+1)^2e^{\sqrt{c}(\ell_j+\delta_{j-1})}}{(\alpha-1)^2-(\alpha+1)^2e^{2\sqrt{c}\ell_j}}, \\
&= \frac{-(\alpha+1)e^{\sqrt{c}\delta_{j-1}}\big[(\alpha-1)+(\alpha+1)e^{\sqrt{c}\ell_j}\big]}{(\alpha-1)^2-(\alpha+1)^2e^{2\sqrt{c}\ell_j}} \\
&\qquad\qquad + \frac{(\alpha-1)e^{\sqrt{c}(\ell_j-\delta_{j-1})}\big[(\alpha-1)+(\alpha+1)e^{\sqrt{c}\ell_j}\big]}{(\alpha-1)^2-(\alpha+1)^2e^{2\sqrt{c}\ell_j}}, \\
&= \frac{\big[(\alpha-1)e^{\sqrt{c}(\ell_j-\delta_{j-1})} - (\alpha+1)e^{\sqrt{c}\delta_{j-1}}\big]\big[(\alpha-1)+(\alpha+1)e^{\sqrt{c}\ell_j}\big]}{(\alpha-1)^2-(\alpha+1)^2e^{2\sqrt{c}\ell_j}}, \\
&= \frac{(\alpha-1)e^{\sqrt{c}(\ell_j-\delta_{j-1})} - (\alpha+1)e^{\sqrt{c}\delta_{j-1}}}{-(\alpha+1)e^{\sqrt{c}\ell_j}+(\alpha-1)}, \qquad (3.34) \\
&= 1 + \frac{(\alpha-1)e^{\sqrt{c}(\ell_j-\delta_{j-1})} - (\alpha+1)e^{\sqrt{c}\delta_{j-1}} + (\alpha+1)e^{\sqrt{c}\ell_j} - (\alpha-1)}{-(\alpha+1)e^{\sqrt{c}\ell_j}+(\alpha-1)}, \\
&= 1 + \frac{(\alpha-1)(e^{\sqrt{c}(\ell_j-\delta_{j-1})}-1) + (\alpha+1)e^{\sqrt{c}\delta_{j-1}}(e^{\sqrt{c}(\ell_j-\delta_{j-1})}-1)}{-(\alpha+1)e^{\sqrt{c}\ell_j}+(\alpha-1)}, \\
&= 1 + (e^{\sqrt{c}(\ell_j-\delta_{j-1})}-1)\frac{(\alpha-1)+(\alpha+1)e^{\sqrt{c}\delta_{j-1}}}{-(\alpha+1)e^{\sqrt{c}\ell_j}+(\alpha-1)}, \\
&< 1,
\end{aligned}$$

since $\alpha - 1 < 0 < (\alpha+1)e^{\sqrt{c}\delta_{j-1}}$ and $-(\alpha+1)e^{\sqrt{c}\ell_j} + (\alpha-1) < 0$ for $\alpha < 1$. Similarly, for $\alpha < 1$, we have

$$|q_j^\dagger| + |s_j^\dagger| < 1.$$

Hence, the inequalities hold for any non-negative α. □

Theorem 3.1.6. Let $\mathcal{S}$ be any closed 1-manifold partitioned according to Definition 3.1.1 with $N \geq 2$. The OPS iterations (3.22) for the positive Helmholtz equation on $\mathcal{S}$ converges globally on an arbitrary number of subdomains for any $\alpha \geq 0$.

Proof. We must show $\rho(\mathbf{M}_{\text{OPS}}) < 1$ to prove convergence. Noting that $\mathbf{M}_{\text{OPS}} = \mathbf{M}\mathbf{M}^\dagger\mathbf{M}^{-1}$, we see that $\mathbf{M}_{\text{OPS}}$ and $\mathbf{M}^\dagger$ are similar matrices, and consequently, they share common eigenvalues, i.e., their spectral radii are equal. Thus, for convergence it is sufficient to show

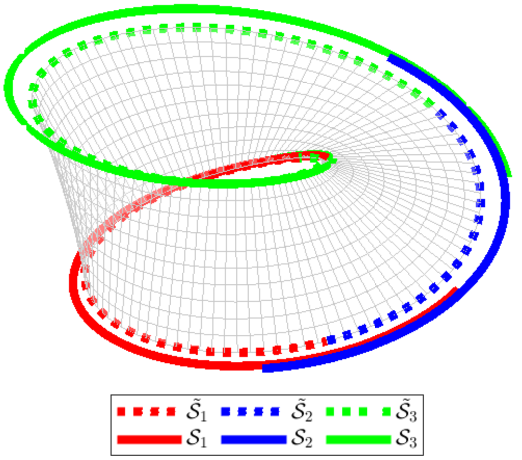

Figure 3.10: Partitioning of the edge of the Möbius strip.

$\rho(\mathbf{M}^\dagger) < 1$. Further, one may use the inequality $\rho(\mathbf{M}^\dagger) \leq ||\mathbf{M}^\dagger||_\infty$. Now,

$$\rho(\mathbf{M}_{\text{OPS}}) = \rho(\mathbf{M}^\dagger) \leq ||\mathbf{M}^\dagger||_\infty = \max\{|p_1^\dagger| + |r_1^\dagger|, |q_1^\dagger| + |s_1^\dagger|, \ldots, |p_N^\dagger| + |r_N^\dagger|, |q_N^\dagger| + |s_N^\dagger|\}$$

In Lemma 3.1.5, we have shown that $|p_j^\dagger| + |r_j^\dagger| < 1$ and $|q_j^\dagger| + |s_j^\dagger| < 1$ for any non-negative values of α. Therefore, $||\mathbf{M}^\dagger||_\infty$, which is the maximum of absolute row sums, is strictly less than one, i.e.,

$$\rho(\mathbf{M}_{\text{OPS}}) = \rho(\mathbf{M}^\dagger) \leq ||\mathbf{M}^\dagger||_\infty = \max\{|p_1^\dagger| + |r_1^\dagger|, |q_1^\dagger| + |s_1^\dagger|, \ldots, |p_N^\dagger| + |r_N^\dagger|, |q_N^\dagger| + |s_N^\dagger|\} < 1$$

Hence, the iterations of (3.22) converges for any $\alpha \geq 0$. □

Once again, we emphasize that the partitioning used for the theorem is not necessarily overlapping. That is, the OPS method is also convergent with non-overlapping subdomains. In order to numerically verify the theorem, we solve (3.22) on the boundary of a Möbius strip with width 1, whose center circle has radius 1. The edge of the Möbius strip is partitioned into three disjoint subdomains with ratios 2:3:5 as shown in Figure 3.10. Once again, (3.22) is implemented in MATLAB. The implementation is the same as the CPS iterations, but the boundary conditions need to be changed. The Robin boundary condition $\mathcal{B}^-$ is discretized with first order forward finite differences, while $\mathcal{B}^+$ is approximated by first order backward finite differences.

Given the initial condition $\epsilon^0(s) = 1$, the global solutions at different iterations are shown in Figure 3.11. The error plots are shown in Figure 3.12 for $\alpha = 0.5$ and $\alpha = 4$. The algorithm clearly converges for $\alpha = 0.5$ and $\alpha = 4$, while $\alpha = 0.5$ shows a better decay rate. $\alpha = 0.5$ reaches the MATLAB threshold of $2^{-1023} \approx 10^{-308}$ for the smallest positive normalized floating-point number in IEEE® double precision. The decay rates are equal to the spectral radii of the corresponding iteration matrices and are bounded by the max-

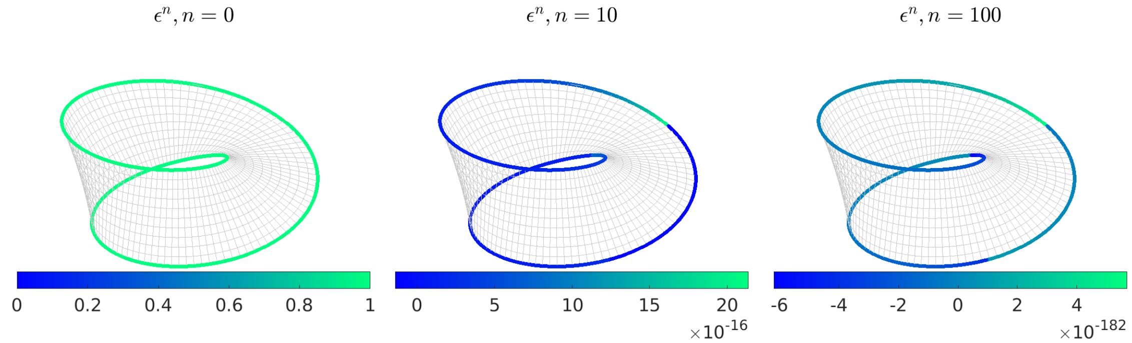

Figure 3.11: Global solution to (3.22) on the the edge of the Möbius strip at different iterations with $c = 1$ and $\alpha = 1$.

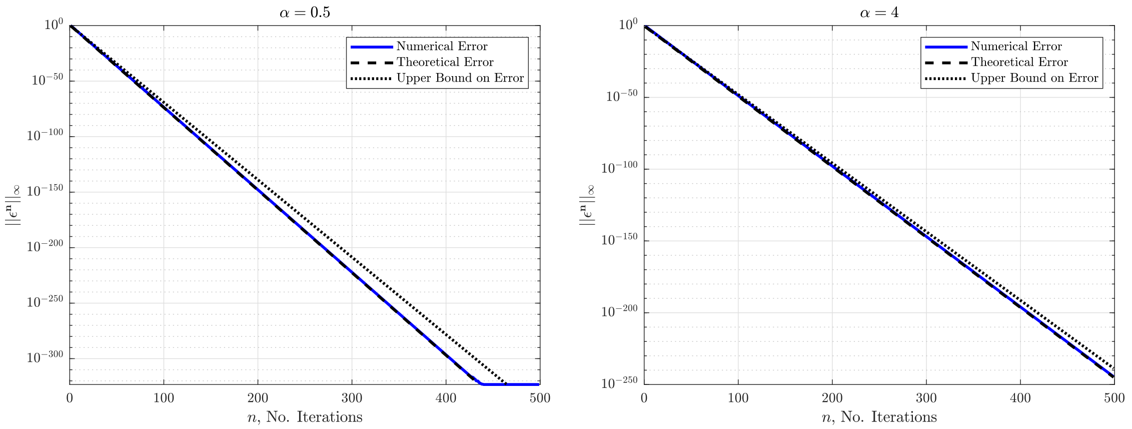

Figure 3.12: Decay rate of the max-norm of error vector for different Robin parameters.

norms. The max-norm of the iteration matrix is a better upper bound on the spectral radius when $\alpha = 4$. We now present a corollary about the Robin parameter that is important to our analysis.

Corollary 3.1.5. The OPS iterations (3.22) with $\alpha = \alpha^\star \geq 0$ converges with the same convergence factor as $\alpha = 1/\alpha^\star$.

Proof. We need to show the corresponding iteration matrices have the same spectral radii. Further, it is sufficient to show the corresponding $\mathbf{M}^\dagger$ matrices share the same spectral radii. By a direct substitution in (3.27), one obtains

$$p_j^\dagger(\alpha^\star) = -p_j^\dagger(\frac{1}{\alpha^\star}), \qquad\qquad r_j^\dagger(\alpha^\star) = r_j^\dagger(\frac{1}{\alpha^\star}).$$

Similarly,

$$q_j^\dagger(\alpha^\star) = -q_j^\dagger(\frac{1}{\alpha^\star}), \qquad\qquad s_j^\dagger(\alpha^\star) = s_j^\dagger(\frac{1}{\alpha^\star}).$$

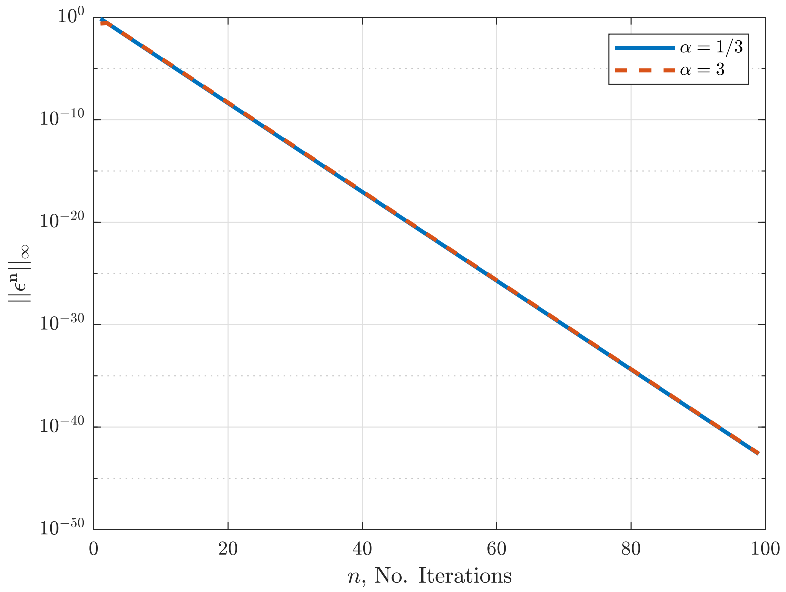

Figure 3.13: Convergence factor of (3.22) with a Robin parameter and its reciprocal.

Introducing a $2N \times 2N$ permutation matrix $P = [a_{ij}]$ where

$$a_{ij} = \begin{cases} (-1)^{i+1}; & i = j, \\ \\ 0; & i \neq j, \end{cases}$$

we have $\mathbf{M}^\dagger(\alpha^\star) = P^{-1}\mathbf{M}^\dagger(\dfrac{1}{\alpha^\star})P$. Notice that $P^{-1} = P$. Hence, $\mathbf{M}^\dagger(\alpha^\star)$ and $\mathbf{M}^\dagger\left(\dfrac{1}{\alpha^\star}\right)$ are similar matrices, sharing the same spectral radii. □

We can easily verify the corollary by comparing the decay rate of iterations (3.22) with an arbitrary α and $1/\alpha$. Taking $\alpha = 3$, Figure 3.13 shows the decay rate of the OPS method on the partitioning shown in Figure 3.10 and indicates that the convergence factors for $\alpha = 3$ and $\alpha = 1/3$ are identical. We draw our attention to the extreme cases of the Robin parameter, $\alpha = 0$ and $\alpha \to \infty$. By a direct substitution, one obtains

$$\begin{aligned} \lim_{\alpha \to \infty} p_j^\dagger(\alpha) = -p_j^\dagger(\alpha = 0) &= \frac{1 - e^{2\sqrt{c}(\ell_j - \delta_{j-1})}}{1 - e^{2\sqrt{c}\ell_j}} e^{\sqrt{c}\delta_{j-1}}, \\ \lim_{\alpha \to \infty} r_j^\dagger(\alpha) = r_j^\dagger(\alpha = 0) &= \frac{1 - e^{2\sqrt{c}\delta_{j-1}}}{1 - e^{2\sqrt{c}\ell_j}} e^{\sqrt{c}(\ell_j - \delta_{j-1})}, \end{aligned}$$

for $j = 1, \ldots, N$, where the right-hand sides are the quantities defined for the classical Schwarz algorithms in (3.9). Likewise, $q_j^\dagger$ and $s_j^\dagger$ are equal to their counterparts in the classical Schwarz methods in the limit $\alpha \to \infty$. That is, the OPS method is consistent with the CPS method in the limit $\alpha \to \infty$. In other words, increasing α decreases the effect of the Neumann part in the Robin boundary condition. Neglecting the Neumann part in iterations (3.22) yields the same iterations as in (3.5). Moreover, $\alpha = 0$ gives the same values for $r_j^\dagger$ and $s_j^\dagger$ as r_j and s_j in (3.9), respectively. Although $p_j^\dagger$ and $q_j^\dagger$ are off by a negative sign from p_j and q_j in (3.9) when $\alpha = 0$, the convergence factors of the OPS and CPS methods are equal, following Corollary 3.1.5. We continue the discussion on the OPS method by presenting the convergence factor of the method on an equal-sized partitioning. We show the convergence factor for $\alpha \geq 1$, but one can find the convergence factor for $0 \leq \alpha < 1$ using the following corollary and Corollary 3.1.5.

Corollary 3.1.6. The OPS iterations (3.22) with $\alpha \geq 1$ for the positive Helmholtz equation on any closed 1-manifold partitioned into $N \geq 2$ equal-sized subdomains and overlaps, according to Definition 3.1.2, converges with the rate of:

$$\kappa = \frac{(\alpha - 1)e^{\sqrt{c}L/N} + (\alpha + 1)e^{\sqrt{c}\delta}}{(\alpha + 1)e^{\sqrt{c}(L/N+\delta)} + (\alpha - 1)}.$$

Proof. We investigate the spectral radius of $\mathbf{M}^\dagger$ as it is similar to the iteration matrix $\mathbf{M}_{\text{OPS}}$. For the overlapping equal-sized partitioning in Definition 3.1.2 with $0 \leq \delta < L/N$, we have

$$p_1^\dagger = p_2^\dagger = \cdots = p_N^\dagger = q_1^\dagger = q_2^\dagger = \cdots = q_N^\dagger,$$
$$r_1^\dagger = r_2^\dagger = \cdots = r_N^\dagger = s_1^\dagger = s_2^\dagger = \cdots = s_N^\dagger.$$

Setting $p^\dagger = p_j^\dagger$ and $r^\dagger = r_j^\dagger$ for $j = 1, \ldots, N$, we have

$$\mathbf{M}^\dagger = \begin{bmatrix}
0 & 0 & r^\dagger & & & & & & & & & & p^\dagger \\
0 & 0 & p^\dagger & & & & & & & & & & r^\dagger \\
 & p^\dagger & 0 & 0 & r^\dagger & & & & & & & & \\
 & r^\dagger & 0 & 0 & p^\dagger & & & & & & & & \\
 & & & p^\dagger & 0 & 0 & r^\dagger & & & & & & \\
 & & & r^\dagger & 0 & 0 & p^\dagger & & & & & & \\
 & & & & & \ddots & \ddots & \ddots & \ddots & & & & \\
 & & & & & & \ddots & \ddots & \ddots & \ddots & & & \\
 & & & & & & & & p^\dagger & 0 & 0 & r^\dagger & \\
 & & & & & & & & r^\dagger & 0 & 0 & p^\dagger & \\
r^\dagger & & & & & & & & & & p^\dagger & 0 & 0 \\
p^\dagger & & & & & & & & & & r^\dagger & 0 & 0
\end{bmatrix}. \tag{3.35}$$

Note that the convergence is a direct consequence of Theorem 3.1.6. From Lemma 3.1.5 and with $\alpha \geq 1$, $\mathbf{M}^\dagger$ is a non-negative matrix, i.e, all entries of the matrix are non-negative. In addition, it has the same structure as the iteration matrix in (3.12), hence it is irreducible. The Perron-Frobenius theorem states that the maximal eigenvalue of a non-negative irre-

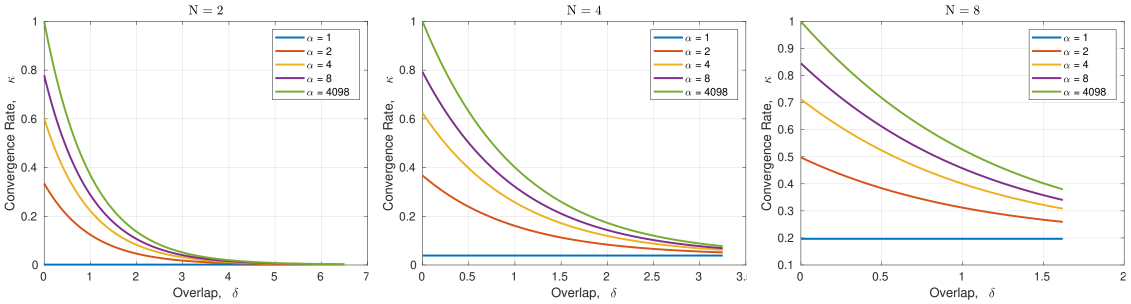

Figure 3.14: Convergence factor of the OPS method versus the overlap in an equal-sized partitioning configuration with different N and α. In the left panel, the convergence factor for $\alpha = 1$ is $e^{-L/2} \approx 0.0015$.

ducible matrix – the spectral radius – is bounded by the minimum and maximum of the row sums [6]. Having the same row sums for all the rows yields

$$\kappa = \rho(\mathbf{M}_{\text{OPS}}) = \rho(\mathbf{M}^{\dagger}) = ||\mathbf{M}^{\dagger}||_{\infty} = |p^{\dagger}| + |r^{\dagger}| = \frac{(\alpha-1)e^{\sqrt{c}L/N} + (\alpha+1)e^{\sqrt{c}\delta}}{(\alpha+1)e^{\sqrt{c}(L/N+\delta)} + (\alpha-1)},$$

where the last equality comes from Equation (3.33). □

Note that the above corollary does not provide the convergence factor for $0 \leq \alpha < 1$, but utilizing Corollary 3.1.5 suggests

$$\kappa = \frac{(1/\alpha-1)e^{\sqrt{c}L/N} + (1/\alpha+1)e^{\sqrt{c}\delta}}{(1/\alpha+1)e^{\sqrt{c}(L/N+\delta)} + (1/\alpha-1)} = \frac{(1-\alpha)e^{\sqrt{c}L/N} + (1+\alpha)e^{\sqrt{c}\delta}}{(1+\alpha)e^{\sqrt{c}(L/N+\delta)} + (1-\alpha)},$$

for $0 \leq \alpha < 1$ when the domain with length L is partitioned into $N \geq 2$ subdomains of equal size and equal overlap δ. Figure 3.14 illustrates the convergence factor of the OPS algorithm on the Möbius edge ($L \approx 13.006$) against the overlap size for different α and N. We do not provide the plots for $0 \leq \alpha < 1$ as they have the same convergence as $1/\alpha$. In addition, $\alpha = 1$ results in the constant convergence factor $\kappa = e^{-\sqrt{c}L/N}$ for any amount of overlap. Furthermore, $\alpha = 4098$ behaves approximately similar to Figure 3.5, as the Dirichlet term outweighs the Neumann term in the Robin boundary condition. Note that we still get a convergent method for non-overlapping partitioning with an acceptable convergence factor. As we observe, one can obtain the best convergence factor with $\alpha = 1$. Moreover, this can be obtained with the cheapest computational cost of non-overlapping partitioning. We can theoretically prove that $\alpha = 1$ is the Robin parameter with the best convergence factor for an equal-sized partitioning, but a robust theory is needed for the general partitioning as the convergence factor is highly affected by the Robin parameter. The following lemma helps us to find the optimized α value which gives the best convergence factor.

Lemma 3.1.7. Suppose the Robin parameter is restricted to be greater than 1, i.e., $\alpha \geq 1$. For the partitioning specified in Definition 3.1.1, $\alpha = 1$ is the minimizer of $p_j^\dagger$, $r_j^\dagger$, $q_j^\dagger$ and $s_j^\dagger$ for all $j = 1, \ldots, N$.

Proof. $p_j^\dagger$ in (3.27) can be rewritten as:

$$p_j^\dagger = (\alpha^2 - 1)\frac{1 - e^{2\sqrt{c}(\ell_j - \delta_{j-1})}}{(\alpha - 1)^2 - (\alpha + 1)^2 e^{2\sqrt{c}\ell_j}} e^{\sqrt{c}\delta_{j-1}}.$$

The denominator $(\alpha - 1)^2 - (\alpha + 1)^2 e^{2\sqrt{c}\ell_j} = (1 - e^{2\sqrt{c}\ell_j})\alpha^2 - 2(1 + e^{2\sqrt{c}\ell_j})\alpha + (1 - e^{2\sqrt{c}\ell_j})$ is a decreasing function for $\alpha \geq 1$, while the numerator $\alpha^2 - 1$ increases as α increases. Thus, $p_j^\dagger$ is increasing over the interval $[1, \infty)$, and $\alpha = 1$ minimizes $p_j^\dagger$. Likewise, $\alpha = 1$ is the minimizer of $q_j^\dagger$. Next, we show the proof that $\alpha = 1$ minimizes $r_j^\dagger$. The proof for $s_j^\dagger$ can similarly be concluded. From (3.27),

$$\begin{aligned}
r_j^\dagger &= \frac{(\alpha - 1)^2 - (\alpha + 1)^2 e^{2\sqrt{c}\delta_{j-1}}}{(\alpha - 1)^2 - (\alpha + 1)^2 e^{2\sqrt{c}\ell_j}} e^{\sqrt{c}(\ell_j - \delta_{j-1})}, \\
&= \frac{(1 - e^{2\sqrt{c}\delta_{j-1}})\alpha^2 - 2(1 + e^{2\sqrt{c}\delta_{j-1}})\alpha + (1 - e^{2\sqrt{c}\delta_{j-1}})}{(1 - e^{2\sqrt{c}\ell_j})\alpha^2 - 2(1 + e^{2\sqrt{c}\ell_j})\alpha + (1 - e^{2\sqrt{c}\ell_j})} \cdot \frac{e^{\sqrt{c}\ell_j}}{e^{\sqrt{c}\delta_{j-1}}}, \\
&= \frac{e^{\sqrt{c}\ell_j}}{e^{\sqrt{c}\delta_{j-1}}} \cdot \frac{(1 - e^{2\sqrt{c}\delta_{j-1}})}{(1 - e^{2\sqrt{c}\ell_j})} \cdot \frac{\alpha^2 - 2(1 + 2e^{2\sqrt{c}\delta_{j-1}}/(1 - e^{2\sqrt{c}\delta_{j-1}}))\alpha + 1}{\alpha^2 - 2(1 + 2e^{2\sqrt{c}\ell_j}/(1 - e^{2\sqrt{c}\ell_j}))\alpha + 1}, \\
&= \frac{e^{\sqrt{c}\ell_j}}{e^{\sqrt{c}\delta_{j-1}}} \cdot \frac{(1 - e^{2\sqrt{c}\delta_{j-1}})}{(1 - e^{2\sqrt{c}\ell_j})} \\
&\qquad \cdot \left[1 + 4\left[\frac{e^{2\sqrt{c}\delta_{j-1}}}{1 - e^{2\sqrt{c}\delta_{j-1}}} + \frac{e^{2\sqrt{c}\ell_j}}{1 - e^{2\sqrt{c}\ell_j}}\right] \underbrace{\left[\frac{\alpha}{\alpha^2 - 2(1 + 2e^{2\sqrt{c}\ell_j}/(1 - e^{2\sqrt{c}\ell_j}))\alpha + 1}\right]}_{f(\alpha)} \right].
\end{aligned}$$

Differentiating $f(\alpha)$ with respect to α yields,

$$\begin{aligned}
\frac{\mathrm{d}}{\mathrm{d}\alpha} f &= \frac{\alpha^2 - 2(1 + 2e^{2\sqrt{c}\ell_j}/(1 - e^{2\sqrt{c}\ell_j}))\alpha + 1 - \alpha(2\alpha - 2(1 + 2e^{2\sqrt{c}\ell_j}/(1 - e^{2\sqrt{c}\ell_j})))}{(\alpha^2 - 2(1 + 2e^{2\sqrt{c}\ell_j}/(1 - e^{2\sqrt{c}\ell_j}))\alpha + 1)^2}, \\
&= \frac{-\alpha^2 + 1}{(\alpha^2 - 2(1 + 2e^{2\sqrt{c}\ell_j}/(1 - e^{2\sqrt{c}\ell_j}))\alpha + 1)^2}.
\end{aligned}$$

The critical points of $r_j^\dagger$ are $\alpha = \pm 1$ and the zeros of its denominator are $\alpha = (1 - e^{\sqrt{c}\ell_j})/(1 + e^{\sqrt{c}\ell_j})$ and $\alpha = (1 + e^{\sqrt{c}\ell_j})/(1 - e^{\sqrt{c}\ell_j})$. All the critical points are negative, except $\alpha = 1$. Hence, $\alpha = 1$ minimizes $r_j^\dagger$ and $s_j^\dagger$ with a similar reasoning. Notice that the minimizer is independent of the partitioning. □

We state a lemma on the monotonicity of the spectral radius for non-negative irreducible matrices.

Lemma 3.1.8. Suppose A and B are two irreducible matrices with non-negative entries. Further, we suppose $A < B$ by which we mean that any non-zero component in A is less than the corresponding entry in B. Hence, $\rho(A) < \rho(B)$.

Proof. A similar proof of this lemma can be found in [6], however, we provide our proof as well. From the Perron-Frobenius theorem, the spectral radius of a non-negative irreducible matrix is an eigenvalue, and the elements of the corresponding eigenvector are all non-negative [6]. Suppose r is the eigenvalue and x denotes the corresponding eigenvector. Thus, $Ax_A = r_A x_A$ and $Bx_B = r_B x_B$. If we multiply the inequality $A < B$ by $x_B > 0$, we obtain $Ax_B < Bx_B = r_B x_B$. Thus, $Ax_B < r_B x_B$. We let $||\cdot||_{x_B}$ be a norm such that $||x_B||_{x_B} = 1$. Thus, $||A||_{x_B} = \sup_{||x||_{x_B}=1} ||Ax||_{x_B} = ||Ax_B||_{x_B}$ since the matrix and the vector are non-negative. Subsequently,

$$||A||_{x_B} = ||Ax_B||_{x_B} < ||r_B x_B||_{x_B} = r_B.$$

Since the spectral radius is the infimum of all norms, $r_A \leq ||A||_{x_B} < r_B$. Equivalently, $\rho(A) < \rho(B)$. □

Employing Lemma 3.1.7 and Lemma 3.1.8, we find the α value that has the best decay rate.

Theorem 3.1.9. For a given partitioning of a closed 1-manifold based on Definition 3.1.1, the OPS iterations (3.22) with $\alpha = 1$ for the positive Helmholtz equation converges faster than any other $\alpha \geq 0$.

Proof. We show that the spectral radius of $\mathbf{M}^\dagger$ corresponding to $\alpha = 1$ is less than the the spectral radius of the same matrix with any $\alpha > 1$. According to Lemma 3.1.7, $\alpha = 1$ minimizes the quantities in Equation (3.27) which appear in $\mathbf{M}^\dagger$. Hence, we write $\mathbf{M}^\dagger(\alpha = 1) < \mathbf{M}^\dagger(\alpha)$ for any $\alpha > 1$ to denote that any non-zero element in $\mathbf{M}^\dagger(\alpha = 1)$ is less than the element at the same row and column in $\mathbf{M}^\dagger(\alpha)$. It has been shown in Corollary 3.1.5 that $\mathbf{M}^\dagger$ is a non-negative irreducible matrix for any $\alpha \geq 1$. For now, let us define $A = \mathbf{M}^\dagger(\alpha = 1)$ and $B = \mathbf{M}^\dagger(\alpha)$ for any $\alpha > 1$. Since A and B are non-negative irreducible matrices, we exploit the result of Lemma 3.1.8 to obtain $\rho(A) < \rho(B)$. That is, the spectral radius of $\mathbf{M}^\dagger$ with $\alpha = 1$ is minimal over $\alpha \geq 1$. From the similarity of $\mathbf{M}^\dagger$ and the iteration matrix $\mathbf{M}_{\text{OPS}}$, $\mathbf{M}_{\text{OPS}}$ with $\alpha = 1$ is the minimum for any other $\alpha \geq 1$. Corollary 3.1.5 also shows that the OPS iteration with $0 \leq \alpha \leq 1$ converges with the same rate as the OPS iteration with $1/\alpha$. Thus, $\alpha = 1$ minimizes the spectral radius of $\mathbf{M}_{\text{OPS}}$. □

The above theorem proves that the best convergence factor of the OPS iteration is obtained with $\alpha = 1$. With $\alpha = 1$, we have the same weight for the Neumann and Dirichlet

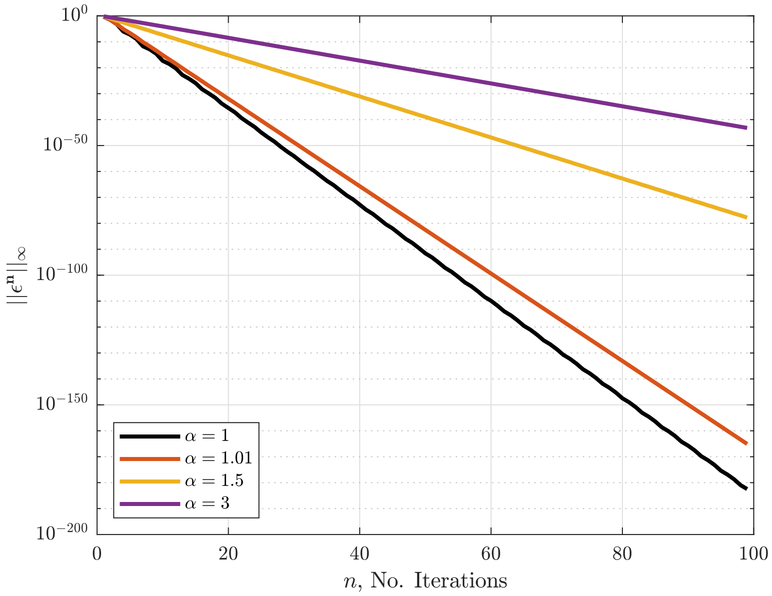

Figure 3.15: Convergence factor of the OPS method with different Robin parameters for the Möbius strip shown in Figure 3.10.

terms in the transmission condition. The result is reasonable as we solve the one-dimensional positive Helmholtz equation on a periodic domain, and we could expect that having the same weights for the terms in the transmission condition is ideal for obtaining the best convergence factor. We now numerically verify the theorem. We run the OPS algorithm on the curve defined by the edge of the Möbius strip shown in Figure 3.10 with different values for the Robin parameter. The results are shown in Figure 3.15. As we observe, $\alpha = 1$ yields the best convergence factor, and small changes to the optimal α results in a considerably different convergence factor. In addition, one can interpret Theorem 3.1.9 as a proof of monotonicity of the spectral radius of the OAS iteration with α. In Figure 3.15, the convergence factor reduces as we increase the Robin parameter.

3.1.4 The OAS-CPM

Similar to the OPS-CPM, the OAS-CPM for a closed 1-manifold is consistent with the following Schwarz method:

$$\begin{cases} (c - \frac{\mathrm{d}^2}{\mathrm{d}s^2})\epsilon_j^{n+1} = 0, & \text{for } s \in [a_j, b_j], \\ (\alpha - \frac{\mathrm{d}}{\mathrm{d}s})\epsilon_j^{n+1}(a_j) = (\alpha - \frac{\mathrm{d}}{\mathrm{d}s})\epsilon_{j-1}^{n+1}(a_j), \\ (\alpha + \frac{\mathrm{d}}{\mathrm{d}s})\epsilon_j^{n+1}(b_j) = (\alpha + \frac{\mathrm{d}}{\mathrm{d}s})\epsilon_{j+1}^{n}(b_j), \end{cases} \tag{3.36}$$

with the solution:

$$\epsilon_j^{n+1}(s) = \frac{e^{\sqrt{c}(s-a_j)} - e^{\sqrt{c}(b_j-s+\ell_j)}}{1 - e^{2\sqrt{c}\ell_j}}\mathcal{B}^-\epsilon_{j-1}^{n+1}(a_j) + \frac{e^{\sqrt{c}(b_j-s)} - e^{\sqrt{c}(s-a_j+\ell_j)}}{1 - e^{2\sqrt{c}\ell_j}}\mathcal{B}^+\epsilon_{j+1}^{n}(b_j), \tag{3.37}$$

for $j = 1, \ldots, N$, and (3.4) still applies.

Using Equation (3.37), the error values at the boundaries are:

$$\begin{cases} \epsilon_j^{n+1}(b_{j-1}) = p_j\mathcal{B}^-\epsilon_{j-1}^{n+1}(a_j) + r_j\mathcal{B}^+\epsilon_{j+1}^{n}(b_j), \\ \epsilon_j^{n+1}(a_{j+1}) = s_j\mathcal{B}^-\epsilon_{j-1}^{n+1}(a_j) + q_j\mathcal{B}^+\epsilon_{j+1}^{n}(b_j), \end{cases} \tag{3.38}$$

where the quantities p_j, r_j, q_j, and s_j are introduced in Equation (3.25). By applying the boundary operator to Equation (3.37), one obtains

$$\begin{cases} \mathcal{B}^+\epsilon_j^{n+1}(b_{j-1}) = p_j^\dagger\mathcal{B}^-\epsilon_{j-1}^{n+1}(a_j) + r_j^\dagger\mathcal{B}^+\epsilon_{j+1}^{n}(b_j), \\ \mathcal{B}^-\epsilon_j^{n+1}(a_{j+1}) = s_j^\dagger\mathcal{B}^-\epsilon_{j-1}^{n+1}(a_j) + q_j^\dagger\mathcal{B}^+\epsilon_{j+1}^{n}(b_j), \end{cases} \tag{3.39}$$

where $p_j^\dagger$, $r_j^\dagger$, $q_j^\dagger$, and $s_j^\dagger$ are defined in Equation (3.27). It is needed to have only values at iteration n on the right-hand side. Thus the terms containing $\mathcal{B}^-\epsilon_{j-1}^{n+1}(a_j)$ must be replaced. Similar to the CAS-CPM section, by working from the first subdomain to the j^{th} subdomain in the second equation of (3.38), we find $\mathcal{B}^-\epsilon_{j-1}^{n+1}(a_j)$ as

$$\begin{aligned} \mathcal{B}^-\epsilon_{j-1}^{n+1}(a_j) = s_{j-1}^\dagger s_{j-2}^\dagger \ldots s_2^\dagger q_1^\dagger \mathcal{B}^+\epsilon_2^n(b_1) + s_{j-1}^\dagger s_{j-2}^\dagger \ldots s_3^\dagger q_2^\dagger \mathcal{B}^+\epsilon_3^n(b_2) + \ldots \\ + q_{j-1}^\dagger\mathcal{B}^+\epsilon_j^n(b_{j-1}) + s_{j-1}^\dagger s_{j-2}^\dagger \ldots s_1^\dagger \mathcal{B}^-\epsilon_N^n(a_1 + L). \end{aligned} \tag{3.40}$$

Substituting (3.40) back into Equations (3.38) and (3.39), we obtain

$$\begin{cases}
\epsilon_j^{n+1}(b_{j-1}) = p_j\Big[s^\dagger_{j-1}s^\dagger_{j-2}\dots s^\dagger_2 q^\dagger_1\mathcal{B}^+\epsilon^n_2(b_1) + s^\dagger_{j-1}s^\dagger_{j-2}\dots s^\dagger_3 q^\dagger_2\mathcal{B}^+\epsilon^n_3(b_2)+\dots \\
\qquad\qquad +q^\dagger_{j-1}\mathcal{B}^+\epsilon^n_j(b_{j-1}) + s^\dagger_{j-1}s^\dagger_{j-2}\dots s^\dagger_1\mathcal{B}^-\epsilon^n_N(a_1+L)\Big] + r_j\mathcal{B}^+\epsilon^n_{j+1}(b_j), \\
\epsilon_j^{n+1}(a_{j+1}) = s_j\Big[s^\dagger_{j-1}s^\dagger_{j-2}\dots s^\dagger_2 q^\dagger_1\mathcal{B}^+\epsilon^n_2(b_1) + s^\dagger_{j-1}s^\dagger_{j-2}\dots s^\dagger_3 q^\dagger_2\mathcal{B}^+\epsilon^n_3(b_2)+\dots \\
\qquad\qquad +q^\dagger_{j-1}\mathcal{B}^+\epsilon^n_j(b_{j-1}) + s^\dagger_{j-1}s^\dagger_{j-2}\dots s^\dagger_1\mathcal{B}^-\epsilon^n_N(a_1+L)\Big] + q_j\mathcal{B}^+\epsilon^n_{j+1}(b_j), \\
\mathcal{B}^+\epsilon_j^{n+1}(b_{j-1}) = p^\dagger_j\Big[s^\dagger_{j-1}s^\dagger_{j-2}\dots s^\dagger_2 q^\dagger_1\mathcal{B}^+\epsilon^n_2(b_1) + s^\dagger_{j-1}s^\dagger_{j-2}\dots s^\dagger_3 q^\dagger_2\mathcal{B}^+\epsilon^n_3(b_2)+\dots \\
\qquad\qquad +q^\dagger_{j-1}\mathcal{B}^+\epsilon^n_j(b_{j-1}) + s^\dagger_{j-1}s^\dagger_{j-2}\dots s^\dagger_1\mathcal{B}^-\epsilon^n_N(a_1+L)\Big] + r^\dagger_j\mathcal{B}^+\epsilon^n_{j+1}(b_j), \\
\mathcal{B}^-\epsilon_j^{n+1}(a_{j+1}) = s^\dagger_j\Big[s^\dagger_{j-1}s^\dagger_{j-2}\dots s^\dagger_2 q^\dagger_1\mathcal{B}^+\epsilon^n_2(b_1) + s^\dagger_{j-1}s^\dagger_{j-2}\dots s^\dagger_3 q^\dagger_2\mathcal{B}^+\epsilon^n_3(b_2)+\dots \\
\qquad\qquad +q^\dagger_{j-1}\mathcal{B}^+\epsilon^n_j(b_{j-1}) + s^\dagger_{j-1}s^\dagger_{j-2}\dots s^\dagger_1\mathcal{B}^-\epsilon^n_N(a_1+L)\Big] + q^\dagger_j\mathcal{B}^+\epsilon^n_{j+1}(b_j).
\end{cases} \tag{3.41}$$

To rewrite the above equations in matrix form, we define an error vector at the $s = b_j$ points:

$$\boldsymbol{\epsilon}^n := [\epsilon^n_2(b_1), \epsilon^n_3(b_2), \dots, \epsilon^n_N(b_{N-1}), \epsilon^n_N(a_1+L)]^T,$$

and also,

$$\boldsymbol{\mathcal{B}}\boldsymbol{\epsilon}^n := [\mathcal{B}^+\epsilon^n_2(b_1), \mathcal{B}^+\epsilon^n_3(b_2), \dots, \mathcal{B}^+\epsilon^n_N(b_{N-1}), \mathcal{B}^-\epsilon^n_N(a_1+L)]^T.$$

Note that $s = a_j$ are not included in the error vectors since they can be directly calculated using the error values at $s = b_j$. Now, we arrive at

$$\boldsymbol{\epsilon}^{n+1} = \mathbf{M}\boldsymbol{\mathcal{B}}\boldsymbol{\epsilon}^n, \tag{3.42}$$

and for Equation (3.39), we get

$$\boldsymbol{\mathcal{B}}\boldsymbol{\epsilon}^n = \mathbf{M}^\dagger\boldsymbol{\mathcal{B}}\boldsymbol{\epsilon}^{n-1}, \tag{3.43}$$

where $\mathbf{M}$ and $\mathbf{M}^\dagger$ are $N \times N$ matrices defined as follows:

$$\mathbf{M} = \begin{bmatrix} p_2 q_1^\dagger & r_2 & & & & & p_2 s_1^\dagger \\ p_3 s_2^\dagger q_1^\dagger & p_3 q_2^\dagger & r_3 & & & & p_3 s_2^\dagger s_1^\dagger \\ p_4 s_3^\dagger s_2^\dagger q_1^\dagger & p_4 s_3^\dagger q_2^\dagger & p_4 q_3^\dagger & r_4 & & & p_4 s_3^\dagger s_2^\dagger s_1^\dagger \\ \vdots & & & \ddots & \ddots & & \vdots \\ p_{N-1} s_{N-2}^\dagger \cdots s_2^\dagger q_1^\dagger & p_{N-1} s_{N-2}^\dagger \cdots s_3^\dagger q_2^\dagger & \cdots & & p_{N-1} q_{N-2}^\dagger & r_{N-1} & p_{N-1} s_{N-2}^\dagger \cdots s_1^\dagger \\ r_N r_1^\dagger + p_N s_{N-1}^\dagger \cdots s_2^\dagger q_1^\dagger & p_N s_{N-1}^\dagger \cdots s_3^\dagger q_2^\dagger & \cdots & & p_N s_{N-1}^\dagger q_{N-2}^\dagger & p_N q_{N-1}^\dagger & r_N p_1^\dagger + p_N s_{N-1}^\dagger \cdots s_1^\dagger \\ q_N r_1^\dagger + s_N s_{N-1}^\dagger \cdots s_2^\dagger q_1^\dagger & s_N s_{N-1}^\dagger \cdots s_3^\dagger q_2^\dagger & \cdots & & s_N s_{N-1}^\dagger q_{N-2}^\dagger & s_N q_{N-1}^\dagger & q_N p_1^\dagger + s_N s_{N-1}^\dagger \cdots s_1^\dagger \end{bmatrix}, \qquad (3.44)$$

$$\mathbf{M}^\dagger = \begin{bmatrix} p_2^\dagger q_1^\dagger & r_2^\dagger & & & & & p_2^\dagger s_1^\dagger \\ p_3^\dagger s_2^\dagger q_1^\dagger & p_3^\dagger q_2^\dagger & r_3^\dagger & & & & p_3^\dagger s_2^\dagger s_1^\dagger \\ p_4^\dagger s_3^\dagger s_2^\dagger q_1^\dagger & p_4^\dagger s_3^\dagger q_2^\dagger & p_4^\dagger q_3^\dagger & r_4^\dagger & & & p_4^\dagger s_3^\dagger s_2^\dagger s_1^\dagger \\ \vdots & & & \ddots & \ddots & & \vdots \\ p_{N-1}^\dagger s_{N-2}^\dagger \cdots s_2^\dagger q_1^\dagger & p_{N-1}^\dagger s_{N-2}^\dagger \cdots s_3^\dagger q_2^\dagger & \cdots & & p_{N-1}^\dagger q_{N-2}^\dagger & r_{N-1}^\dagger & p_{N-1}^\dagger s_{N-2}^\dagger \cdots s_1^\dagger \\ r_N^\dagger r_1^\dagger + p_N^\dagger s_{N-1}^\dagger \cdots s_2^\dagger q_1^\dagger & p_N^\dagger s_{N-1}^\dagger \cdots s_3^\dagger q_2^\dagger & \cdots & & p_N^\dagger s_{N-1}^\dagger q_{N-2}^\dagger & p_N^\dagger q_{N-1}^\dagger & r_N^\dagger p_1^\dagger + p_N^\dagger s_{N-1}^\dagger \cdots s_1^\dagger \\ q_N^\dagger r_1^\dagger + s_N^\dagger s_{N-1}^\dagger \cdots s_2^\dagger q_1^\dagger & s_N^\dagger s_{N-1}^\dagger \cdots s_3^\dagger q_2^\dagger & \cdots & & s_N^\dagger s_{N-1}^\dagger q_{N-2}^\dagger & s_N^\dagger q_{N-1}^\dagger & q_N^\dagger p_1^\dagger + s_N^\dagger s_{N-1}^\dagger \cdots s_1^\dagger \end{bmatrix}. \qquad (3.45)$$

Equation (3.42) and Equation (3.43) together result in:

$$\boldsymbol{\epsilon}^{n+1} = \mathbf{M}_{\text{OAS}}\boldsymbol{\epsilon}^{n} \tag{3.46}$$

where $\mathbf{M}_{\text{OAS}} = \mathbf{M}\mathbf{M}^{\dagger}\mathbf{M}^{-1}$. We now prove that the OAS method is convergent.

Theorem 3.1.10. Let $\mathcal{S}$ be any closed 1-manifold partitioned according to Definition 3.1.1 with $N \geq 2$. The OAS iterations (3.36) for the positive Helmholtz equation on $\mathcal{S}$ converges globally on an arbitrary number of subdomains for any $\alpha \geq 0$.

Proof. We must show $\rho(\mathbf{M}_{\text{OAS}}) < 1$ to prove the convergence. Considering $\mathbf{M}_{\text{OAS}} = \mathbf{M}\mathbf{M}^{\dagger}\mathbf{M}^{-1}$, $\mathbf{M}_{\text{OAS}}$ and $\mathbf{M}^{\dagger}$ are similar matrices, and they share common eigenvalues. Consequently, their spectral radii are equal. Thus, it is sufficient to show $\rho(\mathbf{M}^{\dagger}) < 1$ for convergence. Further, one may use the inequality $\rho(\mathbf{M}^{\dagger}) \leq ||\mathbf{M}^{\dagger}||_{\infty}$. The max-norm is equal to the maximum of the absolute row sums. Hence,

$$\rho(\mathbf{M}_{\text{OAS}}) = \rho(\mathbf{M}^{\dagger}) \leq ||\mathbf{M}^{\dagger}||_{\infty} = \max\{\sigma_1, \sigma_2, \ldots, \sigma_{N-1}, \sigma_N\},$$

where σ_j is the absolute sum of entities in the j^{th} row:

$$\begin{aligned}\sigma_j &= |p^{\dagger}_{j+1}s^{\dagger}_{j}\ldots s^{\dagger}_{2}q^{\dagger}_{1}| + |p^{\dagger}_{j+1}s^{\dagger}_{j}\ldots s^{\dagger}_{3}q^{\dagger}_{2}| + \cdots + |p^{\dagger}_{j+1}q^{\dagger}_{j}| + |r^{\dagger}_{j+1}| + |p^{\dagger}_{j+1}s^{\dagger}_{j}\ldots s^{\dagger}_{1}|\\ &= |p^{\dagger}_{j+1}||s^{\dagger}_{j}|\ldots|s^{\dagger}_{2}||q^{\dagger}_{1}| + |p^{\dagger}_{j+1}||s^{\dagger}_{j}|\ldots|s^{\dagger}_{3}||q^{\dagger}_{2}| + \cdots + |p^{\dagger}_{j+1}||q^{\dagger}_{j}| + |r^{\dagger}_{j+1}| + |p^{\dagger}_{j+1}||s^{\dagger}_{j}|\ldots|s^{\dagger}_{1}|,\end{aligned}$$

which can be expressed using the nested product:

$$\sigma_j = |p^{\dagger}_{j+1}|(|s^{\dagger}_{j}|(|s^{\dagger}_{j-1}|(\ldots(|s^{\dagger}_{2}|(|s^{\dagger}_{1}| + |q^{\dagger}_{1}|) + |q^{\dagger}_{2}|) + \ldots) + |q^{\dagger}_{j-1}|) + |q^{\dagger}_{j}|) + |r^{\dagger}_{j+1}|.$$

Starting at the innermost bracket in the first term, we have $|s^{\dagger}_{1}|+|q^{\dagger}_{1}| < 1$ from Lemma 3.1.5. The next bracket is $|s^{\dagger}_{2}|(|s^{\dagger}_{1}|+|q^{\dagger}_{1}|)+|q^{\dagger}_{2}| < |s^{\dagger}_{2}|+|q^{\dagger}_{2}| < 1$. Moving to the next set of brackets, we have $|s^{\dagger}_{3}|(|s^{\dagger}_{2}|(|s^{\dagger}_{1}| + |q^{\dagger}_{1}|) + |q^{\dagger}_{2}|) + |q^{\dagger}_{3}| < |s^{\dagger}_{3}| + |q^{\dagger}_{3}| < 1$. Proceeding in this manner, we know that each term contained within brackets will be less than one in magnitude, and as such we have:

$$\begin{aligned}\sigma_j &= |p^{\dagger}_{j+1}|(|s^{\dagger}_{j}|(|s^{\dagger}_{j-1}|(\ldots(|s^{\dagger}_{2}|(|s^{\dagger}_{1}| + |q^{\dagger}_{1}|) + |q^{\dagger}_{2}|) + \ldots) + |q^{\dagger}_{j-1}|) + |q^{\dagger}_{j}|) + |r^{\dagger}_{j+1}|,\\ &< |p^{\dagger}_{j+1}|(|s^{\dagger}_{j}|(|s^{\dagger}_{j-1}|(\ldots(|s^{\dagger}_{2}| + |q^{\dagger}_{2}|) + \ldots) + |q^{\dagger}_{j-1}|) + |q^{\dagger}_{j}|) + |r^{\dagger}_{j+1}|,\\ &\vdots\\ &< |p^{\dagger}_{j+1}| + |r^{\dagger}_{j+1}|,\\ &< 1.\end{aligned}$$

Likewise, for the last two rows,

$$\begin{aligned}\sigma_{N-1} &= |r_N^\dagger||r_1^\dagger| + |p_N^\dagger||s_{N-1}^\dagger|\dots|s_2^\dagger||q_1^\dagger| + |p_N^\dagger||s_{N-1}^\dagger|\dots|s_3^\dagger||q_2^\dagger| + \dots \\ &\qquad + |p_N^\dagger||s_{N-1}^\dagger||q_{N-2}^\dagger| + |p_N^\dagger||q_{N-1}^\dagger||r_N^\dagger||p_1^\dagger| + |p_N^\dagger||s_{N-1}^\dagger|\dots|s_1^\dagger|, \\ &= |p_N^\dagger|(|s_{N-1}^\dagger|(|s_{N-2}^\dagger|(\dots(|s_2^\dagger|(|s_1^\dagger| + |q_1^\dagger|) + |q_2^\dagger|) + \dots) + |q_{N-2}^\dagger|) + |q_{N-1}^\dagger|) \\ &\qquad + |r_N^\dagger|(|p_1^\dagger| + |r_1^\dagger|), \\ &< |p_N^\dagger|(|s_{N-1}^\dagger|(|s_{N-2}^\dagger|(\dots(|s_2^\dagger| + |q_2^\dagger|) + \dots) + |q_{N-2}^\dagger|) + |q_{N-1}^\dagger|) + |r_N^\dagger|(|p_1^\dagger| + |r_1^\dagger|), \\ &\ \vdots \\ &< |p_N^\dagger| + |r_N^\dagger|, \\ &< 1,\end{aligned}$$

and

$$\begin{aligned}\sigma_N &= |q_N^\dagger||r_1^\dagger| + |s_N^\dagger||s_{N-1}^\dagger|\dots|s_2^\dagger||q_1^\dagger| + |s_N^\dagger||s_{N-1}^\dagger|\dots|s_3^\dagger||q_2^\dagger| + \dots \\ &\qquad + |s_N^\dagger||s_{N-1}^\dagger||q_{N-2}^\dagger| + |s_N^\dagger||q_{N-1}^\dagger||q_N^\dagger||p_1^\dagger| + |s_N^\dagger||s_{N-1}^\dagger|\dots|s_1^\dagger|, \\ &= |s_N^\dagger|(|s_{N-1}^\dagger|(|s_{N-2}^\dagger|(\dots(|s_2^\dagger|(|s_1^\dagger| + |q_1^\dagger|) + |q_2^\dagger|) + \dots) + |q_{N-2}^\dagger|) + |q_{N-1})^\dagger| \\ &\qquad + |q_N^\dagger|(|p_1^\dagger| + |r_1^\dagger|), \\ &< |s_N^\dagger|(|s_{N-1}^\dagger|(|s_{N-2}^\dagger|(\dots(|s_2^\dagger| + |q_2^\dagger|) + \dots) + |q_{N-2}^\dagger|) + |q_{N-1}^\dagger|) + |q_N^\dagger|(|p_1^\dagger| + |r_1^\dagger|), \\ &\ \vdots \\ &< |s_N^\dagger| + |q_N^\dagger|, \\ &< 1.\end{aligned}$$

Now that the absolute row sums are shown to be less than one, we must have

$$\rho(\mathbf{M}_{\text{OAS}}) = \rho(\mathbf{M}^\dagger) \leq ||\mathbf{M}^\dagger||_\infty < 1.$$

Thus, the algorithm converges for any $\alpha \geq 0$ and $N \geq 2$. □

With a slight modification to the code implemented for the OPS method, we obtain the implementation of the OAS algorithm. We verify the convergence of the algorithm on a helix of 10 revolutions wrapped around the torus of major radius 3 and minor radius 1. The toroidal helix is partitioned into four non-overlapping subdomains shown in Figure 3.16. The solutions at different iterations are shown in Figure 3.17, assuming $c = 1$ and $\alpha = 0.25$. The max-norm of the error vector is shown in Figure 3.18 against the number of passed iterations for two different α values. Similar to the OPS method, we show that one can restrict the analysis to $\alpha \geq 1$ as the spectral radius obtained from α and $1/\alpha$ are the same. This is shown in the following corollary.

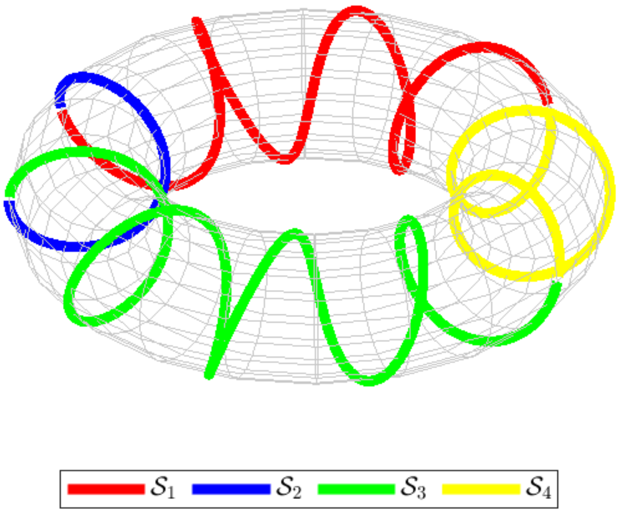

Figure 3.16: The toroidal helix with four non-overlapping subdomains.

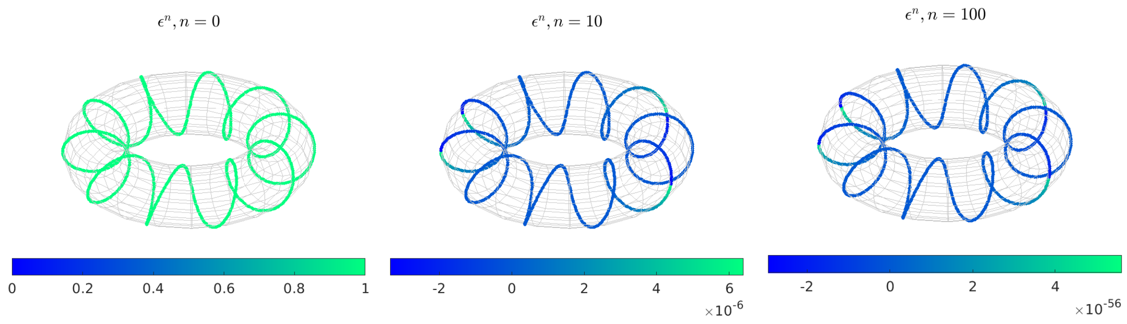

Figure 3.17: The global solution to (3.36) with $c = 1$ and $\alpha = 0.25$ along the toroidal helix shown in Figure 3.16 at different iterations.

Corollary 3.1.7. The OAS iterations (3.36) with $\alpha = \alpha^\star > 0$ converges with the same convergence factor as the OAS iterations (3.36) with $\alpha = 1/\alpha^\star$.

Proof. We have to show the corresponding iteration matrices have the same spectral radii. That is, it is sufficient to show the corresponding $\mathbf{M}^\dagger$ matrices for $\alpha = \alpha^\star$ and $\alpha = 1/\alpha^\star$ share the same spectral radii. By a direct substitution in (3.27), one obtains

$$p_j^\dagger(\alpha^\star) = -p_j^\dagger(\frac{1}{\alpha^\star}), \qquad r_j^\dagger(\alpha^\star) = r_j^\dagger(\frac{1}{\alpha^\star}).$$

Similarly,

$$q_j^\dagger(\alpha^\star) = -q_j^\dagger(\frac{1}{\alpha^\star}), \qquad s_j^\dagger(\alpha^\star) = s_j^\dagger(\frac{1}{\alpha^\star}).$$

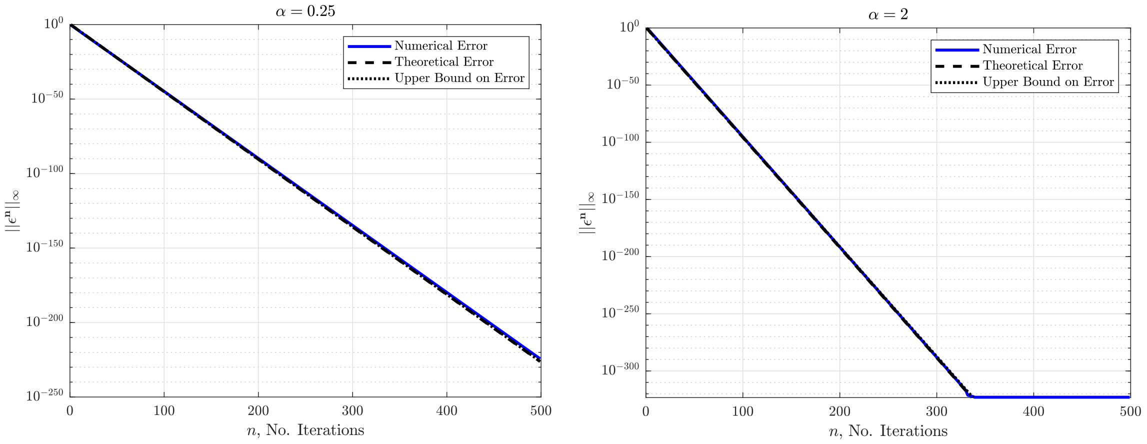

Figure 3.18: Decay rate of the max-norm of the error vector for different Robin parameters.

The entry in row $i \leq N-1$ and column $j \leq i$ of $\mathbf{M}^{\dagger}$ has the terms $p^{\dagger}_{i+1}$ and $q^{\dagger}_{j}$. Thus, $p^{\dagger}_{i+1}(\dfrac{1}{\alpha^{\star}})q^{\dagger}_{j}(\dfrac{1}{\alpha^{\star}}) = p^{\dagger}_{i+1}(\alpha^{\star})q^{\dagger}_{j}(\alpha^{\star})$. Hence, $\mathbf{M}^{\dagger}(\dfrac{1}{\alpha^{\star}})$ and $\mathbf{M}^{\dagger}(\alpha^{\star})$ have identical entries except for the entries located in the last row or column. In those cases, the entry is off by a negative sign. Note that the entry in the last row and column is the same for both matrices. Introducing the $N \times N$ permutation matrix $P = [a_{ij}]$ where

$$a_{ij} = \begin{cases} 1; & i = j \neq N, \\ \\ -1; & i = j = N, \\ \\ 0; & i \neq j, \end{cases}$$

we have $\mathbf{M}^{\dagger}(\alpha^{\star}) = P^{-1}\mathbf{M}^{\dagger}(\dfrac{1}{\alpha^{\star}})P$. Notice that $P^{-1} = P$. Finally, $\mathbf{M}^{\dagger}(\alpha^{\star})$ and $\mathbf{M}^{\dagger}(\dfrac{1}{\alpha^{\star}})$ are similar matrices and have identical spectral radii. □

From the boundary condition, we anticipate to obtain the convergence behaviour of the CAS method from the OAS method in the limit $\alpha \to \infty$. Corollary 3.1.7 also suggests that $\alpha = 0$ has the same behaviour as $\alpha \to \infty$. The following corollary provides the proof of equivalency between the OPS method and the OAS method with $\alpha \to \infty$ and $\alpha = 0$.

Corollary 3.1.8. For a given partitioning of a closed 1-manifold based on Definition 3.1.1, the OPS iterations (3.22) in the limit $\alpha \to \infty$ for the positive Helmholtz equation is equivalent to the CPS iterations (3.5).

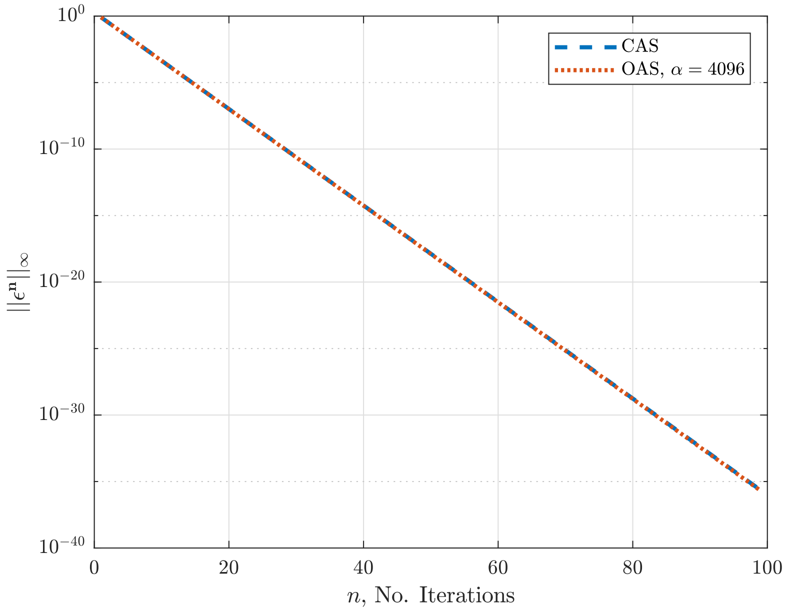

Figure 3.19: The OAS ($\alpha = 4096$) and CAS methods comparison.

Proof. By a direct substitution, one obtains

$$\lim_{\alpha\to\infty} p_j^\dagger(\alpha) = -p_j^\dagger(\alpha = 0) = \frac{1 - e^{2\sqrt{c}(\ell_j - \delta_{j-1})}}{1 - e^{2\sqrt{c}\ell_j}} e^{\sqrt{c}\delta_{j-1}},$$
$$\lim_{\alpha\to\infty} r_j^\dagger(\alpha) = r_j^\dagger(\alpha = 0) = \frac{1 - e^{2\sqrt{c}\delta_{j-1}}}{1 - e^{2\sqrt{c}\ell_j}} e^{\sqrt{c}(\ell_j - \delta_{j-1})},$$

for $j = 1, \dots, N$ where the right-hand sides are the quantities defined for the classical Schwarz algorithms in (3.9). Likewise, $q_j^\dagger$ and $s_j^\dagger$ are equal to their counterparts in the classical Schwarz methods in the limit $\alpha \to \infty$. Thus, the OAS method in the limit $\alpha \to \infty$ is consistent with the CAS method. In addition, they are equivalent in the limit $\alpha = 0$ as the OAS is identical to $\alpha \to \infty$, according to Corollary 3.1.7. □

To numerically verify the above corollary, we solve the positive Helmholtz equation with $c = 1$ on the toroidal helix shown in Figure 3.16 using the OAS and CAS methods. Note that the CAS method does not converge on a non-overlapping set of subdomains as in Figure 3.16, thus we have to use an overlapping set of subdomains. Figure 3.19 illustrates the error plots of the OAS method with a large Robin parameter and the CAS method. As expected based on the above corollary, the error vectors of the two methods decay with the same rate.

Corollary 3.1.9. The OPS iterations (3.22) with $\alpha \geq 1$ for the positive Helmholtz equation on any closed 1-manifold partitioned according to Definition 3.1.2 with $N \geq 3$ converges with the factor of

$$\kappa \leq {p^{\dagger}}^{2} + p^{\dagger} r^{\dagger} + r^{\dagger},$$

and for $N = 2$:

$$\kappa = (p^{\dagger} + r^{\dagger})^{2}$$

Proof. The convergence factor is equal to the spectral radius of $\mathbf{M}_{\mathrm{OAS}}$. Since $\mathbf{M}_{\mathrm{OAS}}$ and $\mathbf{M}^{\dagger}$ are similar, the spectral radius of $\mathbf{M}_{\mathrm{OAS}}$ is bounded by the infinity-norm of $\mathbf{M}^{\dagger}$. On the other hand, we have

$$p_1^{\dagger} = p_2^{\dagger} = \cdots = p_N^{\dagger} = q_1^{\dagger} = q_2^{\dagger} = \cdots = q_N^{\dagger},$$

$$r_1^{\dagger} = r_2^{\dagger} = \cdots = r_N^{\dagger} = s_1^{\dagger} = s_2^{\dagger} = \cdots = s_N^{\dagger},$$

for an equal-sized partitioning. By defining $p^{\dagger} = p_j^{\dagger}$ and $r^{\dagger} = r_j^{\dagger}$ for $j = 1, \ldots, N$, $\mathbf{M}^{\dagger}$ reduces to

$$\mathbf{M}_{\mathrm{OAS}} = \begin{bmatrix} {p^{\dagger}}^{2} & r^{\dagger} & & & & & p^{\dagger} r^{\dagger} \\ {p^{\dagger}}^{2} r^{\dagger} & {p^{\dagger}}^{2} & r^{\dagger} & & & & p^{\dagger} {r^{\dagger}}^{2} \\ {p^{\dagger}}^{2} {r^{\dagger}}^{2} & {p^{\dagger}}^{2} r^{\dagger} & {p^{\dagger}}^{2} & r^{\dagger} & & & p^{\dagger} {r^{\dagger}}^{3} \\ \vdots & & & \ddots & \ddots & & \vdots \\ {p^{\dagger}}^{2} {r^{\dagger}}^{N-3} & {p^{\dagger}}^{2} {r^{\dagger}}^{N-4} & \cdots & & {p^{\dagger}}^{2} & r^{\dagger} & p^{\dagger} {r^{\dagger}}^{N-2} \\ {r^{\dagger}}^{2} + {p^{\dagger}}^{2} {r^{\dagger}}^{N-2} & {p^{\dagger}}^{2} {r^{\dagger}}^{N-3} & \cdots & & {p^{\dagger}}^{2} r^{\dagger} & {p^{\dagger}}^{2} & p^{\dagger} r^{\dagger} + p^{\dagger} {r^{\dagger}}^{N-1} \\ p^{\dagger} r^{\dagger} + p^{\dagger} {r^{\dagger}}^{N-1} & p^{\dagger} {r^{\dagger}}^{N-2} & \cdots & & p^{\dagger} {r^{\dagger}}^{2} & {r^{\dagger}}^{2} & {p^{\dagger}}^{2} + {r^{\dagger}}^{N} \end{bmatrix}.$$

The iteration matrix in Corollary 3.1.3 has the same structure as above. Using the result of Corollary 3.1.3 and noting that $p^{\dagger} + r^{\dagger} < 1$, we obtain the maximum row sum as ${p^{\dagger}}^{2} + p^{\dagger} r^{\dagger} + r^{\dagger}$. Thus, the convergence factor is bounded by

$$\kappa \leq {p^{\dagger}}^{2} + p^{\dagger} r^{\dagger} + r^{\dagger},$$

Furthermore, if the number of subdomains is 2, the row sums are both equal to $(p^{\dagger} + r^{\dagger})^{2}$, and the convergence factor is equal to $\kappa = (p^{\dagger} + r^{\dagger})^{2}$. □

Although the above corollary gives the proof for $\alpha \geq 1$, one can use it for $0 \leq \alpha < 1$ according to Corollary 3.1.7. We now draw our attention to finding the value of the Robin parameter which secures the best convergence factor.

Theorem 3.1.11. For a given partitioning of a simple closed 1-manifold based on Definition 3.1.1, the OAS iterations (3.36) with $\alpha = 1$ for the positive Helmholtz equation converges faster than any other $\alpha \geq 1$.

Proof. We show that the spectral radius of $\mathbf{M}^{\dagger}$ corresponding to $\alpha = 1$ is less than the the spectral radius of the same matrix with any $\alpha > 1$. According to Lemma 3.1.7, $\alpha = 1$ minimizes the quantities in Equation (3.27) which appear in $\mathbf{M}^{\dagger}$. Hence, we write $\mathbf{M}^{\dagger}(\alpha = 1) < \mathbf{M}^{\dagger}(\alpha)$ for any $\alpha > 1$ to denote that any non-zero element in $\mathbf{M}^{\dagger}(\alpha = 1)$ is less than the corresponding element in $\mathbf{M}^{\dagger}(\alpha)$. It has been shown in Corollary 3.1.7 that $\mathbf{M}^{\dagger}$ is a non-negative irreducible matrix for any $\alpha \geq 1$. For now, let us define $A = \mathbf{M}^{\dagger}(\alpha = 1)$ and $B = \mathbf{M}^{\dagger}(\alpha)$ for any $\alpha > 1$. Since A and B are non-negative irreducible matrices such that $A < B$, we exploit the result of Lemma 3.1.8 to obtain $\rho(A) < \rho(B)$. That is, the spectral radius of $\mathbf{M}^{\dagger}$ with $\alpha = 1$ is minimal over $\alpha \geq 1$. From the similarity of $\mathbf{M}^{\dagger}$ and the iteration matrix $\mathbf{M}_{\text{OAS}}$, $\mathbf{M}_{\text{OAS}}$ with $\alpha = 1$ is the minimum for any other $\alpha \geq 1$. Corollary 3.1.7 also shows that the OPS iteration with $0 \leq \alpha \leq 1$ converges with the same rate as the OAS iteration with $1/\alpha$. Thus, $\alpha = 1$ minimizes the spectral radius of $\mathbf{M}_{\text{OAS}}$. □

Interestingly, we were able to find the optimal Robin parameter α without explicitly computing the spectral radius. The optimal Robin parameter is independent of the problem and partitioning. We verify Theorem 3.1.11 using a non-overlapping equal-sized partitioning of the toroidal helix into 4 subdomains. The OAS iterations (3.36) on the helix are solved with different values of the Robin parameter. The convergence factor for different α values is shown in Figure 3.20 along with the theoretical convergence factor obtained directly from the iteration matrix. As we observe, the numerical experiment is in a good agreement with the analysis. Note that the convergence factor associated with $\alpha = 1$ is $\kappa \approx 7 \times 10^{-8}$. At the discrete level, $\kappa \approx 7 \times 10^{-8}$ leads to convergence in only two iterations.

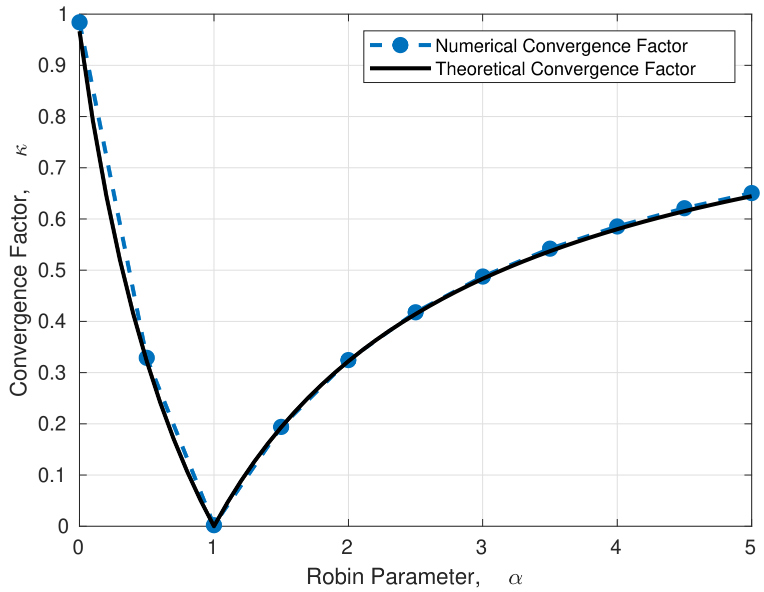

Figure 3.20: The convergence factor of the OAS iterations for the toroidal helix shown in Figure 3.16 as a function of the Robin parameter.

Chapter 4

Numerical Results

In this chapter, we provide numerical experiments for the Schwarz-CPM methods. The ultimate goal is to show that the convergence rate of the Schwarz-CPM methods is the same as the convergence of the equivalent Schwarz problem obtained by Theorem 3.1.1. Indeed, this chapter can be seen as a numerical verification of Theorem 3.1.1.

4.1 Implementation

The first step to implement the Schwarz-CPM methods is partitioning the global domain of the CPM. We have addressed the partitioning at the continuous level in Chapter 2, but partitioning at the discrete level must be specified. The domain decomposition usually occurs at the discrete level where a mesh is generated for the domain. The mesh partitioning usually is done on a single processor before the computation begins, while one may utilize parallel mesh partitioning algorithms for a fully parallel approach. The mesh partitioning problem is closely connected to the graph partitioning problem where a computational point is a node in the graph with its connectivity determined from the numerical discretization of the original problem. For a graph partitioning of a finite difference discretization, each graph node can be connected to all nodes in the stencil of the discretized operator. Moreover, in a finite element scheme, elements are treated as the nodes in the graph, followed by connecting each pair if they share an interface. After having an appropriate graph, graph partitioning tools, such as METIS [32] or its parallel version PARMETIS, can be used to efficiently perform the partitioning.

If a global meshing of the CPM is in hand, one can find the disjoint subdomains of the CPM computational domain using METIS. Given a size of overlap for each subdomain, usually as a number of overlapping layers, we obtain the overlapping subdomains by expanding each disjoint subdomain. In the CPM, we extend the manifold values along the normal direction to the manifold. Hence, it is intuitive to have the boundaries of a subdomain align with the surface normal. METIS does not necessarily yield boundaries aligned with the surface normal as it does not have a sense of the underlying geometry. Further, expanding the disjoint subdomains to get the overlapping subdomains will not fix this boundary issue. Therefore, the alignment must be done manually. Starting with finding the interface nodes between the partitions, we state that an interface point belongs to the subdomain containing the closest grid point to its closest point representation. This is an iterative procedure; Once a set of interface nodes is visited and migrated to the corresponding subdomain, we have a new set of interface nodes. We repeat the procedure up to the point that there are no more interface nodes for migration. This yields interfaces which are aligned to the surface normal. Finally, we need to complete the interpolation stencil for the boundary nodes. This changes the closest point representation which has to be modified according to Equation (2.8). Please refer to [44] for a thorough explanation of the interfaces alignment.

We introduce the sets of nodes that are essential to our implementation:

- $\tilde{\Sigma}_j^{\mathrm{A}}$, $j = 1, \cdots, N$: Disjoint sets of active nodes obtained from partitioning of the global domain, usually by a graph partitioning algorithm.

- Σ_j^{A}, $j = 1, \cdots, N$: Overlapping sets of active nodes by adding N_j^o layers of the global active nodes to $\tilde{\Sigma}_j^{\mathrm{A}}$. First we suppose $\Sigma_j^{\mathrm{A}} = \tilde{\Sigma}_j^{\mathrm{A}}$. By identifying the adjacent active nodes to Σ_j^{A} and adding the adjacent points to Σ_j^{A}, we construct the overlapping set of active nodes for the subdomain j with $N_j^o = 1$. Note that after repeating this procedure for N_j^o passes to form the overlapping set of active nodes Σ_j^{A} for the subdomain j, we are required to align the interfaces as explained.

- $\Sigma_j^{\mathrm{BC}}(\mathrm{Active})$, $j = 1, \cdots, N$: Sets of active boundary nodes obtained from completing the interpolation stencil. This corresponds to the blue semi-circles shown in Figure 2.4. Note that the closest point representation of these nodes will be modified. We use this set to enforce the transmission condition later.

- $\tilde{\Sigma}_j^{\mathrm{G}}$, $j = 1, \cdots, N$: Set of ghost nodes in the local subproblem j. $\tilde{\Sigma}_j^{\mathrm{G}}$ is a layer surrounding all active nodes of subproblem j.

- $\Sigma_j^{\mathrm{BC}}(\mathrm{Ghost})$, $j = 1, \cdots, N$: Sets of boundary ghost nodes over which we will modify the closest point representation.

The introduced sets of nodes are illustrated in Figure 4.1 for a circular arc. We now modify the closest point representation of the boundary nodes. First, we let $\Sigma_j^{\mathrm{Interface}}$ be the set of the final layer nodes in Σ_j^{A}. The closest point representation of the nodes in $\Sigma_j^{\mathrm{Interface}}$ approximates the subsurface boundaries that we called γ_{jk} and $\gamma_{jk'}$ in Figure 2.4 in Chapter 2. We collect the boundary approximations of the subdomain j into a set $\Gamma_j = \mathrm{cp}_{\mathcal{S}}(x)$ for $x \in \Sigma_j^{\mathrm{Interface}}$. These new introduced sets are shown in Figure 4.2. Thus, we introduce the following modification to the closest point representation of the subproblem

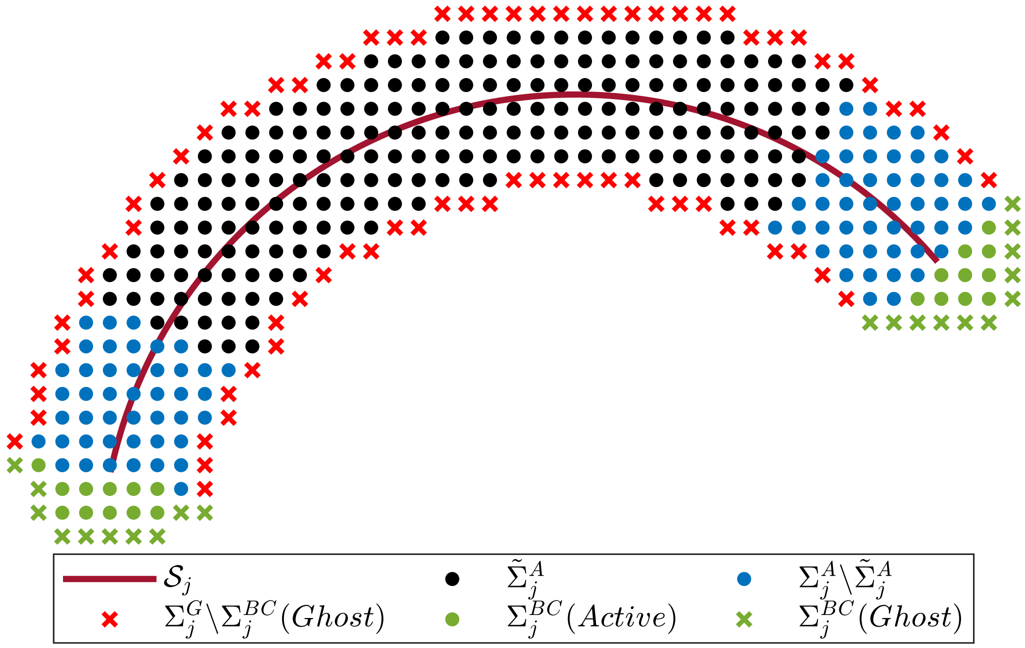
$\mathcal{S}_j$
$\tilde{\Sigma}_j^A$
$\Sigma_j^A \backslash \tilde{\Sigma}_j^A$
$\Sigma_j^G \backslash \Sigma_j^{BC}(Ghost)$
$\Sigma_j^{BC}(Active)$
$\Sigma_j^{BC}(Ghost)$

Figure 4.1: An example of the nodes required for a single subdomain in a Schwarz-CPM method with polynomial degree-four interpolation.

j:

$$\mathrm{cp}_{\mathcal{S}_j}(x) = \begin{cases} \mathrm{cp}_{\mathcal{S}}(x), & x \in \Sigma_j^{\mathrm{A}} \cup \Sigma_j^{\mathrm{G}} \backslash \Sigma_j^{\mathrm{BC}}(\mathrm{Ghost}), \\ \\ \underset{s \in \Gamma_j}{\arg\min} ||x - s||, & x \in \Sigma_j^{\mathrm{BC}}(\mathrm{Active}) \cup \Sigma_j^{\mathrm{BC}}(\mathrm{Ghost}). \end{cases} \tag{4.1}$$

The positive surface intrinsic Helmholtz equation for each subdomain can be discretized using the CPM. We discretize with an approach similar to the discretization of the single-domain CPM explained in Chapter 2. We obtain the extension matrix $\mathbf{E}_j$ and the differential operator matrix $\mathbf{\Delta_h}_j$ for each subdomain. The transmission conditions have to be enforced at the boundary nodes. We impose the transmission conditions on the extension matrix [44]. For the Dirichlet transmission condition, a first order accurate discretization can be imposed by zeroing out the row associated with the boundary node x_i in $\mathbf{E}_j$ and setting to one the entry in the column associated with the interface node $y \in \Sigma_j^{\mathrm{Interface}}$ whose closest point representation is the same as the closest point representation of x_i, i.e., $\mathrm{cp}_{\mathcal{S}_j}(y) = \mathrm{cp}_{\mathcal{S}_j}(x_i)$ [44]. Furthermore, for enforcing the Robin transmission condition with the Robin parameter α to first order accuracy, we multiply the row associated with the boundary node x_i by the scalar $1/(1 + \alpha d_i \cdot \hat{q}_i)$ where $d_i = x_i - \mathrm{cp}_{\mathcal{S}_j}(x_i)$ and $\hat{q}_i$ is the unit tangent vector to the one-manifold at $\mathrm{cp}_{\mathcal{S}_j}(x_i)$. For further details on imposing the transmission conditions at the discrete level, see [44]. After modifying the extension matrices corresponding to

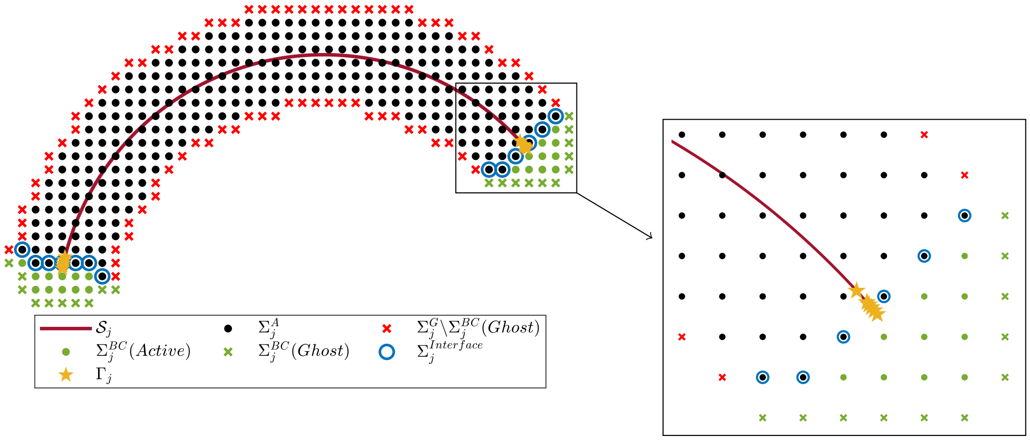

Figure 4.2: $\Sigma_j^{\text{Interface}}$ and Γ_j sets for Figure 4.1.

each subdomain, the regularized discretization of the Laplace-Beltrami operator $\mathbf{M}_j$ can be constructed using Equation (2.3). Finally, the discrete local operator for each subdomain is defined as $\mathbf{A}_j = c\mathbf{I} - \mathbf{M}_j$ where $\mathbf{I}$ is the identity matrix.

Thus, the linear systems of the form $\mathbf{A}_j\mathbf{u}_j = \mathbf{f}_j$ have to be solved for each subdomain. The right-hand side of the subproblems can be determined by $\mathbf{f}_j = f(\text{cp}_{\mathcal{S}_j}(x))$ for all $x \in \Sigma_j^{\text{A}}$. Then, we update the rows associated with the active boundary nodes Σ_j^{BC}(Active) for each iteration. This requires applying the transmission condition to the adjacent subsolutions. To avoid this, we exploit the linearity of the problem to instead solve for additive corrections to the current solution [16]. Suppose that the single-domain CPM discretization leads to the linear system $\mathbf{Au} = \mathbf{f}$. Starting with an initial guess over the active nodes of the global solution, we compute the initial global residual as $\mathbf{r}^0 = \mathbf{f} - \mathbf{Au}^0$. Next, the portion of the global residual acting over the active nodes in the subdomain j is denoted as $\mathbf{r}_j^0$. To enforce the boundary values, it is sufficient to zero out the rows corresponding to the active boundary nodes. Hence, updating $\mathbf{f}_j$ at the boundary nodes is not required anymore. After solving for the additive corrections $\mathbf{e}_j^0$ in $\mathbf{A}_j\mathbf{e}_j^0 = \mathbf{r}_j^0$, we construct the global correction by restricting the local corrections to their disjoint subdomains. The global correction is added to the initial guess to create the new global solution, i.e., $\mathbf{u}^1 = \mathbf{u}^0 + \mathbf{e}^0$. We iterate until a desired convergence criteria is met. This approach is called the Restricted Additive Schwarz (RAS) and has the same convergence factor as the Schwarz-CPM methods introduced so far [19].

4.2 Numerical Results

We now have all necessary details to perform the numerical experiments. The implementation is done in MATLAB. Throughout the experiments, we suppose $N_o = N_o^j$ for $j = 1, \ldots, N$ for simplicity. Moreover, the discretization of the CPM is done over a uniform

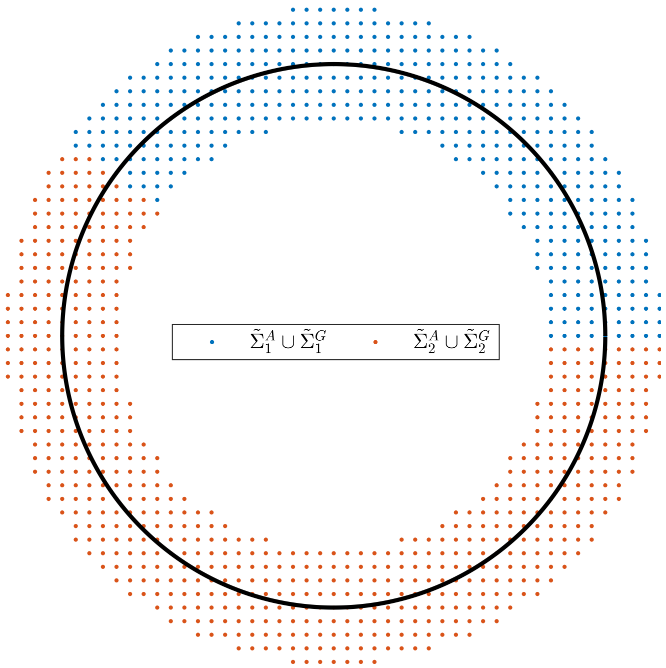

● $\tilde{\Sigma}_1^A \cup \tilde{\Sigma}_1^G$
● $\tilde{\Sigma}_2^A \cup \tilde{\Sigma}_2^G$

Figure 4.3: The domain decomposition for the CPM with $\Delta x = 0.05$ and $p = 4$ on the unit circle. Note that the interfaces are aligned.

mesh in $\mathbb{R}^d$ with size Δx. In addition, we suppose $c = 1$ and $f = 0$ since they have no effect on convergence. Note that the Schwarz-CPM methods with the assumption $f = 0$ mimics the iterations for the error.

We start the verification by solving the positive surface intrinsic Helmholtz equation on the unit circle. After constructing the required computational nodes of the CPM for a degree-p interpolation and the mesh size Δx, we decompose the nodes into two disjoint subdomains with the ratio 2:3. We investigate three configurations of $(\Delta x = 0.05, p = 2)$, $(\Delta x = 0.05, p = 4)$, and $(\Delta x = 0.01, p = 2)$ for the CPM to compare the effect of different parameters on the convergence factor. Furthermore, we assume $\alpha = 1$ for the Robin parameter involved in the optimized Schwarz methods. We add 5 layers of nodes $(N_o = 5)$ and 25 layers of nodes $(N_o = 10)$ to disjoint subdomains in order to form the overlapping sets of nodes when $\Delta x = 0.05$ and $\Delta x = 0.01$, respectively. This keeps the overlapping subdomains unaffected by changing the mesh size. The disjoint sets of nodes are shown in Figure 4.3. The error plots are illustrated in Figure 4.4. The numerical errors are the max-norm of the error values computed at the sets Σ_j^{BC} for $j = 1, \ldots, N$. In addition, the theoretical errors are computed by explicitly constructing the iteration matrix associated with the partitioning. Indeed, the closest point representation of the boundary nodes in Σ_j^{BC} for $j = 1, \ldots, N$ gives the approximate boundary locations. The approximate boundary locations are used to find the equivalent problem at the continuous level. Next, the iteration matrix associated with the equivalent continuous problem is constructed whose

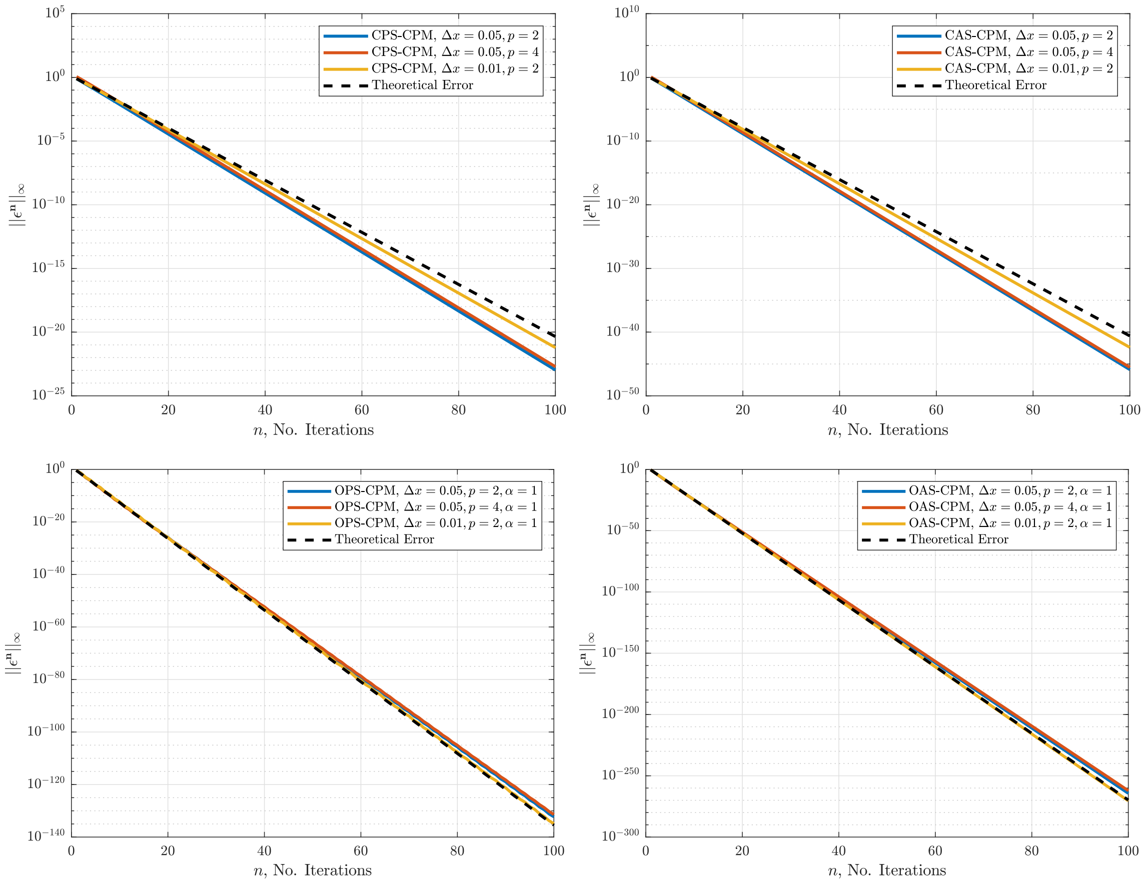

Figure 4.4: Error plots for different Schwarz-CPM methods on the unit circle shown in Figure 4.3.

spectral radius gives the theoretical decay rate of the error. As we observe, the convergence factors of the methods agree with the theoretical errors obtained from the analysis as we refine the mesh size. The degree of interpolation has roughly no effect on the convergence factor.

We now investigate the effect of N_o on convergence. Figure 4.5 depicts the convergence factor as a function of overlap. The experiments are done on an equal-sized partitioning of the unit circle with four subdomains and varying overlap. The experiments are consistent with the analysis carried out in Chapter 3, although the mesh size is not chosen too small. In Chapter 3, we explained that the convergence factor of the OPS iterations with $\alpha = 1$ for an equal-sized partitioning is given by $\kappa = e^{-\sqrt{c}L/N}$. In Figure 4.5, we observe that the convergence factor of the OPS-CPM method is close to the theoretical convergence factor $e^{-\sqrt{c}L/N} = e^{-\pi/4} \approx 0.2079$

Next, we use the edge of the Möbius strip introduced in Chapter 3 to test the convergence of the optimized Schwarz methods for the CPM with different Robin parameters. The edge of the Möbius strip is partitioned with four equal-sized subdomains and $N_o = 2$. The

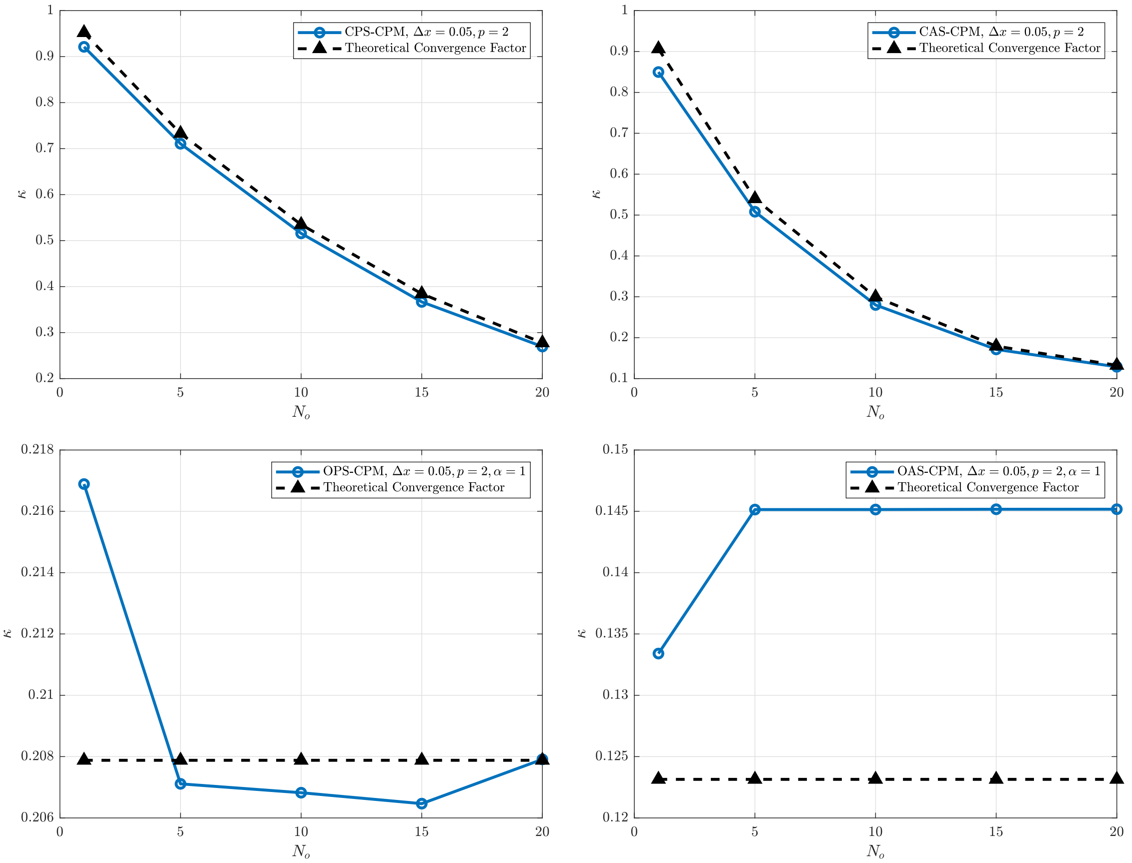

Figure 4.5: The convergence factor of the Schwarz-CPM methods against the overlap size on an equal-sized partitioning of the unit circle with four subdomains.

cloud points are shown in Figure 4.6. In Figure 4.7, we have plotted the convergence of the optimized Schwarz-CPM methods versus the Robin parameter. As shown in Chapter 3, $\alpha = 1$ secures the best convergence factor. Furthermore, $\alpha = 1$ is the optimal Robin parameter for the experiments on manifolds of co-dimension one in [44].

Finally, we compare the Schwarz-CPM methods by solving the positive surface intrinsic Helmholtz equation on a helix of 5 revolutions wrapped around the torus of major radius 3 and minor radius 1. The toroidal helix is decomposed into three subdomains with ratios 2:3:5. We have also set $N_o = 10$. Figure 4.8 illustrates each set of disjoint cloud points with a different colour. We use $\Delta x = 0.05$ and a degree-2 polynomial interpolation for the CPM. Notice that the tubular band around the helix is thinner than the tubular region around the Möbius edge in Figure 4.6 as the latter uses a degree-4 interpolation. The four Schwarz-CPM methods introduced in this thesis are applied to the positive surface intrinsic Helmholtz equation. We set the Robin parameter $\alpha = 1$ to achieve the best convergence factor. The methods are compared in Figure 4.9. The CPS-CPM has the slowest rate of convergence since it applies the basic transmission condition (Dirichlet) on the solution

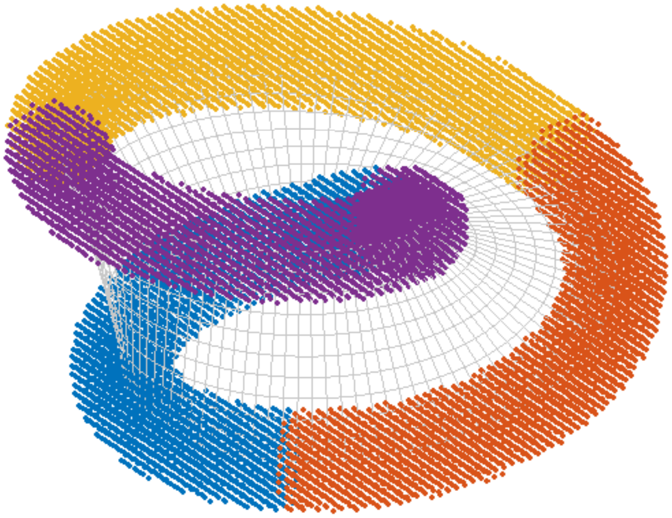

Figure 4.6: The cloud points for the edge of the Möbius strip with $\Delta x = 0.05$ and $p = 4$.

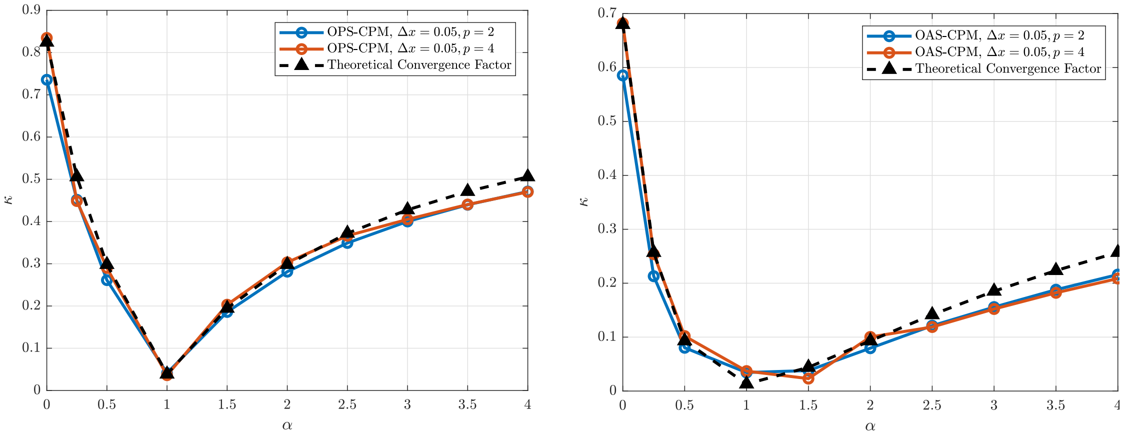

Figure 4.7: The convergence factor of the optimized Schwarz-CPM methods against the Robin parameter on the partitioning of the Möbius edge shown in Figure 4.6.

obtained from the previous iteration. The CAS-CPM method utilizes the latest available information at the boundaries, a property that boosts its convergence. The OPS-CPM method is a parallel iteration with the optimized transmission condition (Robin). With an appropriate choice of the Robin parameter, this method can outperform the CAS-CPM method. Finally, the OAS-CPM iterations are the fastest methods because they benefit from the Robin transmission condition and the latest available solution. As expected, the optimized methods are more suitable for the CPM.

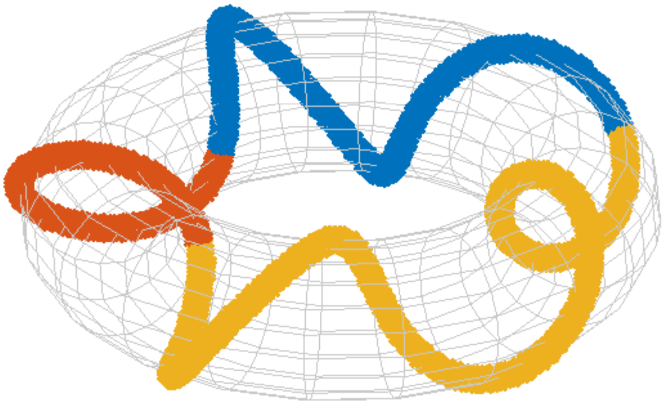

Figure 4.8: The coloured disjoint cloud points for the toroidal helix with $\Delta x = 0.05$ and $p = 2$.

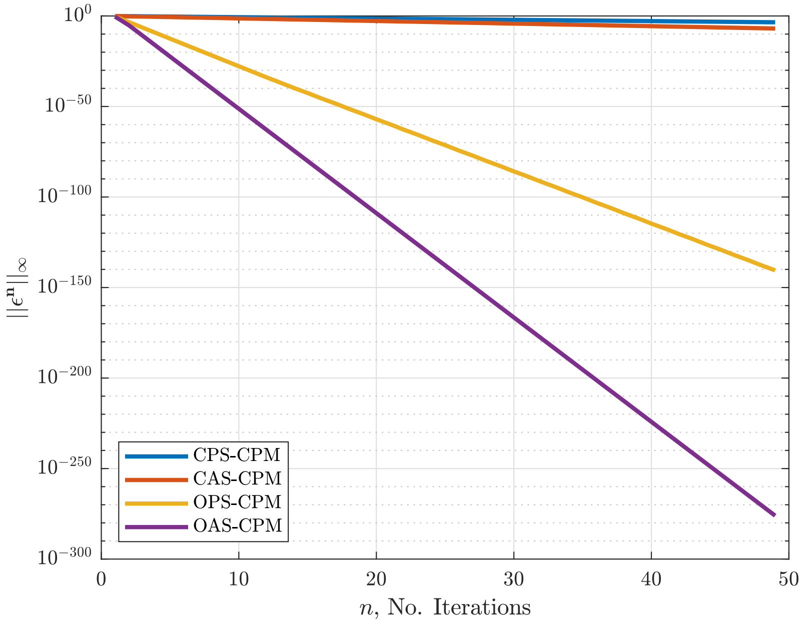

Figure 4.9: The decay rates of different Schwarz-CPM methods on the partitioning of the toroidal helix shown in Figure 4.8.

Chapter 5

Conclusion

Employing Schwarz methods as solvers for the CPM parallelizes the solution of PDEs on surfaces and enhances the performance for large scale problems. In this thesis, convergence of the (continuous) CPM equipped with four different Schwarz solvers was investigated for an arbitrary one-dimensional simple and closed manifold in $\mathbb{R}^d$. We first reduced the problem to an equivalent Schwarz method for the positive surface intrinsic Helmholtz equation on a periodic one-dimensional domain. We investigated the equivalent Schwarz methods in detail and proved that they are convergent. We have found the convergence factor or an upper bound on the convergence factor of the Schwarz methods in the case where the subdomains are of equal size and overlap. The optimal Robin parameter $\alpha = 1$ was also found for the introduced optimized Schwarz methods. All the results on the equivalent Schwarz methods were verified numerically. Next, we solved the positive surface intrinsic Helmholtz equation on a one-dimensional manifold using the Schwarz-CPM to verify the equivalency between the Schwarz-CPM and its equivalent Schwarz method. Observed convergence rates agree with our theory as the mesh spacing is refined. Indeed, the results apply to any convergent discretization (e.g., a finite element discretization) of Schwarz solvers applied to surface PDEs as the mesh spacing approaches zero.

In order to extend this work, the convergence of the Schwarz-CPM methods at the discrete level on one-dimensional manifolds could be investigated. In addition, showing convergence of the Schwarz-CPM methods on manifolds of co-dimension one is an interesting potential future step. It could be followed by seeking the optimal Robin parameter for optimized Schwarz methods. In addition, Schwarz methods employed as a preconditioner for the CPM could be analyzed at the discrete level. How the constant c in the surface intrinsic positive Helmholtz equation affects the convergence of domain decomposition methods could be studied later. Finally, note that other domain decomposition methods could be utilized and investigated as a solver or a preconditioner for the CPM.

Bibliography

[1] David Adalsteinsson and James A Sethian. Transport and diffusion of material quantities on propagating interfaces via level set methods. *Journal of Computational Physics*, 185(1):271–288, 2003.

[2] Micol Amar and Roberto Gianni. Laplace–Beltrami operator for the heat conduction in polymer coating of electronic devices. *Discrete & Continuous Dynamical Systems-B*, 23(4):1739, 2018.

[3] Sigurd Angenent, Steven Haker, Allen Tannenbaum, and Ron Kikinis. On the Laplace-Beltrami operator and brain surface flattening. *IEEE Transactions on Medical Imaging*, 18(8):700–711, 1999.

[4] Raquel Barreira, Charles M Elliott, and Anotida Madzvamuse. The surface finite element method for pattern formation on evolving biological surfaces. *Journal of Mathematical Biology*, 63(6):1095–1119, 2011.

[5] Mikhail Belkin and Partha Niyogi. Laplacian eigenmaps for dimensionality reduction and data representation. *Neural computation*, 15(6):1373–1396, 2003.

[6] Abraham Berman and Robert J Plemmons. *Nonnegative matrices in the mathematical sciences*. SIAM, 1994.

[7] Jean-Paul Berrut and Lloyd N. Trefethen. Barycentric Lagrange interpolation. *SIAM Review*, 46(3):501–517, 2004.

[8] Marcelo Bertalmıo, Li-Tien Cheng, Stanley Osher, and Guillermo Sapiro. Variational problems and partial differential equations on implicit surfaces. *Journal of Computational Physics*, 174(2):759–780, 2001.

[9] Jay Chu and Richard Tsai. Volumetric variational principles for a class of partial differential equations defined on surfaces and curves. *Research in the Mathematical Sciences*, 5:1–38, 2017.

[10] Ming Chuang, Linjie Luo, Benedict J. Brown, Szymon Rusinkiewicz, and Michael Kazhdan. Estimating the Laplace–Beltrami operator by restricting 3d functions. In *Proceedings of the Symposium on Geometry Processing*, SGP '09, page 1475–1484, Goslar, DEU, 2009. Eurographics Association.

[11] Moo K Chung and Jonathan Taylor. Diffusion smoothing on brain surface via finite element method. In *2004 2nd IEEE International Symposium on Biomedical Imaging: Nano to Macro (IEEE Cat No. 04EX821)*, pages 432–435. IEEE, 2004.

[12] Jean Côté, Martin J Gander, Lahcen Laayouni, and Sébastien Loisel. Comparison of the Dirichlet-Neumann and optimal Schwarz method on the sphere. In *Domain decomposition methods in science and engineering*, pages 235–242. Springer, 2005.

[13] Nicolas Courty, Thomas Burger, and Johann Laurent. Perturbo: a new classification algorithm based on the spectrum perturbations of the Laplace–Beltrami operator. In *Joint European Conference on Machine Learning and Knowledge Discovery in Databases*, pages 359–374. Springer, 2011.

[14] Patrick Degener, Jan Meseth, and Reinhard Klein. An adaptable surface parameterization method. *IMR*, 3:201–213, 2003.

[15] Alan Demlow and Gerhard Dziuk. An adaptive finite element method for the Laplace–Beltrami operator on implicitly defined surfaces. *SIAM Journal on Numerical Analysis*, 45(1):421–442, 2007.

[16] Victorita Dolean, Pierre Jolivet, and Frédéric Nataf. An Introduction to Domain Decomposition Methods: algorithms, theory and parallel implementation. Lecture, January 2015.

[17] Anastasia Dubrovina and Ron Kimmel. Matching shapes by eigendecomposition of the Laplace–Beltrami operator. In *Proc. 3DPVT*, volume 2, page 2. Citeseer, 2010.

[18] Gerhard Dziuk and Charles M Elliott. Finite element methods for surface PDEs. *Acta Numerica*, 22:289–396, 2013.

[19] E. Efstathiou and M. J. Gander. Why restricted additive Schwarz converges faster than additive Schwarz. *BIT Numer. Math.*, 43, 2003.

[20] Charles M Elliott and Thomas Ranner. Evolving surface finite element method for the Cahn–Hilliard equation. *Numerische Mathematik*, 129(3):483–534, 2015.

[21] Michael S Floater and Kai Hormann. Surface parameterization: a tutorial and survey. *Advances in multiresolution for geometric modelling*, pages 157–186, 2005.

[22] Martin J Gander and Tommaso Vanzan. Optimized Schwarz methods for advection diffusion equations in bounded domains. In *European Conference on Numerical Mathematics and Advanced Applications*, pages 921–929. Springer, 2017.

[23] Martin J Gander and Hui Zhang. Optimized Schwarz methods with overlap for the Helmholtz equation. *SIAM Journal on Scientific Computing*, 38(5):A3195–A3219, 2016.

[24] Martin Jakob Gander. Overlapping Schwarz for linear and nonlinear parabolic problems. In *9th International Conference on Domain Decomposition Methods*, pages 97–104, 1996.

[25] Martin Jakob Gander. Schwarz methods over the course of time. *Electronic Transactions on Numerical Analysis*, 31:228–255, 2008.

[26] David Gilbarg and Neil S Trudinger. *Elliptic partial differential equations of second order*, volume 224. springer, 2015.

[27] Ingrid Von Glehn, Thomas März, and Colin B. Macdonald. An embedded method-of-lines approach to solving partial differential equations on surfaces, 2013.

[28] Gene H Golub and Charles F Van Loan. Matrix computations. johns hopkins studies in the mathematical sciences, 1996.

[29] John B Greer. An improvement of a recent Eulerian method for solving pdes on general geometries. *Journal of Scientific Computing*, 29(3):321–352, 2006.

[30] D. Halpern, O.E. Jensen, and J.B. Grotberg. A theoretical study of surfactant and liquid delivery into the lung. *J Appl Physiol (1985)*, 85:333–52, 07 1998.

[31] Yasushi Ito and Kazuhiro Nakahashi. Surface triangulation for polygonal models based on cad data. *International Journal for Numerical Methods in Fluids*, 39(1):75–96, 2002.

[32] George Karypis and Vipin Kumar. A fast and high quality multilevel scheme for partitioning irregular graphs. *SIAM Journal on Scientific Computing*, 20(1):359–392, 1998.

[33] Kiran K Katta, Ramachandran D Nair, and Vinod Kumar. High-order finite-volume transport on the cubed sphere: Comparison between 1d and 2d reconstruction schemes. *Monthly Weather Review*, 143(7):2937–2954, 2015.

[34] Shigeru Kondo and Rihito Asai. A reaction–diffusion wave on the skin of the marine angelfish pomacanthus. *Nature*, 376:765–768, 08 1995.

[35] Venkat Krishnamurthy and Marc Levoy. Fitting smooth surfaces to dense polygon meshes. In *Proceedings of the 23rd annual conference on Computer graphics and interactive techniques*, pages 313–324, 1996.

[36] Julien Lefèvre and Jean-François Mangin. A reaction-diffusion model of human brain development. *PLOS Computational Biology*, 6(4):1–10, 04 2010.

[37] Bruno Lévy. Laplace–Beltrami eigenfunctions towards an algorithm that "understands" geometry. In *IEEE International Conference on Shape Modeling and Applications 2006 (SMI'06)*, pages 13–13. IEEE, 2006.

[38] Bruno Lévy, Sylvain Petitjean, Nicolas Ray, and Jérome Maillot. Least squares conformal maps for automatic texture atlas generation. *ACM transactions on graphics (TOG)*, 21(3):362–371, 2002.

[39] Sébastien Loisel, Jean Côté, Martin J Gander, Lahcen Laayouni, and Abdessamad Qaddouri. Optimized domain decomposition methods for the spherical Laplacian. *SIAM Journal on Numerical Analysis*, 48(2):524–551, 2010.

[40] Sébastien Loisel and Daniel B Szyld. On the geometric convergence of optimized Schwarz methods with applications to elliptic problems. *Numerische Mathematik*, 114(4):697–728, 2010.

[41] Colin B. Macdonald, Jeremy Brandman, and Steven J. Ruuth. Solving eigenvalue problems on curved surfaces using the closest point method. *J. Comput. Phys.*, 230:7944–7956, 2011.

[42] Colin B. Macdonald, Barry Merriman, and Steven J. Ruuth. Simple computation of reaction–diffusion processes on point clouds. *PNAS USA*, 110(23):9209–9214, 2013.

[43] Colin B. Macdonald and Steven J. Ruuth. The implicit closest point method for the numerical solution of partial differential equations on surfaces. *SIAM J. Sci. Comput.*, 31(6):4330–4350, 2010.

[44] Ian C. T. May, Ronald D. Haynes, and Steven J. Ruuth. Schwarz solvers and preconditioners for the closest point method. *SIAM Journal on Scientific Computing*, 42(6):A3584–A3609, 2020.

[45] Barry Merriman and Steven J. Ruuth. Diffusion generated motion of curves on surfaces. *Journal of Computational Physics*, 225(2):2267–2282, 2007.

[46] Tim G Myers. Extension to the Messinger model for aircraft icing. *AIAA journal*, 39(2):211–218, 2001.

[47] Maxim A Olshanskii, Arnold Reusken, and Jörg Grande. A finite element method for elliptic equations on surfaces. *SIAM Journal on Numerical Analysis*, 47(5):3339–3358, 2009.

[48] Abdessamad Qaddouri, Lahcen Laayouni, Sébastien Loisel, Jean Côté, and Martin J Gander. Optimized Schwarz methods with an overset grid for the shallow-water equations: preliminary results. *Applied Numerical Mathematics*, 58(4):459–471, 2008.

[49] Martin Reuter, Silvia Biasotti, Daniela Giorgi, Giuseppe Patanè, and Michela Spagnuolo. Discrete Laplace–Beltrami operators for shape analysis and segmentation. *Computers & Graphics*, 33(3):381–390, 2009. IEEE International Conference on Shape Modelling and Applications 2009.

[50] Martin Reuter, Franz-Erich Wolter, and Niklas Peinecke. Laplace–Beltrami spectra as 'Shape-DNA' of surfaces and solids. *Computer-Aided Design*, 38(4):342–366, 2006.

[51] Martin Reuter, Franz-Erich Wolter, Martha Shenton, and Marc Niethammer. Laplace–Beltrami eigenvalues and topological features of eigenfunctions for statistical shape analysis. *CAD*, 41(10):739–755, 2009. Selected Papers from the 2007 New Advances in Shape Analysis and Geometric Modeling Workshop.

[52] Steven J. Ruuth and Barry Merriman. A simple embedding method for solving partial differential equations on surfaces. *Journal of Computational Physics*, 227(3):1943–1961, January 2008.

[53] P. Sander, S. Gortler, John M. Snyder, and Hugues Hoppe. Signal-specialized parameterization. 2002.

[54] Alla Sheffer and Eric de Sturler. Parameterization of faceted surfaces for meshing using angle-based flattening. *Engineering with computers*, 17(3):326–337, 2001.

[55] John Strain. Fast tree-based redistancing for level set computations. *Journal of Computational Physics*, 152:664–686, 1999.

[56] Gang Wang, Xiaofeng Zhang, Qingtang Su, Jie Shi, Richard J Caselli, Yalin Wang, Alzheimer's Disease NeuroImaging Initiative, et al. A novel cortical thickness estimation method based on volumetric Laplace–Beltrami operator and heat kernel. *Medical image analysis*, 22(1):1–20, 2015.

[57] Chao Yang, Jianwen Cao, and Xiao-Chuan Cai. A fully implicit domain decomposition algorithm for shallow water equations on the cubed-sphere. *SIAM Journal on Scientific Computing*, 32(1):418–438, 2010.

[58] Gary Yngve and Greg Turk. Creating smooth implicit surfaces from polygonal meshes. Technical report, Georgia Institute of Technology, 1999.